

The Use of Maps in the Analysis of Networks of Coupled Neuronal Oscillators

by

Pranay Goel

B.Tech. in Engineering Physics,
Indian Institute of Technology, Bombay, India, 1998

M.S. in Physics, University of Pittsburgh

Submitted to the Graduate Faculty of

Arts and Sciences in partial fulfillment

of the requirements for the degree of

Doctor of Philosophy

University of Pittsburgh

2003

UNIVERSITY OF PITTSBURGH
FACULTY OF ARTS AND SCIENCES

This dissertation was presented

by

Pranay Goel

It was defended on

June 24, 2003

and approved by

Carson C. Chow, Associate Professor, Department of Mathematics

David Jasnow, Professor, Department of Physics

Xiao-Lun Wu, Associate Professor, Department of Physics

Committee Chairpersons: G. Bard Ermentrout, Professor, Department of Mathematics, and,

Robert Coalson, Professor, Department of Physics

THE USE OF MAPS IN THE ANALYSIS OF NETWORKS OF COUPLED NEURONAL OSCILLATORS

Pranay Goel, Ph.D.

University of Pittsburgh, 2003

In this thesis we study aspects of periodic activity in model mutually-coupled oscillators inspired by the nervous system. We define and use *maps* describing the timing of activity on successive cycles. The central theme here is to examine emergent behavior in networks through the properties of the individual oscillators.

In the first chapter, we describe *Phase Response Curves* (PRCs), which map the changes in the period of an oscillator to perturbations at different phases along the cycle. We consider various networks of oscillators, pulse-coupled through their PRCs: rings, chains, arrays, and global coupling. We study conditions under which stable patterns, such as synchrony and waves, may be found.

In the second and third chapters, we model beta (12-30 Hz) and gamma (30-80 Hz) rhythms in the nervous system in reduced networks of excitatory and inhibitory neurons. We look at the intriguing results of experiments that show increases in beta band activity in human MEGs upon taking the sedative Diapam. We show that the model network is able to mimic the experimental data. The model then clarifies the inhibitory action of the drug in tissue.

We look at another experiment that finds disruption of long-range synchrony of gamma oscillations in transgenic mice with altered excitatory kinetics. We study this behavior in a reduced network that encodes for conduction delays across spatially distal sites. The model provides an explanation of this phenomenon in terms of the properties of the cells involved in generating the rhythm.

In our analyses, we use maps to study stability of the patterns of activity.

To my parents, my first teachers

Acknowledgments

Foremost, I'd like to thank my committee members, for their invaluable support and interest in my work. Professors David Jasnow and Xiao-Lun Wu have been very encouraging. Professor Robert Coalson was a wonderful mentor and friend. Professor Carson Chow has taught me much mathematics since the earliest days. His wonderful insights have spurred me on more than once.

I have benefitted greatly from their critical evaluation of my work.

To my colleagues through the years, Remus Osan, Rodica Curtu, Rukmini Kumar, Jon Drover, Yixin Guo and Stephanie Hoogendoorn who have made the journey pleasant. They have helped in little ways too numerous to recount.

Professor Nancy Kopell, Boston University, has, directly and indirectly, influenced nearly half of this work. Her relentless drive towards pushing the boundaries of the possible, have helped us uncover phenomena when I could not have expected them. She is an inspiration.

But most of all, I owe the art of this craft to my advisor, Professor Bard Ermentrout. I have much to be grateful for. For his remarkable patience and generosity. And as much for his particular brand of astringent genuineness (not unlike the Darjeeling that he is so fond of)! I have learnt more from him than these pages can indicate.

*When Koho saw his old master again, the latter lost no time in asking him, "Who is it that carries this lifeless corpse of yours?" Koho burst out a "Kwats!" Thereupon the master took up a stick ready to give him a blow, but the disciple held it back, saying, "You cannot give me a blow today." "Why can't I?" was the master's demand. Instead of replying to him, however, Koho left the room briskly. The following day the master asked him, "All things return to the One, and where does the One return to?" "The dog is lapping the boiling water in the cauldron." "Where did you get this nonsense?" reprimanded the master. "You had better ask yourself," promptly came the response. The master rested, well satisfied. (D. T. Suzuki, *Zen Buddhism*)*

Table of Contents

List of Figures	ix
1. Introduction	1
2. Synchrony, Stability, and Firing Patterns in Pulse-Coupled Oscillators	4
2.1 Introduction	4
2.2 Phase response curves and coupled phase models	5
2.2.1 Defining the PRC	5
2.2.2 Some exactly computable PRCs	6
2.2.3 The Geometry of PRCs	11
2.2.4 Coupling with PRCs	14
2.2.5 “Weak” coupling	16
2.2.6 Smooth pulsatile coupling	16
2.3 Two oscillators	19
2.3.1 Locking	21
2.3.2 Stability of the fixed points of the map	22
2.3.3 All-to-all coupling	23
2.4 One-dimensional geometries	28
2.4.1 Waves in a ring	30
2.4.2 Chains of PRCs	34
2.5 Two-dimensional arrays of coupled oscillatory neurons	35
2.5.1 A simulation of the wave	36
2.5.2 The exact system of equations	37
2.5.3 The 4×4 array	37
2.5.3.1 Results of the simulation	37

2.5.4	The 6×6 array	38
2.5.5	Larger two-dimensional arrays	40
2.6	Discussion	41
3.	On the Increase in the Human Beta Rhythm Activity with the Sedative	
	Diapam	45
3.1	Introduction	45
3.2	Modeling	46
3.3	The “Rest State Network”: Weak g_{ei}	47
3.3.1	Analysis of the Role of Inhibition in Determining the Relative Phases of Firing of the E-cells	48
3.4	Active Processing: the Effects of a Significant g_{ei}	58
3.5	Discussion	59
3.6	Appendix	62
4.	Analysis of the Disruption of Synchrony in Networks with Altered Excitatory	
	Kinetics	66
4.1	Introduction	66
4.1.1	The Findings of Fuchs <i>et al</i> [1]	67
4.1.2	The Simplified Biophysical Model	70
4.1.3	ING and PING rhythms	71
4.2	Regions of Stable Synchrony in the $\tau_e - \delta$ plane	72
4.3	Reduction to a Map in the Ermentrout-Kopell Model	72
4.3.1	Analysis of Synchrony	77
4.4	Dynamics of Synchrony in the $\tau_e - \delta$ plane	78
4.4.1	$\tau_e = 3$	79
4.4.1.1	The T_I map	80
4.4.1.2	$\delta=0.5$	83
4.4.1.3	$\delta=1$	83
4.4.1.4	$\delta=4$	84
4.4.1.5	δ around 8	85
4.4.1.6	$\delta=16$	85

4.4.2	$\tau_e=4$	86
4.4.3	$\tau_e=1.5$	86
4.4.4	The Experimental Results of Fuchs <i>et al</i>	90
4.5	Discussion	91
4.6	Appendix	92
5.	Discussion	94
	Appendix	98
	Bibliography	100

List of Figures

Figure 2.1	The PRCs for the integrate-and-fire model (top); the quadratic integrate-and-fire model (middle) and the radial-isochron clock (bottom)	7
Figure 2.2	The effect of a perturbation on the radial isochron clock	9
Figure 2.3	Experimentally measured PRC (Reyes <i>et al</i>) and two approximations	10
Figure 2.4	The geometry of equation Equation (2.12)	13
Figure 2.5	Construction of the map, $x \mapsto G(x)$ for a pair of coupled PRCs	20
Figure 2.6	(A) The evolution of the phases for 3 all-to-all coupled PRCs (left) and the projection into the $\theta_2 - \theta_3$ phase-plane. (B) Same as A for 4 all-to-all PRCs . . .	27
Figure 2.7	The period as a function of the number of oscillators in the ring for (A) the cortical neuron PRC and (B) the sine model at different amplitudes of coupling .	32
Figure 2.8	Synchronization in a chain of 20 oscillators starting at random phases and using the PRC from Figure 2.3 (the phases of only a few of the oscillators are shown, for clarity). $S = 1$ is the perfectly synchronized state	35
Figure 2.9	The relative phases for the 6×6 array in the sine model. Lines denote the angle relative to the upper left corner. Outer, middle, and inner “rings” are different grey scales	39
Figure 2.10	The period as a function of the strength of coupling in a square array for the sine model	40
Figure 3.1	Power spectra computed for various values of the inhibition in the rest-state network. In the top panel, g_{ie} is held fixed at 0.9 and g_{ii} is varied. The bottom panel shows the result of holding g_{ii} at one of the values (taken from above) and increasing g_{ie}	49

Figure 3.2	Rasters and histograms of activity in the rest-state network, for fixed g_{ie} , and varying g_{ii} . Time (in milliseconds) is on the x-axis, and the cells are plotted by index on the y-axis. The fastest e-cells lie closest to the top. Parameter values for the run appear on the top-right of each panel. The bottom right panel shows a histogram of the spike times over a run of 100 periods normalized with respect to the period of the i-cells for the three rasters. Notice that the parameter values between this figure and the next, Figure 3.3, are the same as used in Figure 3.1, for comparison	50
Figure 3.3	Rasters and histograms for rest-state activity, at fixed g_{ii} , and varying g_{ie} . Note that, for reference, the red curve (and the corresponding raster panel) is the same as in Figure 3.2 above	51
Figure 3.4	Voltage traces of an i- and e-cell taken from the full simulation (top panel). The corresponding synaptic variable for i-cell, s , and AHP gating variable, z , for that e-cell are shown below (bottom panel). The inhibitory synapse peaks when the i-cell fires, and the AHP current turns on when the e-cell fires. Note that the decay time of the AHP current is larger than the time constant for decay of synaptic current. Notice also that z adapts on successive cycles.	53
Figure 3.5	The variables in the analytic model. One i-period for two values of the “drive” I to an e-cell, I_l , (top panel) and I_h (bottom panel) is shown. The e-cell fires when the total inhibition ($g_{ie} s_i + g_{ahp} z$) wears off to the value I , i.e. blue curve touches zero. The i-cells are firing with a period of 50 ms in this example. If the I is too small the cell may be never fire in any one period, as the top panel suggests. If, on the other hand, I is large enough, the cell may recover sufficiently to fire more than one spike within that cycle (bottom)	55
Figure 3.6	Phases of e-spikes relative to the i-period at different g_{ie} and g_{ii} numerically computed from Equations 3.2 through 3.5. Cells towards the top have the higher drives. The red dots indicate the lower value of g_{ie} than the black dots. The curves $P=50, 48, \dots, 40$ for $g_{ie}=3$ indicate the effect of a lowering the period, corresponding to smaller g_{ii} s. A similar set of curves are also plotted for $g_{ie}=4.5$ (with the black dot with the least phase being computed at $P=50$)	56

Figure 3.7	Total number of cells spiking at different g_{ii} and g_{ie} (top panel) as computed from the analytical model. (The scale is normalized by the maximal number of cells that fire at P=50 ms.) The bottom panel shows coherence (as defined in the text) of the spiking e-cells in a cycle, for various values of the inhibition . . .	57
Figure 3.8	Non-monotonicity of the peak in the power spectrum of the total synaptic conductance with increasing g_{ie} . Parameters are as for the active state network . . .	58
Figure 3.9	Spectra computed for the active state network, that is, when the role of g_{ei} is significant. (Contrast with Figure 3.1)	60
Figure 3.10	Rasters and histograms for fixed g_{ie} , and varying g_{ii} corresponding to the power spectra in Figure 3.9	61
Figure 3.11	Rasters and histograms for fixed g_{ii} , and varying g_{ie} corresponding to the power spectra in Figure 3.9	62
Figure 4.1	Figure 4 in [1]. Population gamma oscillations have disrupted synchrony in the mutant mice. (a) Example traces. Paired stratum pyramidale field potential recordings illustrated from the beginning of the posttetanic oscillatory response induced by paired tetanic stimulation. Recording site separation approximately 1 mm along the CA1 axis. Recordings are overlaid to illustrate temporal relationship between population spikes at the two sites. Oscillations from the mutant mice show a more erratic temporal relationship between spike generation at each site. (Scale bars: 3 mV, 100 ms.) Model data show superimposed average voltage signals, from two ends of the model array, for the two simulations (wild type and mutant). Each average was of 224 somatic pyramidal cell potentials, and the signals are inverted so as to resemble the experimental field potentials. Note the tight synchrony in the wild type, contrasted with the jittering back and forth in the mutant. (Scale bars: 50 mV, 100 ms.) (b) Pooled data showing pattern of phase relationship change in the mutant mice. Cross-correlations are taken from data as in a. Control data show mean cross-correlation plot for data from each of six wild-type mice (gray curves) and the global mean from these plots (black line). Inset shows distribution of modular phase relationships for 62 paired posttetanic gamma oscillations from 11 slices from six wild-type animals. Cross-correlation data from slices from mutant mice are represented in the same manner (n = 5 mice). Note erratic nature of central peak amplitudes. Inset shows distribution of modular phase relationships from 74 posttetanic oscillations from 15 slices from five mice. Model data show cross-correlations of 200 ms of data from the average signals shown in a	68

Figure 4.2	Figure 1 in [1]. Two-site synchronization occurs only over a narrow range of values for the decay time constant of interneuron AMPA-receptor-mediated EPSCs (simulations). Data are taken from 14 simulations, each with identical parameters, except for τ_{AMPA} (designated τ on the abscissa). The behavior of the system can be divided into three regimes: I, with $\tau \leq 0.9$ ms, having poor two-site synchrony; II, with $0.925\text{ms} \leq t \leq 1.025\text{ms}$, having good synchrony; III, with $t \geq 1.05$ ms, again with poor synchrony. In each regime, we plot superimposed cross-correlations of local average pyramidal cell voltages (e), from opposite ends of the array, using each simulation in that regime; and also superimposed autocorrelations of local average interneuron voltages (i), again using each simulation in the regime. In regimes I and III, the pyramidal cross-correlations lack a clear peak at 0 ms, and interneuron autocorrelation has either small, single side peaks (I), or double side peaks (III) (arrows). In regime II, in contrast, there is a sharp peak near 0 ms in the pyramidal cross-correlation, and single, sharp side peaks in the interneuron autocorrelation, the latter corresponding to synchronized interneuron doublet firing	69
Figure 4.3	The reduced network: a pair of local circuits, each with an e-, and i-cell. Conduction delays are significant only across columns	70
Figure 4.4	The phase plot of synchronous behavior in the τ_e -delay plane as computed in the two-site, four-cell network. Synchrony is marked in blue. Voltage traces show that in regions A, B and C (both) interneurons fire triplets, in regions D, E, doublets, and singlets in F. Also indicated are the regions that correspond to parameters for the interneuron firing patterns seen in wild mice (synchrony through interneuron doublets), and mutants (loss of synchrony) [1]	73

Figure 4.5	An i-cell (red) fires in response to excitation from the intrinsic (black) and extrinsic (blue) e-cells. Note that although the two e-cells are firing very close to each other, the EPSP from the distal site is experienced by the i-cell only after the delay δ (dashed blue). The map $T_I(\psi)$ thus encodes the response of the i-cell to two e-inputs, temporally dispersed by an amount ψ . T_I is then defined as the (next) firing time of the i-cell since the <i>last</i> received e-pulse. Note that since the inhibitory synapses are close to saturation (section 4.3) upon firing once from immediate local excitation, we make the assumption that the time of the last i-spike in the cycle is most relevant to the dynamics of the network: that is, T_I is measured upto whichever is the last i-spike in that cycle	76
Figure 4.6	$\tau_e = 2, \delta = 7$. <i>Left</i> . An EPSP in an i-cell from the intrinsic e-cells alone evokes single spikes, e-cell in black, i-cell in red. <i>Right</i> . In the full network e-cells (blue and black overlaid) are synchronized through interneuron doublets (red)	79
Figure 4.7	The T_I map (left), and its slope (right) at $\tau_e=2$. Note that the slope $-1 < T_I' < 0$ for $\psi > 2.36$	80
Figure 4.8	The phase plot of synchronous behavior in the τ_e - δ plane around $\tau_e=3$. Traces of activity in the e-cells (black, blue) and the i-cells (red, green) are shown at points representative of the different regions with increasing δ . The plots are computed at values of delay $\delta = 0.5, 1, 4, 8, 9.7, 16$; $\tau_e = 3.0$. Note, in particular, the dots in red that mark where the slope of T_I evaluated for $\tau_e=3$, crosses -1	81
Figure 4.9	The T_I map at $\tau_e=3$. The red curve indicates a firing of triplets. For lower values of δ , however, the excitation does not arrive late enough to induce a third spike (blue). For $\delta > 6.9$ (broken curve), distal excitation can no longer influence the second spike	82
Figure 4.10	The slope of the T_I map in the “doublet” regime (left), and in the “triplet” regime (right) at $\tau_e=3$. The slope crosses the line $T_I'=-1$ at the points $\psi = 0.7, 1.9$ and 6.9 successively (left panel); and 11.61 (right). Notice that the rightmost point on the abscissa on the left is the same as the leftmost abscissa point on the right i.e. the two panels may be “concatenated” with respect to the horizontal axis. . .	83

Figure 4.11 $\tau_e = 3$, $\delta = 15$ (left), and 17. There is a 14 % heterogeneity in the drives to the two e-cells. For larger delays, synchrony is weaker	86
Figure 4.12 The T_I map (left), and its slope (right) at $\tau_e=4$. The slope curve in red is a piecewise polynomial fit to the numerical data (blue; overlaid). The slope crosses the line $T_I'=-1$ at the points $\psi = 0.35, 2.1, 4.58, 5.95$ successively	87
Figure 4.13 The slope of the T_I map in the “singlet” regime (blue), and in the “doublet” regime (red) at $\tau_e=1.5$. The slope crosses the line $T_I'=-1$ at the points $\psi = 0.9$ and again at 8.9. Note that at 7.2 the doublet is evoked soon enough to affect phase in the same cycle	87
Figure 4.14 The phase plot of synchronous behavior in the τ_e - δ plane around $\tau_e = 4$. Traces of activity in the e-cells (black, blue) and the i-cells (red, green) are shown at points representative of the different regions with increasing δ . The plots are computed at values of delay $\delta = 0.25, 1, 4, 5, 10$; $\tau_e = 4.0$. Note, the dots in red that mark where the slope of T_I evaluated for $\tau_e=3$, crosses -1	88
Figure 4.15 $\tau_e=1.5$, $\delta=0.5$, stable synchrony	89
Figure 4.16 $\tau_e=1.5$, $\delta=2$, the “alternating” pattern, but with only singlets	89
Figure 4.17 $\tau_e=1.5$, $\delta=5$, a fragment of an intricate pattern	90
Figure 4.18 chaos?	90
Figure 4.19 $\tau_e=1.5$, $\delta=7$, anti-synchrony	91

Chapter 1

Introduction

An incredible number of phenomena in nature show activity that is periodic, or very nearly so. From the beating heart to the diurnal rhythm, hurricanes, hormonal cycles and lattice vibrations in a quartz crystal, *oscillations* are ubiquitous. Man creates even more - swirling batons, traffic lights, cerium/citric-acid reagents and class schedules. Some of these rhythms can be altered easily; others are impossible to change. Interesting behaviors can occur when groups of these oscillators can influence each other. In the case of the heart, for example, periodicity is enforced by the sinoatrial node. But even in the absence of a *central pacemaker* driving the rhythm, cooperative behavior can sometimes lead to a surprising results: mutual entrainment is possible. Thus old watchmakers found it difficult to maintain good clocks, presumably because of the nearby clocks that kept a different time (Winfree [2]). Or in hordes of fireflies in Southeast Asia that, remarkably, flash *synchronously* at night (Buck [3]). In the case of the fireflies, it is already an achievement to consider if synchrony might be a property of oscillators coupled through the flashes of light rather than, say, chemical influences. Oscillators may be coupled through influences (perhaps periodic themselves) that last for long (compared to the period of oscillators), or only for short times.

Periodic activity can be studied in at least one special way: by looking at behavior as the system returns repeatedly to some specific state. For example, a particular state of the system of oscillators may be described by specifying the phases of all the oscillators whenever the phase of some reference oscillator is zero. The idea, then, is to describe a *return* to a particular *configuration*. A *map* that encodes this variation from cycle to cycle can be used to study *patterns of activity* in the pool.

In Chapter 1 we study groups of identical oscillators connected via pulsatile coupling. Any oscillator, when perturbed due to another, responds with a shift in its (own) phase. A graph that describes the phase shift as a function of time along the cycle when the influence is felt will be called the *phase response curve* (PRC). In many cases, a phase response curve for an oscillator can be measured experimentally, such as for neurons whose membrane potential can oscillate (and

which can be altered either by another neuron, or an artificial electrode stimulation). Our objective is to describe properties of mutually coupled oscillators (such as stability of synchrony), in terms of the PRC of an individual oscillator. We consider various topologies of the connectivity: global coupling (that, is every oscillator coupled to every other), rings, chains, arrays. We study (stability of) synchrony, and waves.

In Chapters 2 and 3, we will focus our attention on rhythms in the brain. That there is much periodic activity in the human body is quite obvious. There are the “mechanical” oscillations, such as respiration, and “chemical”, such as the menstrual cycle. There is another kind of periodic activity, *electrical*, in the action potential generation in nerves. Oscillatory activity in the nervous system is seen not only in, say, the sinoatrial nerve of the heart, but also rippled across MEGs and EEGs recorded from the brain. Thus EEG/MEG data show prominent bands of oscillatory activity, that have been code-named (by the frequency) *alpha* (8-12 Hz), *beta* (12-30 Hz), *gamma* (30-80 Hz), *delta* (6-8 Hz). Since they are often observed simultaneously with sensory processing and other cognitive states, speculations have been made that they may have functional roles to play. Modeling studies and experiments have considered (neuronal) network rhythms as arising from the biophysical properties of the underlying neurons (that can oscillate intrinsically) and their synaptic connectivities. It is not intuitive how this might arise. We shall focus primarily on gamma oscillations. Several authors (see for example, Traub and colleagues [4] and Whittington *et al* [5] and the references therein) have studied gamma oscillations *in vitro*, and in network simulations. Gamma oscillations can be shown to arise from recurrent synaptic connections among *interneurons*, inhibitory neurons that tend retard the activity of others that they are connected to.

In Chapter 2, we shall attempt to explain a rather surprising result of beta activity in humans with the use of the drug diapam. Benzodiazepines, such as diapam, are used clinically as sedatives (among their other uses), yet Jensen *et al* [6] find that beta band activity recorded in MEGs *increases* upon administering the drug. We model this behavior in a network of a few inhibitory and excitatory neurons. Significant to the model is a long-lasting current in the excitatory cells. Adaptation of this current on successive cycles influences features of the activity such as coherence in the network and peak of the power spectra. We shall be able to use a map of activity on successive cycles to analyze the behavior of spiking cells in our network. We use it to predict the specific inhibitory action of the drug.

In Chapter 3 we return to a model for generating gamma rhythms that was used by Ermentrout and Kopell [7] to explain long range synchrony of these neuronal populations (as seen in culture). Ermentrout-Kopell used a model with populations reduced to a four neurons: a pair of excitatory and inhibitory neurons coupled with conduction delays. Synchrony was shown to mediated by rapid spike “doublets” evoked in succession in the interneurons via delayed excitation from the distal populations. Fuchs *et al* [1] studied the effect of prolonging the excitatory influence onto cells on long-range synchrony in transgenic mice. They found that while the oscillation (gamma) continued to persist, synchrony was disrupted. We use the framework of Ermentrout and Kopell to understand these results. In the formalism of the reduced model, the firing times on a cycle are determined by the times of firing of the cells in the network on previous cycles. We shall show that it is possible to study the patterns of activity in the network (while also explaining the experiments of Fuchs *et al*), through a single variable: the timing response of a single inhibitory cell to excitatory impulses received at different phases in its period.

The unifying theme across all these problems is that of the “timing map”. Periodic activity can be studied by charting the development of some variables of the problem on successive *cycles*.

Chapter 2

Synchrony, Stability, and Firing Patterns in Pulse-Coupled Oscillators

2.1 Introduction

There have been many recent investigations of the behavior of coupled networks of neural oscillators. A large body of experimental data indicates that brief periods of oscillatory activity may be required for certain cognitive functions (see Gray [8], for references). Many theoretical approaches have been applied to the general question of synchrony and phase-locking (Winfree [2]; Kuramoto [9]). These include restriction of the models to simple neurons like the integrate-and-fire model (Mirollo and Strogatz [10]; Bressloff and Coombes [11]; van Vreeswijk *et al* [12]), weak coupling (Ermentrout and Kopell [13]; Ermentrout [14]; Hansel *et al* [15], and simple topologies (Dror *et al* [16]; Canavier *et al* [17]). In many of these papers, the coupling is pulse-like lasting only briefly relative to the length of the cycle. In this chapter, we focus on the behavior of such pulse-coupled oscillators motivated by the fact that the coupling between neurons is often through rapidly decaying synapses.

When a stable oscillator is briefly perturbed by a sufficiently small stimulus, then, the phase of the oscillator is shifted by an amount that depends on the timing of the perturbation (Winfree [2]; Kopell [18]). The change in phase of the oscillator is called the phase-response curve (PRC). PRCs are popular among experimentalists as they provide a way to quantify the behavior of the system without knowing the underlying mechanisms responsible for the behavior. Indeed, PRCs have been computed for many biological oscillators (Winfree [2]; Buck [3]), including neurons (Reyes and Fetz [19]; Stoop *et al* [20] have used experimental PRCs to devise coupled map lattices for arrays of nearest neighbor coupled neurons. Canavier and colleagues have taken a different approach and analyzed rings of uni-directionally coupled PRCs without forcing. Our approach is similar but not restricted to uni-directional coupling.

The general plan of this chapter is as follows: we first define PRCs and then derive a set of

discontinuous differential equations representing the phases of the respective oscillators. The PRC is a *timing curve* that encodes the response of a *single* oscillator to perturbations received at different points in its cycle. (We will sometimes describe the PRC also as a timing “map”, in the sense of a function; this connotation will be clear in context). We then use the PRC to study properties (i.e. firing patterns) of oscillators connected into *networks*. The objective is to derive *maps* for the (various) networks as a discrete dynamical systems, which under iteration produce the asymptotic behavior of the oscillators. We describe the timing difference for a single periodically forced PRC and for a pair of coupled PRCs. We generalize this to a map for N globally coupled oscillators and prove a stability result. Surprisingly, the stability depends on the number of oscillators. We then turn to a ring of nearest neighbor coupled PRCs and derive conditions for the existence of traveling waves as well as their stability. We numerically simulate the ring and a line of coupled PRCs to show the differences. Finally, we consider two-dimensional arrays of nearest neighbor-coupled PRCs and show the existence of (apparently numerically stable) rotating waves.

Thus, we study behavior of groups of mutually-coupled oscillators in terms of the properties (in particular, the stably synchronous state) of individual oscillators. The oscillators themselves are often motivated by neuronal models (and will sometimes be called “neurons”). The differences between the various oscillator models are encoded in its response curve: the PRC. Of course, the PRC must itself be obtained in some *a priori* way: either from a given mathematical model, or from experiment. We seek to determine maps determining phases from cycle to cycle for the networks, in terms of the timing curves of single oscillators, i.e. the PRC. (Note that the oscillators - that is, the PRCs - are all identical in any particular network; the connection topology distinguishes one network from another.)

This work has been previously published as [21].

2.2 Phase response curves and coupled phase models

2.2.1 Defining the PRC

Suppose that a system has a stable limit cycle solution and that we are only interested in a particular event within that system. For example, we might only be interested in the times at which a given neuron fires an action potential. At some fixed time after a spike, we briefly perturb

the system (e.g., we inject a current pulse into the neuron). This perturbation changes the time of the next spike. The change in timing is the phase response curve and it is a function of the magnitude and the timing of the perturbation. Let T be the natural period of the oscillation and let $t = 0, T, 2T, \dots$ be the times of successive events. Suppose that at $t = t_s \in [0, T)$ we perturb the trajectory. Then, the new firing time is $\hat{T}(t_s)$. A major assumption of PRC theory is that the events that occur after $t = \hat{T}(t_s)$ are at $t = \hat{T}(t_s) + T, \hat{T}(t_s) + 2T, \dots$. This says that the effect of the perturbation is only carried for one cycle; there is no memory of the perturbation once the event has occurred. This is a rather severe restriction, but, in practice, it often holds. (However, in Reyes and Fetz [19], there is a small change in the next spike time due to the presence of a slow potassium current.) That is, the second spike after the stimulus occurs at $t < \hat{T}(t_s) + T$ but this difference is quite small compared to the initial phase-shift due to the perturbation.) We define the phase-response curve to be:

$$\Delta(\phi) \equiv 1 - \frac{\hat{T}(T\phi)}{T} \quad (2.1)$$

where $\phi \equiv t_s/T \in [0, 1)$ is the phase. Thus, $\Delta(\phi)$ is positive (negative) if the effect of the stimulus is to advance (retard) the time of the next event. Most neurons have phase response curves that satisfy

$$\Delta(0) = \lim_{\phi \rightarrow 1^-} \Delta(\phi) = 0.$$

This means that the spike time is unchanged if the perturbation arrives at the onset of the spike. The PRCs computed for excitatory pyramidal neurons as well as inhibitory cortical neurons have this property. (An example PRC from Reyes and Fetz is shown in Figure 2.3; Figure 1 in Stoop [20] shows PRCs for both excitatory and inhibitory perturbations.)

2.2.2 Some exactly computable PRCs

In this section, we briefly describe PRCs for several classic model oscillators which have appeared in the literature. The first example is the well-known integrate-and-fire model:

$$\frac{dV}{dt} = -V + I$$

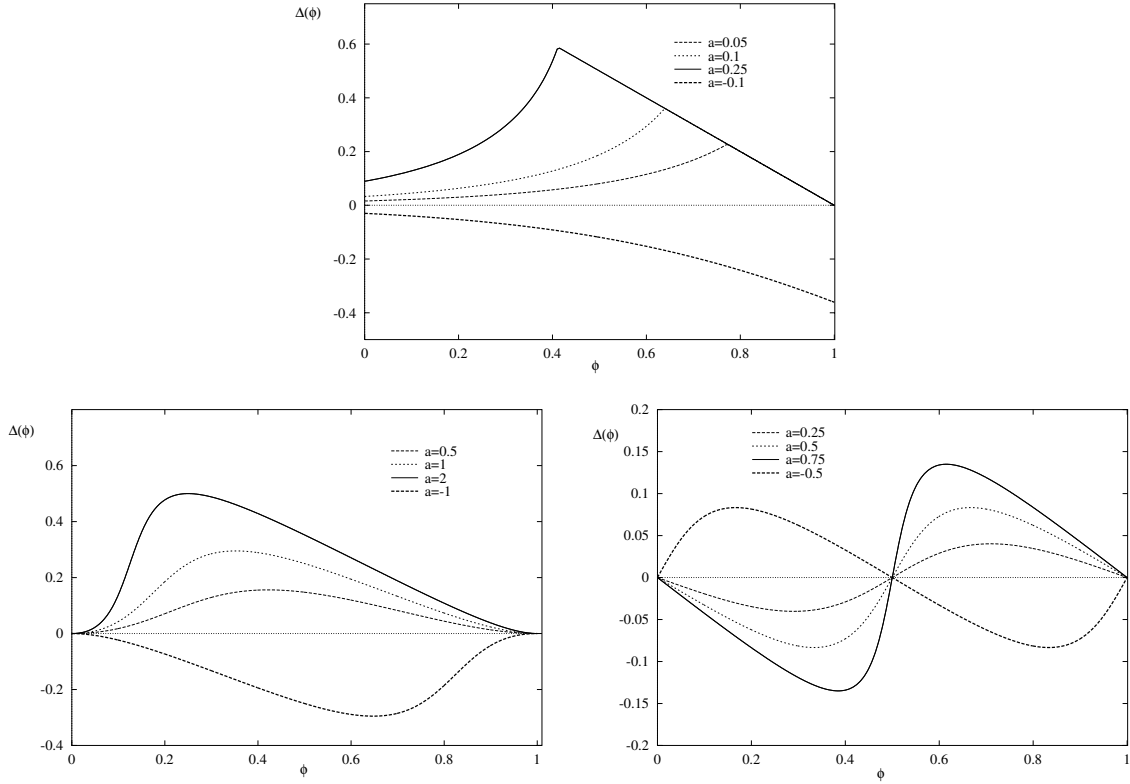


Figure 2.1. The PRCs for the integrate-and-fire model (top); the quadratic integrate-and-fire model (middle) and the radial-isochron clock (bottom).

with $V(t^+) = 0$ when $V(t^-) = 1$. We assume that $I > 1$ so that this oscillates with a period of

$$T = -\ln \frac{I-1}{I}.$$

At $t = t_s$ we add an amount a to V and then ask when the oscillator will fire next. If the t_s is close enough to $t = T$ then the perturbation a will lift V past 1 and the oscillator will fire immediately so that $\hat{T}(t_s) = t_s$. Otherwise, an elementary calculation shows that

$$\hat{T}(t_s) = -\ln \frac{I-1}{I - ae^{t_s}}.$$

Figure 2.1a shows the PRC for the integrate-and-fire model for $I = 1.05$ and various values of a . For $a > 0$ the PRC never satisfies $\Delta(0) = 0$ and for $a < 0$ it satisfies neither the condition that $\Delta(0) = 0$ nor $\Delta(1) = 0$.

Another version of the integrate-and-fire model is the “quadratic” integrate and fire equation:

$$\frac{dx}{dt} = I + x^2$$

with firing defined at $x(t) \rightarrow \infty$ after which x is reset to $-\infty$. The period is just

$$T = \int_{-\infty}^{\infty} \frac{dx}{I + x^2} = \frac{\pi}{\sqrt{I}}$$

This model arises as the normal form for a limit cycle near a saddle-node (see Ermentrout [22]; Hoppensteadt and Izhikevich [23]). As above, we assume that at $t = t_s$ a perturbation of size a is given. Then, an elementary calculation (see e.g. Hoppensteadt and Izhikevich) shows that

$$\hat{T}(t_s) = t_s + \frac{1}{\sqrt{I}} \left(\frac{\pi}{2} - \arctan \left[\frac{a}{\sqrt{I}} - \cot(\sqrt{I}t_s) \right] \right).$$

In Figure 2.1 we show the PRC for $I = 1$ and various values of a . Unlike the integrate-and-fire model, the PRC for this model vanishes at both 0 and T regardless of the strength of the perturbation. In this sense, it is a much “better” representation of what a real neuron does.

As a final example, we take the classic radial isochron clock (Glass and Mackey, [24], p107) a two-dimensional system that is a simplified normal form for any system near a Hopf bifurcation:

$$\frac{dr}{dt} = \Lambda r(1 - r^2) \quad \frac{d\theta}{dt} = 1.$$

This is the polar form of the oscillator, so $\theta \in S^1$. Firing is defined as $\theta = 0$ and perturbations are defined as shifts in the x -coordinate of length a . The parameter Λ is assumed to be very large so that perturbations are immediately brought back to the limit cycle along radii (see Fig 2.2). In order for “phase” to be defined, we require that $|a| < 1$ (note that if $|a| > 1$, then a perturbation at $\theta = \pi$ would “relax” to $\theta = 0$ - since $r = 0$ is an unstable fixed point of the dynamics - i.e. produce a phase shift of 0.5). As above, t_s is the time after firing that the pulse is given so that in the plane, $(x, y) = (\cos t_s, \sin t_s)$. After the pulse, the coordinates are $(a + \cos t_s, \sin t_s)$. The new

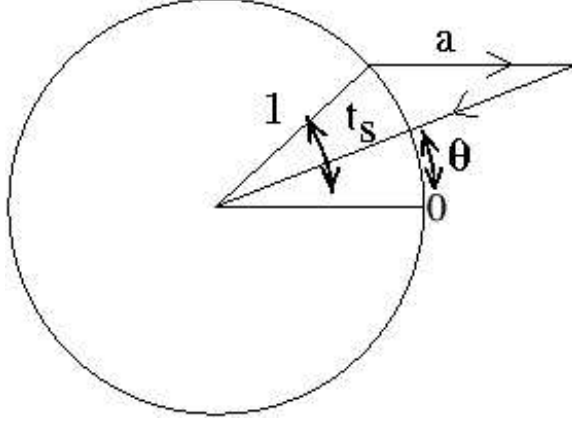


Figure 2.2. The effect of a perturbation on the radial isochron clock.

angle, θ is obtained from trigonometry:

$$\tan \theta = \frac{\sin t_s}{a + \cos t_s},$$

thus

$$\hat{T}(t_s) = t_s + 2\pi - \arctan \left(\frac{\sin t_s}{a + \cos t_s} \right)$$

Figure 2.1c shows the PRC for the radial isochron clock. Unlike the other two models, for a given value of a , the PRC can both advance and delay the firing. As $a \rightarrow 1$ the PRC becomes singular. Note that no matter what the value of a the PRC vanishes at $t = 0, T$. For small values of a , the radial isochron clock PRC has a particularly simple form:

$$\Delta(\phi) = -\frac{a}{2\pi} \sin 2\pi\phi. \quad (2.2)$$

We will use this form later on when we analyze coupling in lattices.

Cortical neuron PRCs that have been measured generally either strictly advance (for positive perturbations) or delay (for negative perturbations) the phase. However other neural PRCs can both advance and delay. (See for example the PRCs computed for the firefly, *Pteroptyx malacca*, Buck [3], Figure 4, and the fruitfly *Drosophila pseudoobscura* pupae, Winfree, [2], Figures 5-7, pp 414. These PRCs looks similar to the small a version of the radial isochron clock.) It is easy to

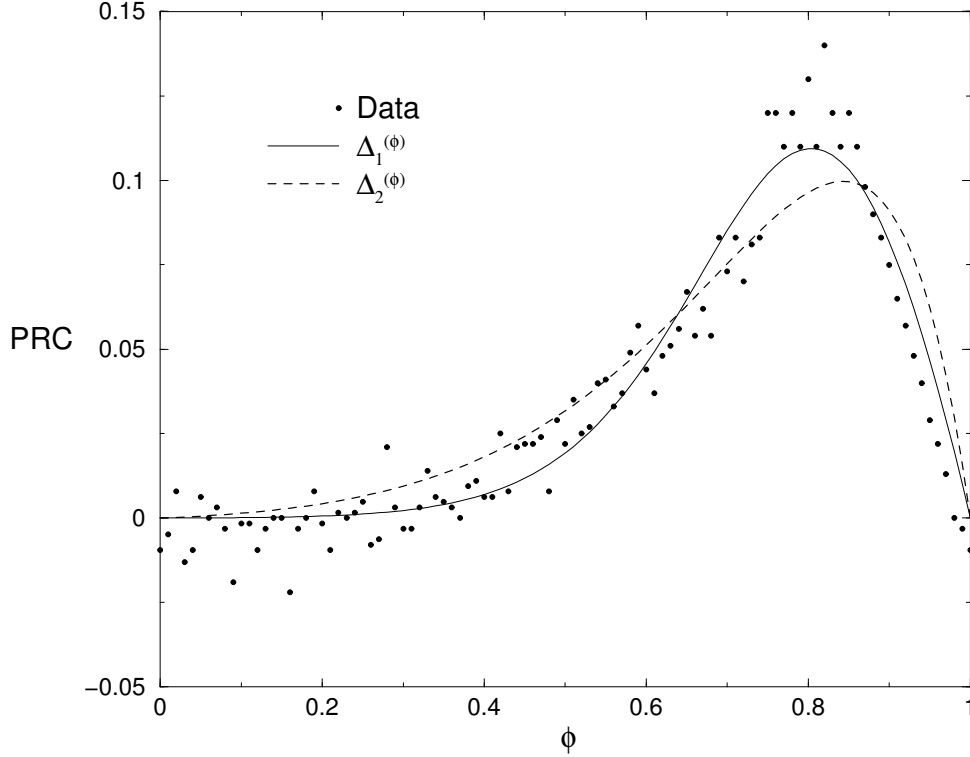


Figure 2.3. Experimentally measured PRC (Reyes *et al*) and two approximations.

compute the PRC for model neurons as well. Hansel *et al* [15] do this for the Hodgkin-Huxley model and the Connor-Stevens model. In the former, the PRC both advances and delays while in the latter, the PRC only advances the phase. In cortical PRCs such as measured by Reyes and Fetz [19] we find the following two classes of functions to be a good fit:

$$\Delta_1(\phi) = a \frac{\phi(1-\phi)}{1 + e^{-c(\phi-b)}}, \quad (2.3)$$

with $c \geq 0, 0 < b < 1$ and

$$\Delta_2(\phi) = a\phi(1-\phi)e^{-p\phi-q(1-\phi)} \quad (2.4)$$

with $0 < p < q$.

These are plotted in Figure 2.3 along with the data from Reyes and Fetz [19]. Parameters for the fits were chosen using least squares. The former function provides a better fit however the latter allows us more flexibility in varying the shape of the PRC.

2.2.3 The Geometry of PRCs

Let $\mathbf{X}_0(\mathbf{t})$ be an asymptotically-stable limit cycle solution to an n -dimensional system of ordinary differential equations

$$\frac{d\mathbf{X}}{dt} = \mathbf{F}(\mathbf{X}) \quad (2.5)$$

with period T , $\mathbf{X}_0(\mathbf{t} + \mathbf{T}) = \mathbf{X}_0(\mathbf{t})$. And let the vector field be perturbed as

$$\frac{d\mathbf{X}}{dt} = \mathbf{F}(\mathbf{X}) + \epsilon\mathbf{G}(\mathbf{X}) \quad (2.6)$$

where $\epsilon\mathbf{G}(\mathbf{X})$ represents a small perturbation (depending on \mathbf{X}), and $0 < \epsilon \ll 1$. For a strongly attracting limit cycle, periodic motions can be expected to persist despite the perturbation $\epsilon\mathbf{G}(\mathbf{X})$. If C is the curve corresponding to $\mathbf{X}_0(\mathbf{t})$, then one may associate with each point on C a scalar, ϕ , such that its velocity along C is uniform,

$$\frac{d\phi(\mathbf{X})}{dt} = 1, \quad \mathbf{X} \in C. \quad (2.7)$$

ϕ is the phase defined *on* C . To extend the definition of phase to points lying outside (but close to) C , we consider a tubular neighborhood, M , of the limit cycle that contains domain of attraction of C . The phase of a point Q in M , but not on C , is defined to be identical to the phase of that point on C to which it approaches in the asymptotic limit. That is, if $Q \rightarrow P$ as $t \rightarrow \infty$, then $\phi(Q) = \phi(P)$. The locus of all such points $Q \in M$ with the same phase as P is an $(n - 1)$ -dimensional surface termed an *isochron* (Winfree [25], Guckenheimer [26]), and denoted by $I(\phi)$ in Figure 2.4. If we take a stroboscopic map of the unperturbed system at times $t = nT$ ($n = 0, 1, 2, \dots$), then any point on a particular isochron will continue to remain on that isochron, and will move closer and closer to C with n . We have then, extending Equation (2.7) to M ,

$$\frac{d\phi(\mathbf{X})}{dt} = 1, \quad \mathbf{X} \in M. \quad (2.8)$$

Since

$$\frac{d\phi(\mathbf{X})}{dt} = \nabla\phi \cdot \frac{d\mathbf{X}}{dt}, \quad (2.9)$$

using Equation (2.5), we have

$$\nabla\phi \cdot \mathbf{F}(\mathbf{X}) = 1, \quad \mathbf{X} \in \mathbf{M}. \quad (2.10)$$

To obtain an expression for $d\phi(\mathbf{X})/dt$ when the system is perturbed we have

$$\begin{aligned} \frac{d\phi(\mathbf{X})}{dt} &= \nabla\phi \cdot \frac{d\mathbf{X}}{dt} \\ &= \nabla\phi \cdot [\mathbf{F}(\mathbf{X}) + \epsilon\mathbf{G}(\mathbf{X})] \\ &= 1 + \epsilon \nabla\phi \cdot \mathbf{G}(\mathbf{X}) \end{aligned} \quad (2.11)$$

for $\mathbf{X} \in \mathbf{M}$. However, in this case a state point typically migrates from the isochron it was restricted to in the unperturbed case. If we restrict to the case of small perturbation, we may assume that any point on C does not deviate very far from the limit cycle when the perturbation is turned on. That is, $|\mathbf{X} - \mathbf{X}_0(\phi)| \rightarrow \mathbf{0}$ as $\epsilon \rightarrow 0$, where $\mathbf{X}_0(\phi)$ is the intersection of C and the isochron containing \mathbf{X} . Under this assumption, to the lowest-order we can approximate \mathbf{X} on the right hand side of Equation (2.11) with \mathbf{X}_0 :

$$\begin{aligned} \frac{d\phi(\mathbf{X})}{dt} &= 1 + \epsilon \mathbf{Z}(\phi) \cdot \mathbf{G}(\mathbf{X}_0(\phi)), \quad \text{where} \\ \mathbf{Z}(\phi) &= (\nabla\phi)_{\mathbf{X}=\mathbf{X}_0} \end{aligned} \quad (2.12)$$

If however, the perturbation is not small, i.e. $\epsilon = 1$, then the previous discussion leading to Equation (2.12) is not valid. However, immediately after the perturbation the state point is on *some* isochron of the unperturbed dynamics (assuming the an isochron exists at that point). Thus, both before and after the perturbation, the dynamics obey the unperturbed equation:

$$\frac{d\phi(\mathbf{X})}{dt} = 1. \quad (2.13)$$

So that for a delta function perturbation

$$\frac{d\phi(\mathbf{X})}{dt} = 1 + \delta(t - t_s) \Delta(\phi) \quad (2.14)$$

where the PRC is defined through,

$$\Delta(\phi) = 1 - \frac{\hat{T}(t_s)}{T}. \quad (2.15)$$

We note that the Equation (2.15) is valid even if the perturbation is not delta-like, but transient (and lasts for a time smaller than the unperturbed period, T). Very often, it is not clear what the form of the coupling is. In the absence of a set of model equations for the oscillator, equation (2.15) shows that one can measure a PRC experimentally by applying brief pulses at different phases and measuring the change in period.

But let us suppose that the coupling is through one component X_i . For example, Hodgkin-Huxley cells are usually coupled in the voltage equations. If the perturbation is a brief positive pulse (at time t_s) i.e. a delta function, then Equation (2.12) reduces to

$$\frac{d\phi(\mathbf{X})}{dt} = 1 + \epsilon \delta(t - t_s) Z_i(\phi) \quad (2.16)$$

and $Z_i(\phi)$ can be recognized as the “infinitesimal” PRC (computed as the $\lim_{\epsilon \rightarrow 0} \frac{\Delta(\phi)}{\epsilon}$). It was

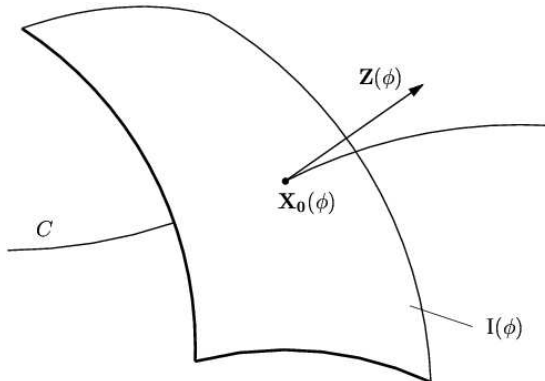


Figure 2.4. The geometry of equation Equation (2.12).

shown in Ermentrout [27] that the infinitesimal PRC can be computed as the i^{th} component of the solution to the adjoint equation:

$$\frac{d\mathbf{X}^*}{dt} = -D\mathbf{F}(\mathbf{X}_0(\mathbf{t}))^T \mathbf{X}^*, \quad \mathbf{X}^*(\mathbf{t}) \cdot \mathbf{X}'_0(\mathbf{t}) = \mathbf{1}. \quad (2.17)$$

In our theory we assume throughout that the coupling is pulsatile i.e. delta-like, and the limit cycle is strongly attracting (the state point relaxes to the limit cycle infinitely fast; the PRC is a function only of phase). Thus two stimuli in succession result in a phase reset composed as $F(F(\phi))$, with $F(\phi) = \phi + \Delta(\phi)$. We remark that Equation (2.14) might suggest that the PRC due to two (or more) pulses arriving at *exactly* the same phase is computed from a *linear* sum over inputs. This is not necessarily the case. For example, a synapse that saturates after a single action potential will not respond to another (near simultaneous) input with any further increase in conductance. We shall retain only the phase of the stimulus, so we assume that the phase reset continues to be $F(\phi)$ regardless of the number of simultaneous inputs.

2.2.4 Coupling with PRCs

Suppose that one has computed a PRC. Then how can we use this to analyze the coupling between oscillators? The easiest way to think about this is to first consider a single oscillator that is periodically driven with a pulsatile stimulus. Assume that every P time units, a stimulus of strength a is given to the system. Then the phase right *before* the time of the n^{th} stimulus is

$$\hat{\theta}_n = \theta_{n-1} + \frac{P}{T}$$

where θ_{n-1} is the phase right *after* the $(n-1)^{\text{th}}$ stimulus. The phase *after* the n^{th} stimulus is thus

$$\theta_n = \hat{\theta}_n + \Delta(\hat{\theta}_n) = \theta_{n-1} + \frac{P}{T} + \Delta(\theta_{n-1} + \frac{P}{T})$$

which gives a map for the phase. Let $\phi = \theta + P/T$. Then we get the more standard map:

$$\phi_n = \frac{P}{T} + \phi_{n-1} + \Delta(\phi_{n-1}) \equiv \frac{P}{T} + F(\phi_{n-1}). \quad (2.18)$$

We call $F(\phi) = \phi + \Delta(\phi)$ the *phase transition map* and it describes what the new phase is as a function of the old phase. This class of circle maps has been analyzed by many people. Glass and Mackey (1988) provide a good overview of circle maps. We note here that if $F'(\phi) > 0$ then the map is invertible and there is no chaotic behavior.

Another way to formally describe the periodic driving is to embed the map into a discontinuous

differential equation:

$$\frac{d\theta}{dt} = \frac{1}{T} + \delta_P(t)\Delta(\theta)$$

where

$$\delta_P(t) = \sum_n \delta(t - nP)$$

and $\delta(t)$ is the Dirac delta function. The solution to this differential equation between the n^{th} and $(n+1)^{\text{th}}$ stimulus is just

$$\theta(t) = \theta(nP) + \Delta(\theta(nP)) + t/T,$$

and if we let ϕ_n be defined as the phase right after the n^{th} stimulus, $\phi_n = \theta(nP) + \Delta[\theta(nP)]$, then we get the map (2.18). This formal version of the forced map leads us easily to the obvious way of coupling PRCs:

$$\frac{d\theta_j}{dt} = \frac{1}{T_j} + C \sum_{n,k} \delta(t - t_k^n) \Delta_{jk}(\theta_j) \quad (2.19)$$

where t_k^n is the n^{th} time that the k^{th} oscillator fires, $\Delta_{jk}(\theta)$ is the effect on the phase of the j^{th} oscillator by the k^{th} oscillator firing, and C is the overall coupling strength. Note that $\Delta_{jk} = 0$ if oscillator k is not connected to oscillator j . Dror *et al* and Canavier *et al* assume this form of coupling in their series of papers. Hoppensteadt and Izhikevich derive a similar model from synaptically coupled neurons near a saddle-node bifurcation. Winfree [28] replaces the Dirac-delta functions with a smooth pulsatile periodic function. The case of all-to-all coupling of the Winfree model was recently analyzed by Ariaratnam and Strogatz [29]. Ermentrout and Kopell [30] also replace the delta functions with smooth functions and analyze the resulting systems of equation. They derive the smoothed version from general neural net equations.

Stoop *et al* [20] consider an alternative means of coupling between PRCs which is akin to “diffusive” coupling and coupled map lattices:

$$\phi_j(n+1) = (1 - C)F(\phi_j(n)) + \frac{C}{m} \sum_k F(\phi_k(n))$$

where the sum is over connections and m is the number of such connections. A biological interpretation of this form of coupling was not suggested.

2.2.5 “Weak” coupling

Before turning to our results on “strong” coupling, we consider a limiting case when C is small. We assume that $C = \epsilon \ll 1$ is a small number and $1/T_j = 1 + \epsilon\omega_j$. We let $\theta_j(t) = t + \phi_j(t)$. For ϵ small, $t_j^n \approx n + \phi_j(t)$ so we obtain:

$$\frac{d\phi_j}{dt} = \epsilon \left(\omega_j + \sum_{k,n} \delta(t - n + \phi_k) \Delta_{jk}(t + \phi_j) \right).$$

Averaging this over one period leads to

$$\frac{d\phi_j}{dt} = \epsilon \left(\omega_j + \sum_k \Delta_{jk}(\phi_j - \phi_k) \right) + O(\epsilon^2). \quad (2.20)$$

Phase equations such as this have been analyzed by numerous authors and have been shown to have many different non-trivial phase-locked solutions (Ermentrout [31]). Thus, it should not be surprising that (2.19) also has a variety of different complex behaviors. We note that a phase-locked solution to (2.20) has the form,

$$\phi_j = \Omega t + \bar{\psi}_j$$

where $\bar{\psi}_j$ is a constant and Ω is a constant determined from the equations. A sufficient (but not necessary) condition for stability of this solution is $\Delta'_{jk}(\bar{\psi}_j - \bar{\psi}_k) \leq 0$.

2.2.6 Smooth pulsatile coupling

One other way to approach the instantaneous pulsatile coupling implicit in the definition of the PRC is to study a “smoothed” version:

$$\frac{d\theta_j}{dt} = \omega_j + \sum_k P(\theta_k) \Delta_{jk}(\theta_k)$$

where $P(\theta)$ is a smooth periodic pulse-like function centered at 0. For example,

$$P(\theta) = A_m(1 + \cos \theta)^m$$

where A_m is chosen so that the integral of P is 1. As m gets large, P will approach the Dirac δ function. Winfree [28] first posed this class of models and recently Ariaratnam & Strogatz analyzed the “all-to-all” coupled case for $m = 1$ and $\Delta_{jk}(\theta) = c \sin \theta$. In this brief section, we give a condition for the existence and stability of synchronous solutions. We assume the following:

- i. $\Delta_{jk}(\phi) = c_{jk}\Delta(\phi)$
- ii. $c_{jk} = c_{kj}$, $\omega_j = \omega$,

$$\sum_k c_{jk} = c,$$

and c is non-singular.

- iii. There is a solution to

$$\phi' = \omega + cP(\phi)\Delta(\phi) \tag{2.21}$$

satisfying $\phi(t + T) = \phi(t) + 2\pi$ for some finite positive T .

The first assumption says that the responses to any perturbation differ only in magnitude. The second assumption says that the coupling is homogeneous, the oscillators are identical, the coupling is symmetric, and nondegenerate. The third assumption says the oscillators don’t get stuck at fixed points. With these assumptions, a synchronous solution to

$$\frac{d\theta_j}{dt} = \omega + \sum_k c_{jk}P(\theta_k)\Delta(\theta_j) \tag{2.22}$$

exists, $\theta_j(t) = \phi(t)$. This is easily seen by substitution into (2.22) and using the homogeneity assumption and assumption (iii).

Suppose in addition, we have the following:

- iv. $c_{jk} \geq 0$,
- v.

$$Q \equiv \int_0^T P(\phi(t))\Delta'(\phi(t)) dt < 0.$$

Then, the synchronous solution is asymptotically stable.

Remark The integral Q is generalization of the “XZ” loop conditions that Winfree derives for all-to-all coupling for pulse-coupled oscillators (Winfree [28]).

To prove this, we linearize (2.22): $\theta_j(t) = \phi(t) + y_j$. To lowest order

$$\frac{dy_j}{dt} = \sum_k c_{jk} (P'(\phi(t))\Delta(\phi(t))y_k + P(\phi(t))\Delta'(\phi(t))y_k).$$

Recall that ϕ satisfies (2.21) so that if we differentiate this with respect to t we obtain:

$$\frac{d\phi'(t)}{dt} = (P'(\phi(t))\Delta(\phi(t)) + P(\phi(t))\Delta'(\phi(t))) \phi'(t).$$

Since $\phi'(t)$ is periodic, this means

$$\int_0^T P'(\phi(t))\Delta(\phi(t)) + P(\phi(t))\Delta'(\phi(t)) dt = 0$$

or

$$-\int_0^T P'(\phi(t))\Delta(\phi(t)) dt = \int_0^T P(\phi(t))\Delta'(\phi(t)) dt \equiv Q. \quad (2.23)$$

Let $\vec{\xi}$ be an eigenvector of the matrix c_{jk} with eigenvalue, λ . Since c_{jk} is nonnegative, nonsingular, and symmetric, it has a unique eigenvector with nonnegative components. (This is a consequence of the Frobenius-Perron theorem.) Since c_{jk} is homogeneous (i.e., its column sums are the same), this eigenvector is the vector of all 1's and the eigenvalue is c . Furthermore since c_{jk} is nonnegative and nonsingular, this is the maximal eigenvalue. Thus $c > \lambda$ for all $\vec{\xi} \neq \vec{1}$. The solutions to the linearized equation are

$$y_j(t) = x(t)[\vec{\xi}]_j$$

where $x(t)$ is a scalar satisfying:

$$x'(t) = (cP(\phi(t))\Delta'(\phi(t)) + \lambda P'(\phi(t))\Delta(\phi(t))) x(t).$$

Integrating this over a period, we see that $x(t)$ will decay if and only if

$$M \equiv \int_0^T (cP(\phi(t))\Delta'(\phi(t)) + \lambda P'(\phi(t))\Delta(\phi(t))) dt < 0.$$

Using (2.23), we see that

$$M = Q(c - \lambda).$$

Since $c > \lambda$, then a necessary and sufficient condition for stability of the synchronous state is that $Q < 0$ which is assumption (v). Note that there is a single zero eigenvalue corresponding to the time-translation invariance of the periodic solution.

We remark that this integral condition can be understood intuitively. Suppose that $\Delta'(\phi)$ is negative near the origin. (For example, in the radial isochron clock, this is true.) Suppose that $P(\phi)$ is positive and rapidly falls off to zero away from the origin. Then the integral quantity, Q will be negative as required. We also remark that this condition is analogous to the condition for the weakly coupled case. Indeed, the “weak interaction” function is

$$H(\phi) = \frac{1}{T} \int_0^T \Delta(t + \phi) P(t) dt.$$

The condition for stability of the synchronous state is $H'(0) < 0$ which is equivalent to $Q < 0$.

2.3 Two oscillators

We now consider a pair of mutually coupled PRCs and derive a one-dimensional map. For simplicity we will assume identical frequencies. We assume that the function $F(x) = x + \Delta(x)$ is invertible ($F'(x) > 0$). This has several important consequences:

1. No stimulus can cause a neuron to fire immediately. The phase can be advanced but never sufficiently to induce instant firing. This means that if $x < 1$ then $F(x) < 1$ as well. Since $F(1) = 1$ and F is monotone increasing $F(x) < 1$ for $x < 1$.
2. Similarly, invertibility means that the phase of an oscillator can never be brought below 0.

This assumption holds if the coupling is not too strong.

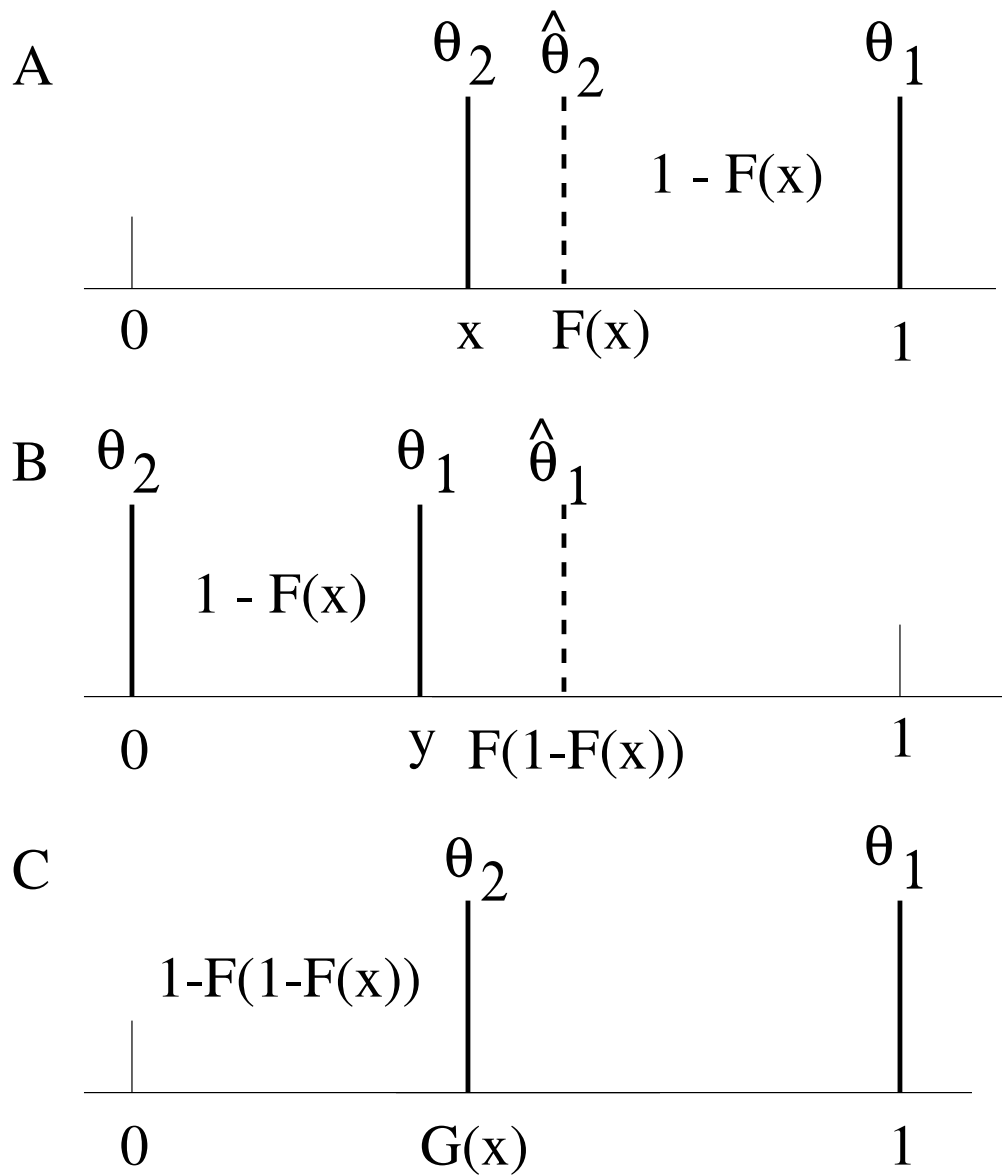


Figure 2.5. Construction of the map, $x \mapsto G(x)$ for a pair of coupled PRCs.

2.3.1 Locking

We assume identical frequencies in order to obtain an ordering principle for the oscillators. The pair of oscillators satisfies the formal differential equation:

$$\begin{aligned}\frac{d\theta_1}{dt} &= 1 + \sum_k \delta(t - t_2^k) \Delta(\theta_1) \\ \frac{d\theta_2}{dt} &= 1 + \sum_k \delta(t - t_1^k) \Delta(\theta_2)\end{aligned}$$

where $t_{1,2}^k$ are the times at which oscillators 1 and 2 fire. Suppose that θ_1 is ahead of θ_2 . Then invertibility of F implies that θ_1 will always be ahead of θ_2 if they have identical frequencies. This is because the firing of θ_1 can never push θ_2 past 1 nor can θ_2 pull θ_1 below 0. If the frequencies are different, then it becomes more difficult to describe a map. Figure 2.5 describes the construction of the map. Suppose that at the moment that θ_1 crosses 1, $\theta_2 = x$. Then immediately after firing, the new phase of θ_2 is $\hat{\theta}_2 = F(x)$. θ_1 is reset to 0 and θ_2 will then fire at $t = 1 - F(x)$ by which time θ_1 has advanced to $y = 1 - F(x)$. θ_1 is mapped to $\hat{\theta}_1 = F(y) = F(1 - F(x))$. It takes $1 - F(1 - F(x))$ amount of time for θ_1 to again reach 1 completing the map. Thus, the new value of θ_2 is found to be:

$$x \longrightarrow 1 - F(1 - F(x)) = x + \Delta(x) - \Delta(1 - x - \Delta(x)) \equiv G(x). \quad (2.24)$$

Fixed points of this map satisfy:

$$0 = \Delta(x) - \Delta(1 - x - \Delta(x)).$$

If $\Delta(0) = 0$ as we usually assume, then $x = 0$ is always a fixed point. That is, there is a synchronous solution. There can be other fixed points as well; generically at least one interior fixed point. For the maps (2.2-2.4) there are two roots: the synchronous root and the anti-synchronous root. The maps arising from both the radial isochron clock and the integrate-and-fire model also have two fixed points: a synchronous and anti-synchronous root. The quadratic integrate-and-fire map is degenerate, $G(x) = x$.

An alternate way of deriving a map is to consider the timing rather than the phases of the oscillators. Let T_1 be the last time that oscillator 1 fired and $T_2 > T_1$ be the last time that

oscillator 2 fired. Let T'_j denote the next firing time of each oscillator. Then

$$\begin{aligned} T'_1 &= 1 + T_1 - \Delta(T_2 - T_1) \\ T'_2 &= 1 + T_2 - \Delta(T'_1 - T_2) \end{aligned}$$

defines the firing time map since both oscillators have a frequency of 1. Letting $\phi = T_2 - T_1$ we recover the phase map.

2.3.2 Stability of the fixed points of the map

Let \bar{x} be a fixed point of (2.24). Stability is found by linearizing about \bar{x} leading to

$$G'(\bar{x}) = [1 + \Delta'(\bar{x})][1 + \Delta'(1 - \bar{x} - \Delta(\bar{x}))].$$

This is just the product of the derivative of the phase transition map evaluated at the phase of oscillator 1 when 2 fires and vice versa. Since each term is positive from the invertibility of $F(x)$, this means that the fixed point will be stable if the product of the terms is less than 1. In particular, the condition for stability of the synchronous solution is

$$\sigma = [1 + \Delta'(0^+)] [1 + \Delta'(1^-)] < 1. \quad (2.25)$$

Note that it is important that we take the correct limits for the PRC as often, a PRC does not have a continuous derivative. We can visually look at the PRC and determine if synchrony will be stable. For example, in the simple PRC (2.2) if $a > 0$ then $\Delta'(0) = \Delta'(1) = -a$ and thus $\sigma = (1 - a)^2 < 1$ provided that a is less than 2. For the PRC's illustrated in Figure 2.3, $\Delta'(0^+) = a_0 > 0$ and $\Delta'(1^-) = -a_1 < 0$ so that $\sigma = 1 + a_0 - a_1 - a_0 a_1$. If a_j is not too large, then a sufficient condition for stability is that $a_1 > a_0$ which clearly holds in the maps of Figure 2.3. Thus, synchrony is stable.

The anti-phase solution is unstable for the maps illustrated in Figure 2.3. For the simple sinusoidal map (2.2) we see that $\phi = 1/2$ is the anti-phase root and that it is unstable for $a > 0$ and stable for $-2 < a < 0$. The synchronous state is stable and the anti-phase solution unstable for the radial isochron clock if $a > 0$ while for $a < 0$ the situation is reversed.

2.3.3 All-to-all coupling

While the majority of this work is devoted to patterns seen with local coupling, we can say a few general things about the “all-to-all” coupled case in which every cell is identically connected to every other cell. This is reminiscent of the case studied by Mirolo and Strogatz (1993) for pulse-coupled integrate and fire models. They show that all initial conditions outside a set of measure zero converge to the synchronized state. In order to study all-to-all coupling, we need to make an important preliminary observation. Suppose (as we have throughout) that F is monotone and thus invertible. Then $1 \geq F(\theta_1) \geq F(\theta_2) \geq 0$ for all $1 \geq \theta_1 \geq \theta_2 \geq 0$. Thus, if oscillator 1 is ahead of oscillator 2, then after both receive stimuli, oscillator 1 is still ahead of oscillator 2. Furthermore, neither oscillator can be brought to firing by the stimulation nor can either oscillator be pushed to 0 since $F(1) = 1$ and $F(0) = 0$. This means that if we have an array of N all-to-all identically coupled oscillators, then the order of their firing is always preserved. To study the stability of synchrony, we will create a locally defined map after the perturbation away from synchrony is given. This perturbation will determine a set of firing times *which will be preserved*. We can now assume that they are labeled in order of their firing and from this derive the $N - 1$ dimensional map. The map is done in N pieces corresponding to the single firing of each of the N oscillators in a cycle. We will go through the case of $N = 3$ oscillators to illustrate how the map is constructed for general N . We label the oscillators $\theta_1, \theta_2, \theta_3$ and suppose that the firing order is 1-2-3. We start $\theta_1 = 1$ and $1 > \theta_2 > \theta_3 > 0$ and follow the evolution as θ_2, θ_3 fire and then θ_1 is brought up to firing. We define two variables x_2, x_3 which will represent the two oscillators *which are not firing* so that initially x_2 represents θ_2 and x_3 represents θ_3 . However, when oscillator 2 fires, x_2 will represent oscillator 3 and x_3 will represent oscillator 1 which will now be the furthest back in phase since it fired most recently. Once oscillator 2 fires, x_2 becomes oscillator 1 and x_3 becomes oscillator 2 as oscillator 3 is the next in line to fire. Once oscillator 3 fires, it goes to the back of the line and waits for oscillator 1 to fire again. We define three maps:

$$M_a(x_2, x_3) = (F(x_2), F(x_3)),$$

$$M_b(x_2, x_3) = (1 - x_2 + x_3, 1 - x_2),$$

and

$$M_c(x_2, x_3) = (F(1 - x_2 + x_3), F(1 - x_2)) = M_a(M_b(x_2, x_3))$$

The first map is the initial response of 2 and 3 to 1 firing. The time elapsing until 2 fires is thus $1 - x'_2$ where $x'_2 = F(x_2)$. At this point oscillator 3 has advanced to $1 - x'_2 + x'_3$ where $x'_3 = F(x_3)$. This advance without a firing is map M_b . Now, right after oscillator 2 fires, oscillator 3 has a phase $F(1 - x'_2 + x'_3)$ and oscillator 1 has a phase $F(1 - x'_2)$. This explains the form of M_c . We apply M_c one more time accounting for oscillator 3 firing. Finally we apply M_b one more time to bring θ_1 up to the threshold for firing. Thus, the map is:

$$(\theta_2, \theta_3) \longrightarrow M_b M_c M_c M_a(\theta_2, \theta_3).$$

This is defined only in the domain:

$$1 \geq \theta_2 \geq \theta_3 \geq 0$$

which as we have already noted is an invariant under these maps. The generalization to $N > 3$ oscillators is immediate. Synchrony is clearly a solution to this system (i.e. a fixed point). Stability is determined by linearizing about the fixed point, $(0, 0, \dots, 0)$. We consider two cases. In the simplest case, we suppose that the PRC is continuously differentiable at the origin. That is, $\Delta'(0^+) = \Delta'(1^-)$. This is true for the radial isochron clock and for the PRC of the Hodgkin-Huxley equations. However, it appears to not be true for the PRCs of cortical neurons and the models (2.3) and (2.4). If the PRC is continuously differentiable then $F'(0) = F'(1) \equiv \alpha$. However if the PRC is not continuously differentiable, then $F'(0) \equiv \alpha_0 \neq \alpha_1 \equiv F'(1)$. We will discuss this more difficult case shortly. In the former case, the linearized map is just

$$B = E^N \alpha^N$$

where the general form of E (the linearization of M_b) is:

$$E = \begin{pmatrix} -1 & 1 & 0 & 0 & \dots & 0 \\ -1 & 0 & 1 & 0 & \dots & 0 \\ \vdots & & & & & \\ -1 & 0 & 0 & \dots & 0 & 1 \\ -1 & 0 & 0 & \dots & 0 & 0 \end{pmatrix}$$

The $(N - 1) \times (N - 1)$ matrix E is just a permuted transpose of a companion matrix so that its characteristic polynomial is

$$p_E(\lambda) = \lambda^{N-1} + \lambda^{N-2} + \dots + \lambda + 1$$

whose roots are just the N^{th} roots of unity different from 1. These sit exactly on the unit circle so that the roots of B have magnitude α^N . From this we conclude that the synchronous fixed point is asymptotically stable if and only if $\alpha = F'(0) < 1$. “Excitatory coupling” for the Hodgkin-Huxley equations as well as for the radial isochron clock leads to locally stable synchrony with all-to-all coupling.

What about stability in the second case? Here, we no longer have the simple structure for the linearization. To see why, consider the synchronous solution, $(0, \dots, 0)$. One can see that

$$M_a(0, \dots, 0) = (1, \dots, 1)$$

so that linearization of $M_b M_a$ leads to the matrix:

$$A_1 = \text{diag}(\alpha_1, \dots, \alpha_1)E.$$

However application of M_c to the vector of 1’s leads to

$$M_c(1, \dots, 1) = (1, \dots, 1, 0)$$

and the linearization is:

$$A_2 = \text{diag}(\alpha_1, \dots, \alpha_1, \alpha_0)E.$$

Since $\alpha_0 \neq \alpha_1$ the matrix A_2 is not a scalar multiple of E . We continue in this manner up the chain of maps and find that at each point, we replace the bottom-most α_1 by an α_0 . We thus must study the spectrum of a matrix consisting of products of E and products of diagonal matrices which are not scalar multiples of the identity matrix. For example for the case $N = 3$ the linearization is:

$$B = \begin{pmatrix} -1 & 1 \\ -1 & 0 \end{pmatrix} \begin{pmatrix} -\alpha_1 & \alpha_1 \\ -\alpha_0 & 0 \end{pmatrix} \begin{pmatrix} -\alpha_1\alpha_0 & \alpha_1\alpha_0 \\ -\alpha_1\alpha_0 & 0 \end{pmatrix}$$

For the cases $N = 3, 4$, the resulting matrices B are upper triangular and the eigenvalues can be explicitly read off of the diagonals. In the case of $N = 3$, the eigenvalues are $\alpha_0^2\alpha_1, \alpha_0\alpha_1^2$ while for $N = 4$ they are $\alpha_0^3\alpha_1, \alpha_0^2\alpha_1^2, \alpha_0\alpha_1^3$. We show that is a general form for the eigenvalues. Thus, synchrony will be linearly stable if and only if each of the terms $\alpha^k\alpha^\ell$ is less than 1. That is:

THEOREM *The $N - 1$ eigenvalues of B are of the form: $\alpha_0^\ell\alpha_1^{N-\ell}$ where $1 \leq \ell < N$. Synchrony is stable for an N -dimensional all-to-all coupled PRC network if each of these is less than 1*

The proof of this theorem is in the Appendix.

This has an interesting implication. Suppose that $\alpha_0 > 1$ and $\alpha_1 < 1$ as is the case for the experimentally computed PRCs. Suppose that $\alpha_0\alpha_1 < 1$ so that a pair stably synchronizes. Since $\alpha_0 > 1$ we can find a sufficiently large k such that $\alpha_0^k\alpha_1 > 1$ so that a network with $k+1$ cells coupled in an all-to-all fashion does not have a stable synchronous solution while any smaller network does have a stable synchronous solution. The critical network size is thus $N = k + 1$ where k is the smallest integer larger than

$$-\frac{\log \alpha_1}{\log \alpha_0}.$$

For the cortical PRCs, α_0 is very close to 1 so that the network would have to be very large. However, it is easy to construct a simple PRC for which synchrony is stable for a pair but not for a three oscillator system. Take $\Delta(\theta) = a|\sin \pi\theta|/\pi$. Then $\alpha_0 = 1 + a$ and $\alpha_1 = 1 - a$. Synchrony is stable for the pair since the eigenvalue is $\alpha_0\alpha_1 = 1 - a^2$. However, for a network of 3 oscillators, the maximum eigenvalue is $\alpha_0^2\alpha_1 = 1 + a - a^2 - a^3$ which is greater than 1 if $a < (\sqrt{5} - 1)/2 \approx 0.618$.

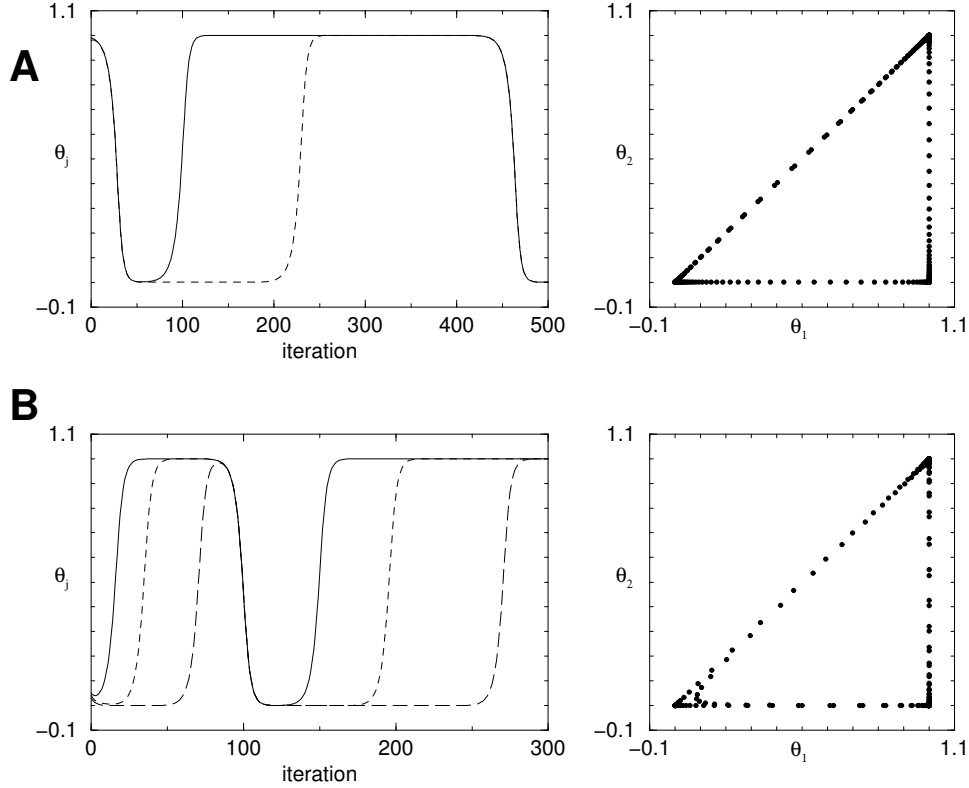


Figure 2.6. (A) The evolution of the phases for 3 all-to-all coupled PRCs (left) and the projection into the $\theta_2 - \theta_3$ phase-plane. (B) Same as A for 4 all-to-all PRCs.

Thus for small values of a synchrony is not a stable solution. A similar bound can be found for $N = 4$ oscillators: $a < a^* \approx 0.839$ then synchrony is unstable for 4 oscillators. We illustrate this point for $N = 3, 4$ oscillators in Figure 2.6. This shows the behavior of the map for $a = 0.2$ with initial data close to synchrony. The relative phases move around with longer and longer periods tending to synchrony for many iterates only to escape and drift around. This is quite similar to the approach of a dynamical system to a heteroclinic cycle. If we increase a past the critical value, then small perturbations from synchrony remain small and rapidly converge to the synchronous solution.

2.4 One-dimensional geometries

We now turn to one-dimensional geometries. The first case to consider is a chain of N coupled maps with nearest neighbor coupling:

$$\frac{d\theta_j}{dt} = 1 + \Delta(\theta_j)[\delta(\theta_{j-1}) + \delta(\theta_{j+1})] \quad (2.26)$$

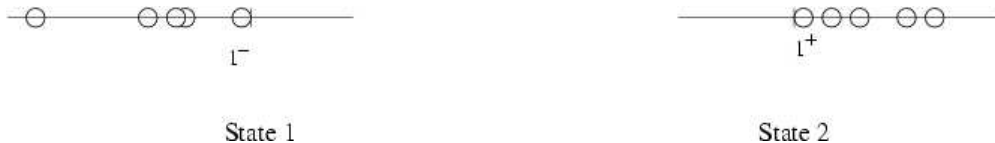
with the stipulation that the end oscillators receive only one input for the linear chain or, in the case of a ring, $N + 1$ is identified with 1 and N with 0. Clearly one solution to this equation is the synchronous solution since $\Delta(0) = 0$. (Note that for the integrate-and-fire PRC, $\Delta(0) \neq 0$ so that a simple linear chain cannot synchronize. Indeed, the oscillators in the middle advance by an amount $2\Delta(0)$ while the ends only advance by an amount $\Delta(0)$ so synchronization is impossible.) One can ask if synchrony is stable and furthermore if there are other possible solutions. The issue of stability remains open. In the case of a ring with $N = 3$, the network is actually all-to-all coupled and thus covered by our previous results. However, $N > 3$ remains an open problem. We conjecture that if the PRC is continuously differentiable at the origin, and if $0 < F'(0) < 1$, synchrony in both a ring and a linear chain is stable. This is certainly true for weak coupling since $F'(0) < 1$ implies that $\Delta'(0) < 0$ and thus the synchronous phase-locked state is stable. Furthermore, this is also consistent with the results for smooth-pulse coupling of section 2.2.6.

Conjecture Suppose that a group of oscillators is connected such that it is possible to reach any one oscillator from any other via connected links. Then synchrony is stable if $0 < F'(1) < 1$.

Argument We denote the phase of an oscillator i by θ_i . Let the oscillators be perturbed away from synchrony. Let some oscillator(s) be very close to firing, i.e. at 1^- . The phases of the other oscillators are close to 1; let $\{\theta_i\}$ denote these phases. We denote this stage, State 1. We are interested in the map that describes the phases of oscillators in State 1 on successive cycles.

Let us also denote the phase of an oscillator j , once it has fired, by $\bar{\theta}_j$. In what follows, it will be slightly more convenient to use $\bar{\theta}_j$ synonymously with its equivalent, $1 + \bar{\theta}_j$ (since phases are described on a periodic domain). (Similarly, we will consider the effect of coupling by using either the phase resetting curve, $F(\theta)$ (for $\theta < 1$), or its *lift*, $\bar{F}(\bar{\theta}) \equiv F(\bar{\theta} - 1)$, for $\bar{\theta} > 1$.) Once the last oscillator to fire (on the given cycle) has done so, let us also denote that stage, State 2. It is clear

that the State 1 that follows State 2, thus completing the cycle, is obtained from it by a simple translation of all oscillators by the same amount (i.e. no oscillator fires).



Consider State 1 on some cycle, and the State 2 that immediately follows it. Let us denote the maximum lower bound of the set of phases in State 1, $\theta^{max} \equiv \min\{\theta_i\}$, and the least upper bound of the phases after firing, in State 2, by $\bar{\theta}^{max} \equiv \max\{\bar{\theta}_j\}$. θ^{max} is the phase of the oscillator that is most distant from 1 in State 1, and $\bar{\theta}_j^{max}$ is the phase that is most distant from 1 in State 2. We show below that the strict inequality

$$(\bar{\theta}^{max} - 1) < (1 - \theta^{max}) \tag{2.27}$$

holds. Then construction of the map above shows that once we start with a given distribution of phases about synchrony, the phases continue to be bound to within this perturbation. Although (2.27) is not a sufficient condition to prove asymptotic stability of synchrony all numerical simulations that we have performed suggest that this is the case.

We will now make some assumptions on the nature of F , and the connection topology, to obtain a sufficient condition that guarantees (2.27) holds. We show this as follows:

Let us assume that (in addition to F being monotone and $F(1) = 0$) that

$$0 < F'(1) < 1. \tag{2.28}$$

This implies that

$$F(\theta_i) < \theta_i \text{ and } F(\bar{\theta}_j) < \bar{\theta}_j. \tag{2.29}$$

Condition (2.29) says that upon the firing of any oscillator m , the phase(s) of any oscillator(s) n , connected to it, are always pulled closer to 1. Let us also assume that the oscillators are connected such that there is always a path between every two oscillators in the group.

Let \bar{t} be the time between States 1 and 2, i.e. the time since the first oscillator to fire on the

cycle until the last. Then

$$\bar{t} \leq (1 - \theta^{max}) \tag{2.30}$$

. There are two cases possible:

Case 1. $\bar{t} < (1 - \theta^{max})$. Then $(\bar{\theta}^{max} - 1) \leq \bar{t} < (1 - \theta^{max})$, and the inequality (2.27) is satisfied.

Case 2. $\bar{t} = (1 - \theta_i^{max})$. This says that the last oscillator (say p) to fire is also the one that lags behind the most in State 1, and that its phase is not reset for $\theta^{max} < \theta_p < 1$. (Recall that $F(1) = 0$). Since this implies that every other oscillator m , that p is connected to, can only reset the phase of p at $\theta_m = \theta_p = 1$, m must be at exactly the same phase as p throughout. Since this is true for any m , it is true for all m ; this implies that all every cell is at the same phase. Thus, this is simply a re-statement that synchrony is a solution.

Although we have seen in numerics that the conjecture seems to hold, this argument is nevertheless incomplete because (2.27) is not sufficient to prove an asymptotic approach to zero.

2.4.1 Waves in a ring

In addition to synchrony, there are other possible solutions in a ring. The simplest such solution is a wave in which the timing interval between the firing of successive oscillators is constant. We now establish conditions for the existence of such a fixed timing wave by deriving an $N - 1$ -dimensional map valid near such a wave. As with the all-to-all coupled case, that map will advance the oscillator index as well as the phase. Suppose that oscillator N has fired and all the remaining oscillators coupled to N (e.g. $N - 1$ and 1) have also been reset. The next oscillator to fire will be oscillator 1 since the sequence is assumed to be $1 \rightarrow 2 \rightarrow \dots \rightarrow N$. The amount of time that it takes for oscillator 1 to reach firing is $1 - \theta_1$ so that oscillator $j < N$ will have advanced to $\theta_j + 1 - \theta_1$ and oscillator N will have advanced to $1 - \theta_1$. Oscillator 2 and oscillator N receive inputs from oscillator 1 (since it is nearest neighbor coupling) thus they both will receive a resetting pulse so that their respective phases are $F(1 - \theta_1 + \theta_2)$ and $F(1 - \theta_1)$. We are now back to where we started

but shifted forward one step. Thus, we obtain the following $N - 1$ -dimensional map:

$$\begin{aligned}
\theta'_1 &= F(1 - \theta_1 + \theta_2) \\
\theta'_2 &= 1 - \theta_1 + \theta_3 \\
&\vdots = \vdots \\
\theta'_{N-2} &= 1 - \theta_1 + \theta_{N-1} \\
\theta_{N-1} &= F(1 - \theta_1)
\end{aligned}$$

This map gets iterated N times per wave but the map is the same at each step so that we need only consider one step for issues such as the existence of a nontrivial fixed point or the stability. We suppose that the time between successive firings is τ . Thus, we must have $1 - \theta_1 = \tau$. We can use this to find the fixed points:

$$\begin{aligned}
\theta_{N-1} &= F(\tau) \\
\theta_{N-2} &= \tau + F(\tau) \\
\theta_{N-3} &= 2\tau + F(\tau) \\
&\vdots = \vdots \\
\theta_2 &= (N - 3)\tau + F(\tau) \\
1 - \tau &= F((N - 2)\tau + F(\tau))
\end{aligned}$$

From this we see that there will be such a fixed point for the map if and only if

$$G(\tau, N) = F(F(\tau) + (N - 2)\tau) + \tau = 1.$$

Suppose for the moment that the PRC is small so that $F(x) = x + \epsilon\Delta(x)$ where ϵ is small and positive. Then, upon expanding in ϵ to order 2 we find

$$\begin{aligned}
\tau &= \frac{1}{N} - \frac{\epsilon}{N} [\Delta(\frac{1}{N}) + \Delta(1 - \frac{1}{N})] \\
&+ \frac{\epsilon^2}{N^2} [(\Delta(\frac{1}{N}) + \Delta(1 - \frac{1}{N}))(\Delta'(\frac{1}{N}) - \Delta'(1 - \frac{1}{N})) + N\Delta(1 - \frac{1}{N})\Delta'(1 - \frac{1}{N})]
\end{aligned}$$

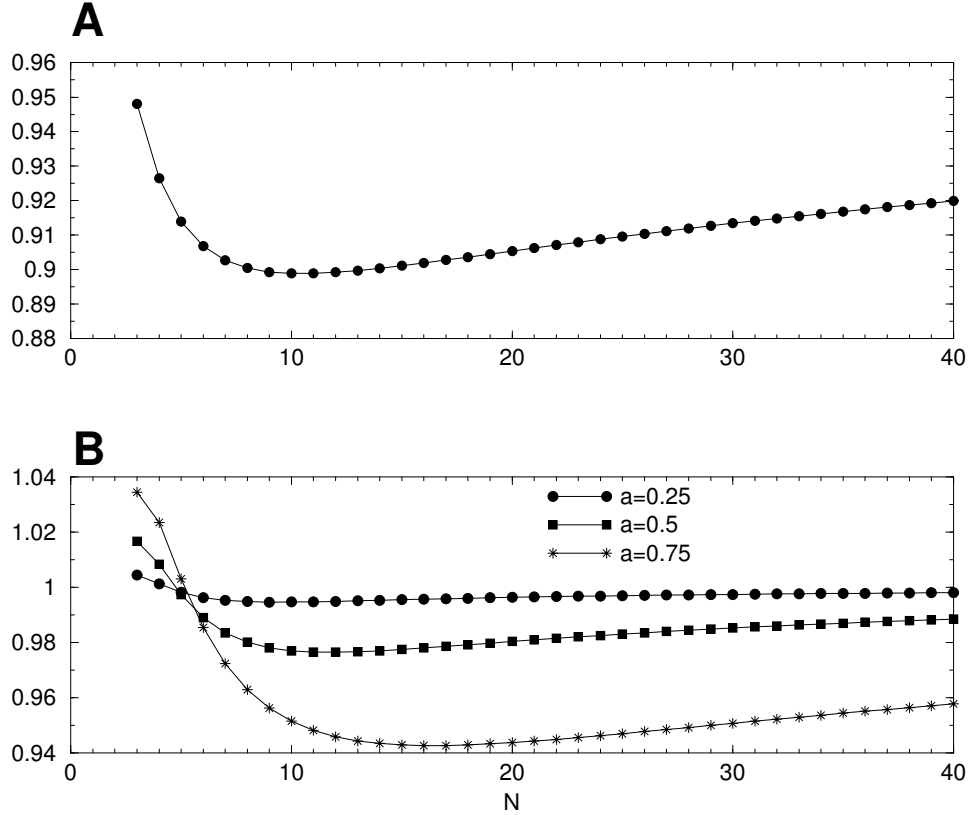


Figure 2.7. The period as a function of the number of oscillators in the ring for (A) the cortical neuron PRC and (B) the sine model at different amplitudes of coupling.

Thus, the timing difference is roughly the length of an uncoupled cycle divided by the number of oscillators. If the PRC is anti-symmetric as is the case for the radial-isochron clock, then the firing interval is $1/N + O(\epsilon^2)$. Since it is a simple matter to numerically solve $G(\tau, N) = 1$ we do so in Figure 2.7 for the model (2.3) which fits Reyes data and for the standard sine model $\Delta(x) = -a \sin(2\pi x)/2\pi$ for a variety of values of a . Rather than plot τ , we instead plot $T = N\tau$ which is the period of a wave. Thus the figures represent a “dispersion” curve for the ring of coupled PRCs. We point out that the neurally motivated PRC (top panel) has a period that is always less than the uncoupled period. This is a consequence of the fact that Δ is nonnegative and the effect of a pulse is to always advance the phase. In contrast, the sine model can both advance and delay the phase and this is shown by the fact that the period is slightly longer for small values of N .

Local stability is determined by linearizing about the fixed point. The resulting matrix has the

form:

$$B_N = \begin{pmatrix} -\alpha_N & \alpha_N & 0 & 0 & \dots & 0 \\ -1 & 0 & 1 & 0 & \dots & 0 \\ \vdots & \vdots & \vdots & \vdots & \vdots & \vdots \\ -1 & 0 & \dots & 0 & 0 & 1 \\ -\alpha_1 & 0 & 0 & 0 & \dots & 0 \end{pmatrix},$$

where $\alpha_N = F'((N-2)\tau + F(\tau))$ and $\alpha_1 = F'(\tau)$. A direct calculation shows that the characteristic polynomial of B_N is just:

$$P(\lambda) = \lambda^N + \alpha_N(\lambda^{N-1} + \dots + \lambda) + \alpha_N\alpha_1.$$

The ‘‘Jury’’ test (Edelstein-Keshet [32]) is a test similar to the Routh-Hurwitz test which allows us to determine when the roots of P lie inside the unit circle. First we note that α_N, α_1 are both positive by the monotonicity of F . Applying this test to $P(\lambda)$ shows that the roots lie in the unit circle if and only if: (i) $\alpha_N < 1$; (ii) $\alpha_1\alpha_N < 1$; and (iii) $1 + \alpha_N\alpha_1 > \alpha_N$. The last condition is trivially satisfied if the first two are satisfied. These conditions are quite intuitively satisfying and very simple to verify. Condition (ii) says that the slope of the PRC must be negative as ϕ approaches 1. This condition is always met in the cortical models when the coupling is excitatory. The second condition is similar to our condition for stability of synchrony for the two neuron network.

We cannot use the map to look at the stability of synchrony since the map is defined under the strict firing order assumption. Small perturbations of the wave maintain this ordering. However, the ordering will not be maintained for the synchronous solution.

Numerical solutions indicate that the waves for $N \leq 10$ are unstable for the model (2.3). For the sine model, (2.2), the stability depends on a ; for a small enough we expect that all waves with $N > 4$ will be stable. This is because when $a \ll 1$ the weakly coupled PRCs become the simple phase models:

$$\frac{d\phi_j}{dt} = \Delta(\phi_j - \phi_{j+1}) + \Delta(\phi_j - \phi_{j-1}).$$

The phase differences between the successive oscillators are $1/N$ and it follows from Ermentrout (1992) that a sufficient condition for stability is that $\Delta'(1/N) < 0$. For the sine model this means that $\cos(2\pi/N) > 0$ so that $N > 4$. However, for larger values of a bigger rings are required to get

a stable pattern.

This result generalizes the result of Canavier *et al* [17] and Dror *et al* [16] to bi-directional coupling and to arbitrary rings of oscillators. However, the results here are local stability results whereas the results from the Canavier group are global.

2.4.2 Chains of PRCs

If we eliminate the coupling between the 1st and the N^{th} oscillator in the ring, we are left with a one-dimensional chain of oscillators. If the coupling is bidirectional and symmetric, then one possible solution is synchrony. It is difficult to create a map for this case due to the fact that there is no reason to believe that ordering will be maintained as was the case for global coupling. Thus, stability of this state is difficult to prove in general. Even the case of a three-oscillator chain is difficult due to the many possible cases and firing orders. If the PRC is small enough then we can appeal to results for a weakly coupled chain (section 2.2.5) which imply that synchrony is stable if $\Delta'(0) < 0$. However, if the PRC is not continuously differentiable at the origin, as seems to be the case for cortical neurons, then even this rather restrictive result cannot be applied. Instead, we must resort to numerical simulations. Figure 2.8 shows the results of a simulation of a chain of twenty nearest neighbor coupled oscillators using the PRC from equation (2.3) with $a = 1.116, b = 0.775, c = 10.2$ which fits the cortical PRC shown in Figure 2.3.

We plot a synchrony index for five different initial conditions in which the phases are either randomly distributed over $[0,1]$ or biased toward a traveling wave solution. The synchrony index, S is defined as

$$\begin{aligned}
 S &= \sqrt{(A^2 + B^2)} \\
 A &= \frac{1}{20} \sum_{j=1}^N \sin 2\pi\theta_j \\
 B &= \frac{1}{20} \sum_{j=1}^N \cos 2\pi\theta_j.
 \end{aligned}$$

If the phases, θ_j are uniformly dispersed around the circle, then $S = 0$ and if they are perfectly synchronized, $S = 1$. Kuramoto ([9], page 71) defines a similar index of synchrony for a globally coupled array of weakly coupled oscillators. For *rings*, the random initial data generally converge

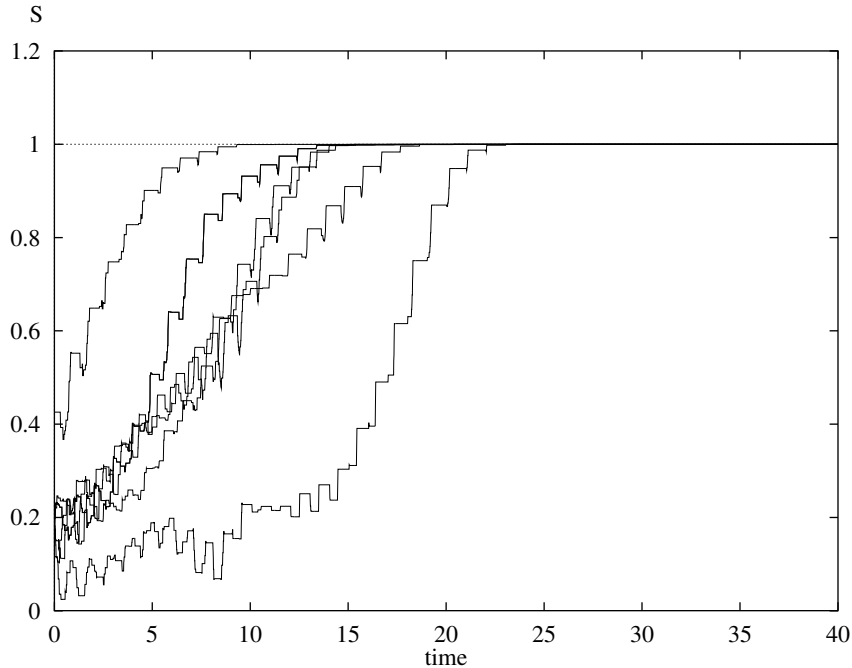


Figure 2.8. Synchronization in a chain of 20 oscillators starting at random phases and using the PRC from Figure 2.3 (the phases of only a few of the oscillators are shown, for clarity). $S = 1$ is the perfectly synchronized state.

to a synchronous solution. However, the biased initial data converge to a traveling wave which has a small synchrony index as the phases are nearly evenly dispersed. We conjecture that if synchrony is stable for pairwise interactions, then it will be stable for chains of nearest neighbor connectivity as long as the coupling is not too strong. This is completely consistent with the results of smooth pulse coupling in section 2.2.6. We remark that the behavior of coupled chains is different from the behavior of chains of phase-difference models such as those analyzed by Ermentrout and Kopell [33]. In generic phase-difference models, synchrony is not even a solution unless one makes adjustments at the ends. Such adjustments are unnecessary with PRCs since there is no effect from an input coming at the exact moment a cell fires ($\Delta(0) = \Delta(1) = 0$).

2.5 Two-dimensional arrays of coupled oscillatory neurons

We consider a network of neural oscillators (“neurons”) that are arranged in an $N \times N$ square array. Each oscillator is bi-directionally coupled to its nearest neighbors through a PRC. In this

section we show that for the sine PRC, persistent *circular waves* can be set up in certain size arrays. That is, the firings proceed systematically in a circular fashion on the array.

2.5.1 A simulation of the wave

We first simulate the wave, to determine the times that the various neurons fire relative to the neuron in the top leftmost corner. That is, the time of firing of the θ_{00} is chosen to be the reference zero time in each period that the wave goes around. The algorithm is as follows. Each neuron is represented as a variable in a two dimensional array. The time this neuron last fired is stored in this variable. Thus, *as the wave passes through the array*, each cell reflects either the firing time (with respect to θ_{00}) from the previous cycle of the wave passing through it, or if the wave has struck it in this cycle, the (current) time it fired. The variables are updated to their most recent value of the firing time, after θ_{00} . We start of the simulation with a certain guess at the firing times of the neuron (detailed below), and see if, as one wave after the other passes through, the system settles into an invariant firing sequence. The wave passing through is implemented by first allowing the θ_{00} neuron to fire, then searching the array for that neuron θ_{ij} that is closest to firing. All the neurons are updated to reflect their phases just before θ_{ij} fires. Finally, the phase of this θ_{ij} is reset to 0, and simultaneously the phases of its (four) nearest neighbors are affected by the PRC. This is repeated until θ_{00} fires again. This leads to a sequence that presumably persists and corresponds to a stable rotating wave.

The initial firing times that we choose for the simulation can be described as follows. The array can be visualized as being roughly composed of concentric *rings* (in analogy with the term *circular wave*). Then, if we consider successive rings, we notice that firings must proceed (counter)clockwise on each ring. To guess at the firing times of the neurons on a ring, we choose the following. Consider the outermost ring of $4(N - 1)$ neurons. Since the θ_{00} neuron fires at the time $t = 0$, and again at (roughly) $t = 1$, the other neurons are setup to fire $\alpha = 1/(4(N - 1))$ apart, going round on the ring. We can then choose, for a clockwise wave, the firing times for neurons on the outer ring to be α for θ_{01} , 2α , for θ_{02} , and so on. The next inner ring is initialized similarly, with θ_{11} set to 0, and the other neurons $\beta = 1/(4(N - 3))$ apart going clockwise around. And so on until all the neurons have been initialized.

2.5.2 The exact system of equations

We now consider the algebraic conditions necessary for a rotating wave with the sinusoidal PRC. There are N^2 unknowns that need to be determined for an $N \times N$ array: the period of the oscillation and the $N^2 - 1$ times relative to the upper left corner. From reflection symmetry only a quarter of these actually need to be found. This leads to $(N/2)^2$ unknowns. We derive the equations for phase-locking for the 4×4 array and then find the roots of this. We compare them to the simulated times.

2.5.3 The 4×4 array

The simplest case to study circular waves in square arrays is $N = 4$.

2.5.3.1 Results of the simulation.

We considered a PRC $\Delta(\phi) = -a \sin(2\pi\phi)/(2\pi)$ with a value of $a = 0.2$. The following table contains the steady state firing times of the different neurons. (Note that the actual simulations were done on the interval $0 < \phi < 2\pi$ for convenience; here we scale the times back to the interval $0 < \phi < 1$.)

0.0/(2 π)	0.337/(2 π)	1.172/(2 π)	1.564/(2 π)
5.864/(2 π)	0.018/(2 π)	1.158/(2 π)	1.901/(2 π)
5.029/(2 π)	4.710/(2 π)	3.146/(2 π)	2.736/(2 π)
4.692/(2 π)	4.300/(2 π)	3.465/(2 π)	3.128/(2 π)

$\tau = 6.256/(2\pi) \approx 0.9956$ is the period of the wave, i.e. the time that θ_{00} fires again. Note that the period is shorter than the uncoupled period of 1 but only by a very small amount.

A pattern of firing times can be discerned by perusing the table of values from the simulation. The following table summarizes the various firing times in terms of four $((N/2)^2)$ unknowns:

0	α	$\tau/4 - \beta$	$\tau/4$
$\tau - \beta$	γ	$\tau/4 + \gamma$	$\tau/4 + \alpha$
$3\tau/4 + \alpha$	$3\tau/4 + \gamma$	$\tau/2 + \gamma$	$\tau/2 - \beta$
$3\tau/4$	$3\tau/4 - \beta$	$\tau/2 + \alpha$	$\tau/2$

The structure of this table depends crucially on the fact that the PRC we use is odd-symmetric.

Like the work of Poullet and Ermentrout [14], we exploit this symmetry to reduce the number of equations. If $\Delta(-\phi) \neq -\Delta(\phi)$ then there can generally be no such simplification. However, the simulation scheme works for any PRC, Δ such that $|\Delta'(\phi)| < 1$ (i.e $F(\phi)$ is invertible.)

From this table, we can derive a set of four equations. Consider the θ_{00} neuron. When it fires at time $t = 0$, its phase is 0 at that instant. The phase then continues to increase, until one of its neighbors fires. Based on the simulations we expect that going around in a wave the neuron θ_{01} (rather than θ_{10}) will fire first. At this point the phase of θ_{00} changes from α to $F(\alpha)$. Once more, the phase of θ_{00} continues to grow independently until a time $\tau - \beta$, when θ_{10} fires, and disturbs its phase to $F(F(\alpha) + (\tau - \beta - \alpha))$. With no other firings to affect it, it can continue to rise until 1, when it fires and must be reset to 0. Thus the following equation must hold:

$$F(F(\alpha) + (\tau - \beta - \alpha)) + \beta = 1$$

Similarly, we can write three other equations by choosing three other oscillators to get a complete system:

$$\begin{aligned} F(F(\alpha) + (\tau - \beta - \alpha)) + \beta &= 1 \\ F(F(F(\beta) + \gamma) + .75\tau + \alpha - \gamma) + \beta &= 1 \\ F(F(F(.25\tau - \beta - \alpha) + .75\tau + \beta) + \gamma) + \alpha - \gamma &= 1 \\ F(F(F(F(\alpha - \gamma) + .25\tau + \gamma - \alpha) + .5\tau) + .25\tau - \beta - \gamma) + \gamma + \beta &= 1 \end{aligned} \tag{2.31}$$

(In Poullet and Ermentrout, $\tau = 1$, $\alpha = \beta$, and $\gamma = 0$ so that there was a single algebraic equation.)

The system of equations (2.31) above can be solved for α , β , γ and τ , using Newton's method. Furthermore, we can use a continuation package such as XPPAUT [34] to study how the roots evolve as the magnitude a increases.

2.5.4 The 6×6 array

The next case to study is $N = 6$. Again, we carry out a simulation, and compare the results to a computation from a system of exact equations. Proceeding as outlined above we obtain the following array of firing times:

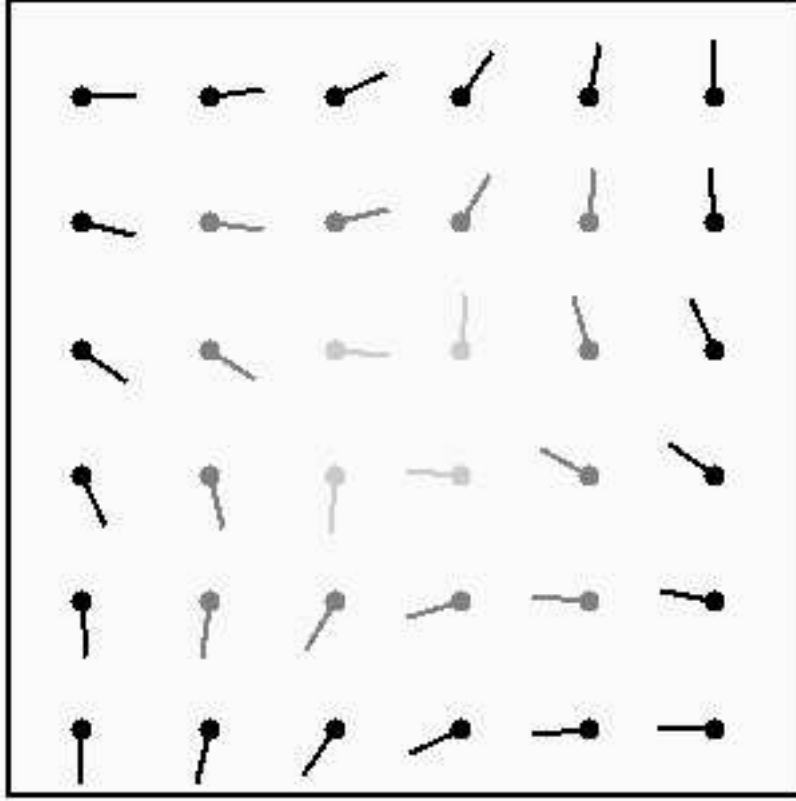


Figure 2.9. The relative phases for the 6×6 array in the sine model. Lines denote the angle relative to the upper left corner. Outer, middle, and inner “rings” are different grey scales.

$0.0/(2\pi)$	$0.125/(2\pi)$	$0.447/(2\pi)$	$0.960/(2\pi)$	$1.345/(2\pi)$	$1.563/(2\pi)$
$6.036/(2\pi)$	$6.162/(2\pi)$	$0.287/(2\pi)$	$1.046/(2\pi)$	$1.471/(2\pi)$	$1.688/(2\pi)$
$5.651/(2\pi)$	$5.737/(2\pi)$	$6.188/(2\pi)$	$1.497/(2\pi)$	$1.851/(2\pi)$	$2.011/(2\pi)$
$5.138/(2\pi)$	$4.978/(2\pi)$	$4.624/(2\pi)$	$3.061/(2\pi)$	$2.609/(2\pi)$	$2.523/(2\pi)$
$4.816/(2\pi)$	$4.598/(2\pi)$	$4.173/(2\pi)$	$3.414/(2\pi)$	$3.034/(2\pi)$	$2.909/(2\pi)$
$4.690/(2\pi)$	$4.473/(2\pi)$	$4.087/(2\pi)$	$3.575/(2\pi)$	$3.252/(2\pi)$	$3.127/(2\pi)$

As the above table shows, this is a wave circling on a 6-dimensional array. The wave is stable and (locally) attracting. Figure 2.9 shows a plot of these relative phases. The outermost ring of 20 oscillators looks like a traveling wave that covers one full cycle as the perimeter is traversed. Similarly the middle ring of 12 oscillators is also a traveling wave. The inner ring of four oscillators consists of cells one quarter of a cycle apart. Thus, these apparently stable patterns look like nested rings of coupled maps, nearly synchronized along the diagonals. We point out that the patterns

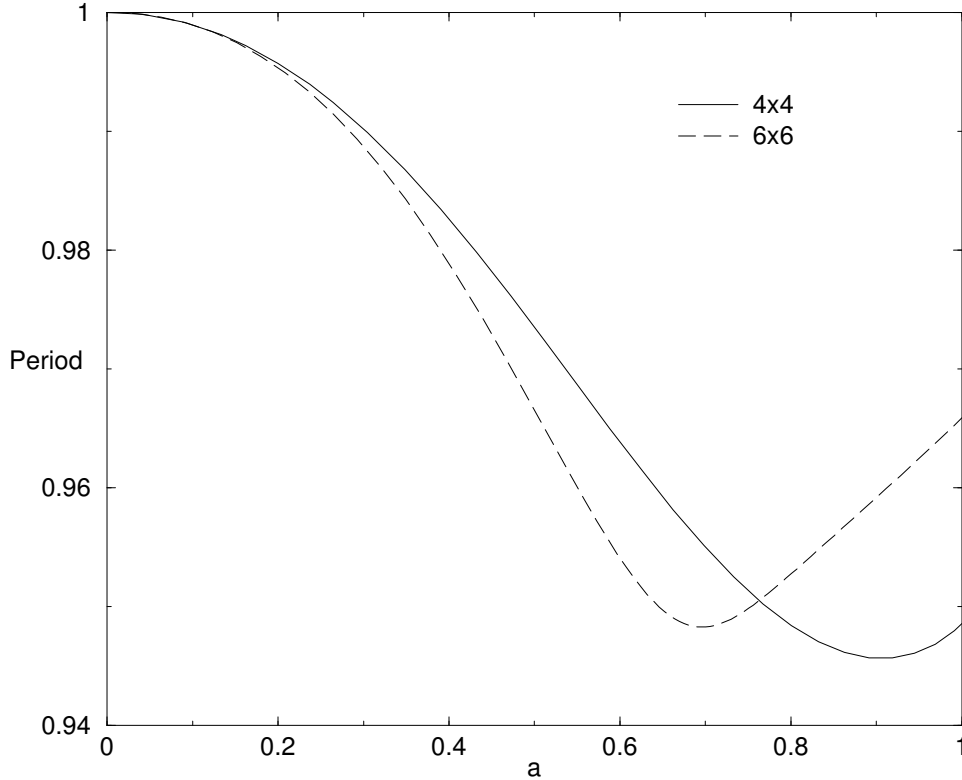


Figure 2.10. The period as a function of the strength of coupling in a square array for the sine model.

here are the direct analogues of those found by Paullet and Ermentrout [14] in arrays of weakly coupled oscillators. The pattern of phases in two dimensions is like a pinwheel such as seen in the analysis of the Ginzberg-Landau equation (Greenberg [35], Hagan [36]; Paullet [14]):

$$z_t = z(1 + i\omega - z\bar{z}) + \nabla^2 z.$$

In Figure 2.10 we show the period of the rotating wave as a function of the strength of the coupling, a for the 4- and 6-dimensional square arrays. We note that this is not monotonic.

2.5.5 Larger two-dimensional arrays

We have extended our simulations to arbitrary sized arrays. Simulations show similar waves. The analyses based on writing an analytical set of equations grows increasing difficult to implement, however. We note that the small arrays of odd-dimension (e.g.5x5) seem to have only the

synchronous solution (at least for the initial conditions implemented in above). However, preliminary results on large arrays show that the dependence on the evenness of the dimension is an artifact of small dimensionality. We expect these circular waves exist in all even N -dimensional ($N \geq 4$) arrays and sufficiently large odd-dimensional arrays. A general existence is still an open question as is the rigorous determination of stability.

2.6 Discussion

We have generally examined a number of networks of coupled phase-response curves. Under certain assumptions (i.e. a fixed firing sequence) it is possible to reduce these to discrete maps. However, the existence of such a map depends on maintaining this fixed firing sequence. Thus, the issue of heterogeneity in uncoupled frequency becomes an important one for the all-to-all networks. For then, near synchrony, it is possible for the order of firing to be changed. On the other hand, with heterogeneity, we don't expect exactly synchronous solutions. Instead, we expect that the oscillators will fire in order of their uncoupled frequency. Small perturbations will not destroy this order so that our techniques are probably applicable. Heterogeneity in coupling is significantly more difficult. The development of a theory for general all-to-all systems remains to be found. For the ring models where there is a fixed firing sequence bounded away from synchrony, small differences in the oscillators will not affect the map as the sequence will be maintained. The maps for linear chains and the two-dimensional systems remain to be described. We note that it is probably possible (albeit tedious) to prove the synchrony of the rotating waves in the two-dimensional lattices. The idea is to exploit the fact that there is a fixed firing sequence. This allows us to define a local linearization of the map and from this determine whether synchrony is stable. All numerical simulations seem to point to stability at least for the simple sinusoidal PRC. Ideally, a general theorem analogous to that in Ermentrout [31] could be proven.

Canavier *et al* and Dror *et al* have concentrated their efforts on computing and analyzing the PRCs for coupled "burst-like" neurons. This is in some ways a much more difficult problem than that which we have derived here. In bursting neurons the effect of one oscillator on the other can be prolonged. Furthermore, the length of time of the effect can depend on the inputs to that oscillator. Effects of such a large perturbation can affect the next cycle as well. Thus, the maps

that one derives from coupled bursters are much more challenging to analyze. In the present work, the interactions are presumed to be very short-lasting compared to the period of the oscillators. For example, cortical excitatory synapses typically last only 2-5 milliseconds while the period of oscillations varies from 25 to 100 milliseconds. This allows us to ignore the possibility of inputs “bleeding” over into the next cycle.

Appendix

Proof of theorem: We define the following N diagonal matrices, d_k , $k = 1, \dots, (N - 1)$, as follows: d_0 is the $(N - 1)$ dimensional diagonal matrix with all its (non-zero) elements α_0 's, d_1 with α_1 's, and the other d_i 's having both α_0 's and α_1 's. $d_2 = \mathcal{D}(\alpha_1, \alpha_1, \dots, \alpha_1, \alpha_0)$, $d_3 = \mathcal{D}(\alpha_1, \alpha_1, \dots, \alpha_0, \alpha_0)$, and so on, with d_i having as its last $(i - 1)$ elements α_0 (and the others α_1), where \mathcal{D} stands for the $(N - 1) \times (N - 1)$ diagonal matrix. Also, let

$$E = \begin{bmatrix} -1 & 1 & 0 & 0 & \cdots \\ -1 & 0 & 1 & 0 & \cdots \\ -1 & 0 & 0 & 1 & \\ \vdots & & & & \ddots \\ -1 & 0 & & & 0 \end{bmatrix}$$

If $B = E D_{n-1} \dots E D_1 E D_0$, then the eigenvalues of B are of the form $\alpha_0^p \alpha_1^{N-p}$ with $1 \leq p \leq N - 1$.

Proof. Let us consider the product B above. We claim that the following matrix S is a similarity transformation that diagonalizes B with the required eigenvalues on the diagonal. S is the $(N - 1) \times (N - 1)$ matrix with all elements on the diagonal, and above it, unity, and zero otherwise. That is,

$$S = \begin{bmatrix} 1 & & \cdots & & 1 \\ 0 & 1 & & & \\ \vdots & \ddots & \ddots & & \vdots \\ \vdots & & & \ddots & 1 \\ 0 & \cdots & \cdots & 0 & 1 \end{bmatrix}$$

with an inverse

$$S^{-1} = \begin{bmatrix} 1 & -1 & 0 & \cdots & 0 \\ 0 & 1 & \ddots & \ddots & \vdots \\ \vdots & \ddots & \ddots & \ddots & 0 \\ \vdots & & \ddots & 1 & -1 \\ 0 & \cdots & \cdots & 0 & 1 \end{bmatrix}$$

Thus we need to show that $S^{-1}BS$ is a diagonal matrix. We proceed as follows: It is a simple matter to evaluate the product $E D_1 E D_0 S$ which is of the following general form:

$$E D_1 E D_0 S = \begin{bmatrix} 0 & -\alpha_0\alpha_1 & 0 & \cdots & 0 \\ & & \ddots & \ddots & \vdots \\ \vdots & \vdots & & \ddots & 0 \\ 0 & -\alpha_0\alpha_1 & \cdots & & -\alpha_0\alpha_1 \\ \alpha_0\alpha_1 & 0 & \cdots & & 0 \end{bmatrix}$$

Next, we make the following claim: every matrix product up to the k^{th} factor $E D_k \dots E D_1 E D_0 S$ is of the general form:

$$P_k = E D_k \dots E D_1 E D_0 S = \begin{bmatrix} 0 & & \cdots & & 0 & -\alpha_0\alpha_1^k & 0 & \cdots & 0 \\ \vdots & & & & \vdots & & \ddots & \ddots & \vdots \\ & & & & & \vdots & & \ddots & 0 \\ 0 & & \cdots & & 0 & -\alpha_0\alpha_1^k & \cdots & & -\alpha_0\alpha_1^k \\ \alpha_0^k\alpha_1 & \alpha_0^{k-1}\alpha_1^2 & \cdots & \alpha_0^2\alpha_1^{k-1} & \alpha_0\alpha_1^k & 0 & \cdots & \cdots & 0 \\ 0 & \alpha_0^{k-1}\alpha_1^2 & & \vdots & \vdots & \vdots & & & \vdots \\ & \ddots & & & & & & & \\ \vdots & & \ddots & \alpha_0^2\alpha_1^{k-1} & \vdots & \vdots & & & \vdots \\ 0 & \cdots & & 0 & \alpha_0\alpha_1^k & 0 & \cdots & \cdots & 0 \end{bmatrix}$$

We remark the following characteristics of this matrix: The $(N-1)$ dimensional matrix above is made up of two submatrices of dimensions k and l with $l = (N - 1) - k$. Let us call the 'lower-triangular' submatrix occupying the upper right $l \times l$ corner of P_k , the \mathcal{L} (sub)matrix, and the

'upper-triangular' submatrix occupying the bottom left $k \times k$ corner of P_k , the \mathcal{K} (sub)matrix. (We note all other elements of P_k are identically zero). All elements of \mathcal{L} are identical, and equal to $-\alpha_0\alpha_1^k$. All elements in the i^{th} column of \mathcal{K} are identical, and equal to $\alpha_0^{k+1-i}\alpha_1^i$. We next consider the product of P_k with the next (premultiplying) factor $P_{k+1} = E D_{k+1} P_k$ in $S^{-1}BS$. If our original claim is to be true, the matrix P_{k+1} must be of the same general form that we described for P_k . Except that for P_{k+1} , its \mathcal{K} matrix is of dimension $(k+1)$ (and \mathcal{L} is one dimension smaller). We verify this is indeed the case. We note that D_{k+1} is a diagonal matrix with the last $k+1$ elements α_0 (the first $N-1-k$ elements α_1). Hence we observe that the product $D_{k+1}P_k$ is simply obtained by multiplying the elements of \mathcal{L} in P_k by α_1 , and those of \mathcal{K} by α_0 ! We also notice that under (pre)multiplication by E , every j^{th} column $(r_1, r_2, \dots, r_{N-2}, r_{N-1})^T$ in the multiplicand matrix is simply permuted to $(-r_1 + r_2, -r_1 + r_3, \dots, -r_1 + r_{N-2}, -r_1)^T$. The product $E D_{k+1} P_k$ is then of the desired form. Proceeding to write $BS \equiv P_{N-1}$ we obtain the upper triangular matrix:

$$BS = \begin{bmatrix} \alpha_0^{N-1}\alpha_1 & \alpha_0^{N-2}\alpha_1^2 & \cdots & \alpha_0^2\alpha_1^{N-2} & \alpha_0\alpha_1^{N-1} \\ 0 & \alpha_0^{N-2}\alpha_1^2 & & \vdots & \vdots \\ \vdots & \ddots & & & \\ & & \ddots & \alpha_0^2\alpha_1^{N-2} & \vdots \\ 0 & \cdots & 0 & \alpha_0\alpha_1^{N-1} \end{bmatrix}$$

It can easily be verified that premultiplying by S^{-1} (given above) then sets all the elements besides those on the diagonal to zero. Hence the eigenvalues of B follow as proposed.

Chapter 3

On the Increase in the Human Beta Rhythm Activity with the Sedative Diapam

3.1 Introduction

Oscillatory activity of the human cerebral cortex, monitored by electroencephalographic (EEG) and magnetoencephalographic (MEG) recordings, comprises several prominent frequency bands. EEG recordings from the sensorimotor cortex show oscillations primarily around 10 and 20 Hz. Both bands show a task dependent modulation. In clinical EEG records, rhythmic beta oscillations are seen in frontal scalp areas in subjects who have taken benzodiazepine-type drugs. Less prominent beta oscillations are also found in extrastriate, temporal and parietal areas. 20-Hz activity in a healthy human subject occurs in the sensorimotor cortical areas (and is modulated) during various motor and cognitive tasks. Moreover, a part of the (approximately) 20-Hz motor-cortex oscillations are coherent with simultaneously recorded surface electromyogram during isometric contraction; this coherent activity has been suggested to be related to recalibration after movements. Thus there seems to be good evidence to suggest that beta oscillations play an important role in processing of sensorimotor information.

Recent experiments of Jensen *et al* [6] have been directed towards investigating whether benzodiazepine might modify the motor-cortex 20-Hz oscillations. They recorded MEG signals from healthy adults before and after oral application of benzodiazepine. Clinical properties of benzodiazepine include sedation, anxiolysis, amnesia, anticonvulsion, and muscle relaxation. (It is important to note that in the experiment, subjects are asked to *relax* under the MEG helmet during the recording, both before (control) and after taking the drug.) They were also able to locate the sources of the beta-range oscillations and characterize its frequency spectrum. They find that following administration of the drug, power in the beta band increases dramatically, and the frequency shifts a few Hz lower. The primary effect of benzodiazepines is to increase the conductance of $GABA_A$ mediated currents. *It is counterintuitive how an increase in inhibition mediated by the*

higher inhibitory conductance should increase the power of a rhythm (and why that increase should be in the beta band).

The human beta oscillations appear to resemble gamma band oscillations (30–90 Hz) observed in various animal preparations. Gamma oscillations have been modeled *in vitro* by Whittington and collaborators in the hippocampus. In the *in vitro* persistent gamma oscillations the pyramidal cells fire very sparsely, while the interneurons fire at gamma frequencies. The computational network model proposed here suggests that the human beta oscillations are an analogue of the gamma oscillations studied in rats.

The frequency of the beta oscillations decreases when the inhibitory cells receive increased inhibition modeling the effect of benzodiazepines. A more subtle effect comes from the accompanying increase in period: excitatory cells that were partially suppressed by the inhibition at a given period can spike on a larger fraction of each cycle, so the proportion of pyramidal cells firing on any given cycle increases. We also show that an increase in inhibition to the pyramidal cells causes them to fire at a smaller fraction of each cycle, making firing more coherent. We conclude that it is the effect of benzodiazepines *on inhibitory cells* that is the major cause of the increase in beta power with administration of benzodiazepines.

3.2 Modeling

The aim of the modeling is to show that an increase in benzodiazepine, modeled as an increase in GABA(A)-mediated (inhibitory) conductance, can increase the power in the beta frequency band of the MEG. We simulate a network of a 64 excitatory and 16 inhibitory cells globally coupled together to represent the cortical population. (The detailed equations are in the Appendix at the end of the chapter.) We separate the simulations into ones in which the inhibition to inhibitory (i-cells) was increased, and ones in which the inhibition to excitatory (e) cells was increased. We show below that the increase in the former is consistent with all the experimental data, while the latter is not.

The model we propose here accounts for the apparently paradoxical result (namely that excitatory activity *increases* upon application of an “*inhibitory*” drug) by assigning a regulatory role to inhibitory cells in the network. Thus the i-cells not only produce spontaneous oscilla-

tions in the beta bands synchronized via recurrent connections, but also keep the activity in the e-cells low under normal conditions (i.e. in absence of the drug). As benzodiazepine is applied, the increased $g_{i \rightarrow i}$ lowers this frequency (through the increased inhibition), and the weaker inhibition to the e-cells ($g_{i \rightarrow e}$) also allows many more of them to be released from suppression. This mode of activity where clearly the i-cells gate activity in the e-cells is thus a form of the ING rhythm (although at beta frequency, see also Chapter 4, section 4.1.3, and Discussion below); a relatively stronger $e \rightarrow i$ connection is implicated in the creation of the PING rhythm.

We are also faced with two other possibilities that can be attributed to state of the subject during experiment: relaxed, or actively processing. Excitatory conductance to the i-cells is thought to be weaker in the states of the network that correspond to resting, than during active processing, when there are likely to be effects of arousing neuromodulators, which have the effect of decreasing habituation of excitatory synapses. Thus, in a relaxed state, with some ongoing activity at beta frequencies, the excitatory synapses are likely to be at a state of lower maximal conductance than during active processing. We will examine the simulations in parameter regimes suited to these two cases below.

3.3 The “Rest State Network”: Weak g_{ei}

The baseline parameters of the network are chosen so that the i-cells are active in the absence of excitatory input, and the mutual inhibition among those cells is strong enough to create a synchronous rhythm (Traub *et al* [37], White *et al* [38], Wang and Buzsaki [39]). Such a mechanism is known to produce a gamma rhythm in vitro (Traub *et al* [4], Whittington *et al* [5]). It is also known that, for this mutually inhibitory rhythm, the period is proportional to the decay time of the inhibition. (Chow *et al* [40]). This motivates modeling a beta-frequency mutually inhibitory frequency by taking a relatively large decay time constant of the GABA(A) mediated inhibition, which we take here to be $\tau_i=20$ ms.

The parameters for the e-cells were chosen so that, in the absence of the benzodiazepine input, few of the cells fire, and those that do fire at frequencies lower than the beta range. This is done by having a relatively low range of drives to the e-cells and having a significantly large slow outward current, both compatible with the resting state of the subjects.

Figure 3.1 (top panel) shows the computed power spectrum for three values of g_{ii} , the maximal inhibitory conductance to an i-cell. As the maximal conductance is increased, the power in the beta frequency range increases, the maximal power increases, and the spectral plot widens. Also, the frequency decreases.

Fig 3.1 (bottom panel) shows the power spectra for increasing values of g_{ie} , the maximal inhibitory conductance for the E-cells, while holding g_{ii} fixed at one of the values in the plot above. Note that, as g_{ie} increases, the power decreases, the frequency remains constant, and the spectral plot becomes thinner.

The mechanism behind the above results can be understood from looking at the raster plots in figures 3.2 and 3.3. The firing of the i-cells are plotted at the bottom (negative indices), and that of the e-cells at the top (positive indices), ordered according to the amount of external drive. The figure E-cells have a range of excitability (i.e., range of imposed drives), the only cells that fire are the ones that have enough drive to spike before the next pulse of inhibition .

Figure 3.2 shows that, as g_{ii} is increased, the period of the underlying inhibitory rhythm grows. This allows more E-cells to fire in a given period. The e-cells that fire for the larger value of g_{ii} are more spread out within a given cycle as can be seen in the histogram, where each of the cycle periods has been normalized to 1 for comparison. We show below in section 3.3.1 that this is true because the e-cells fire when the inhibition has decayed sufficiently (depending on the drive to those cells); with the period increasing, but the inhibition to the e-cells not changing as g_{ii} is increased, there is a longer interval for e-cells to fire before the next bout of inhibition.

Increasing g_{ie} has a different effect, as shown in Figure 3.3. As this conductance is increased, the e-cells get more inhibition, and fewer of the cells fire. However, (as shown in the histogram) the e-cells that do fire are more coherent. The reason is the converse of the decrease in coherence for increasing g_{ii} : as g_{ie} increases, the inhibition to the e-cells suppresses the firing of the latter for a longer proportion of the period, and hence those that fire must do so more coherently.

3.3.1 Analysis of the Role of Inhibition in Determining the Relative Phases of Firing of the E-cells

We can simplify the physics of this problem to examine the role of varying inhibition to the e-cells in determining the number of e-cells that can fire in a given cycle and the range of phases relative

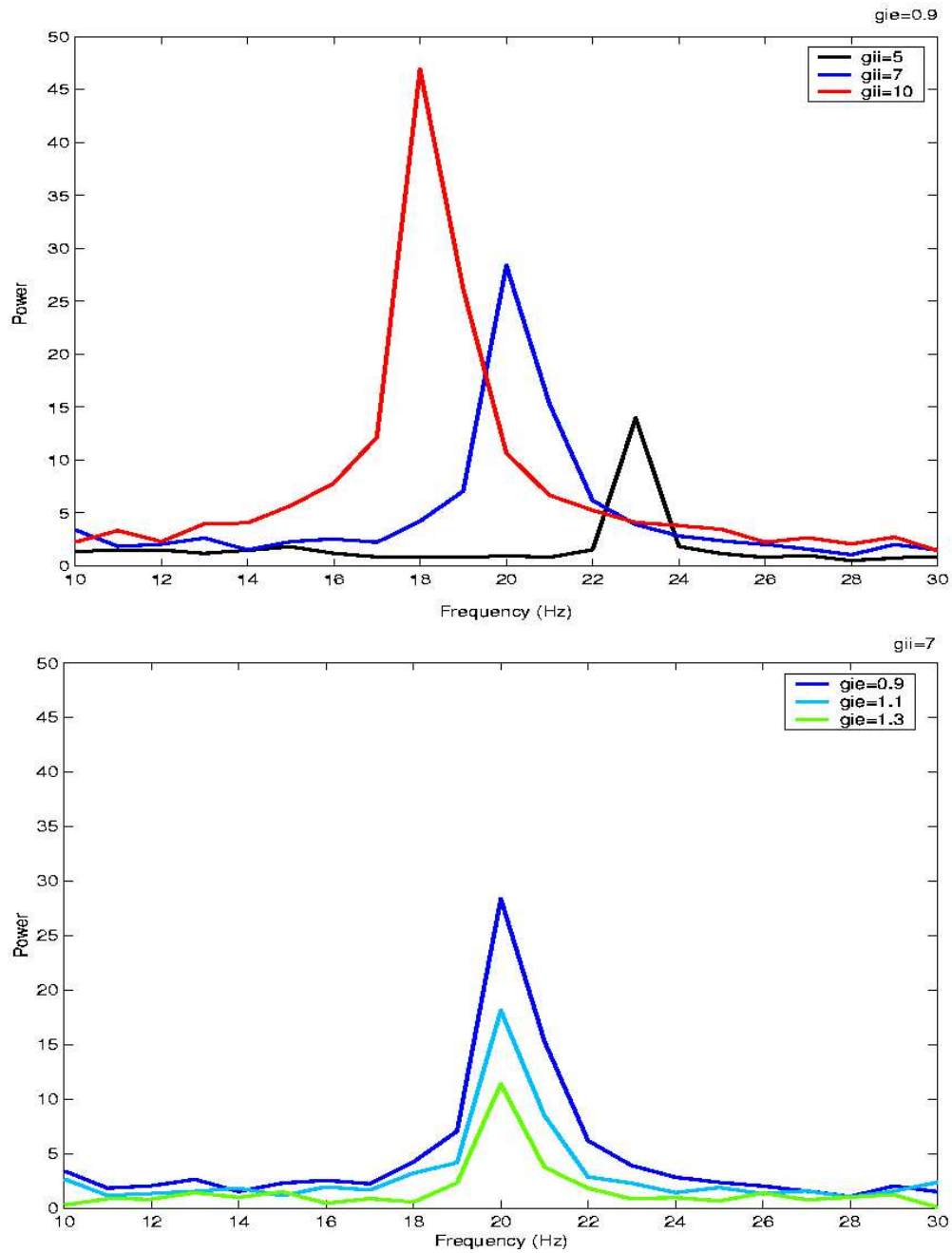


Figure 3.1. Power spectra computed for various values of the inhibition in the rest-state network. In the top panel, g_{ie} is held fixed at 0.9 and g_{ii} is varied. The bottom panel shows the result of holding g_{ii} at one of the values (taken from above) and increasing g_{ie} .

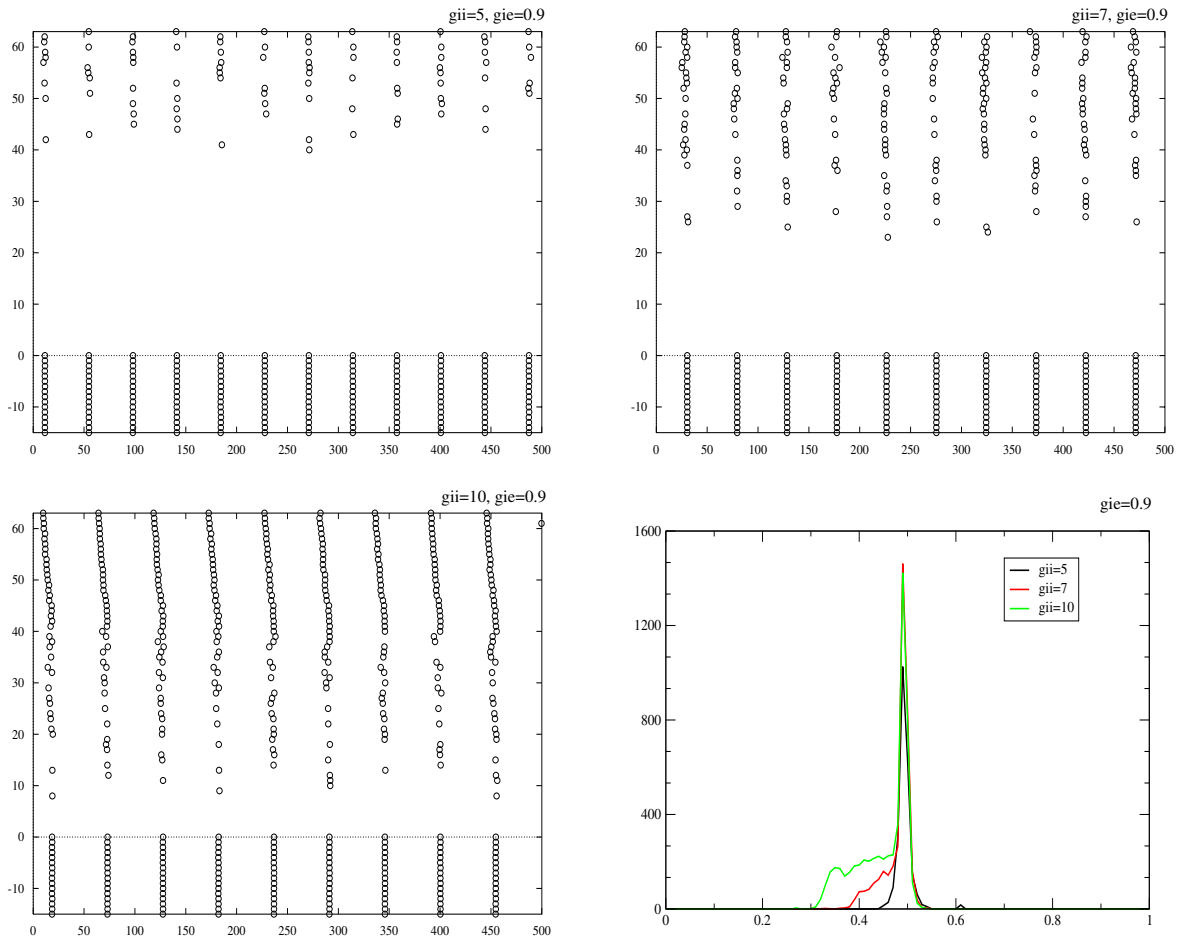


Figure 3.2. Rasters and histograms of activity in the rest-state network, for fixed g_{ie} , and varying g_{ii} . Time (in milliseconds) is on the x-axis, and the cells are plotted by index on the y-axis. The fastest e-cells lie closest to the top. Parameter values for the run appear on the top-right of each panel. The bottom right panel shows a histogram of the spike times over a run of 100 periods normalized with respect to the period of the i-cells for the three rasters. Notice that the parameter values between this figure and the next, Figure 3.3, are the same as used in Figure 3.1, for comparison.

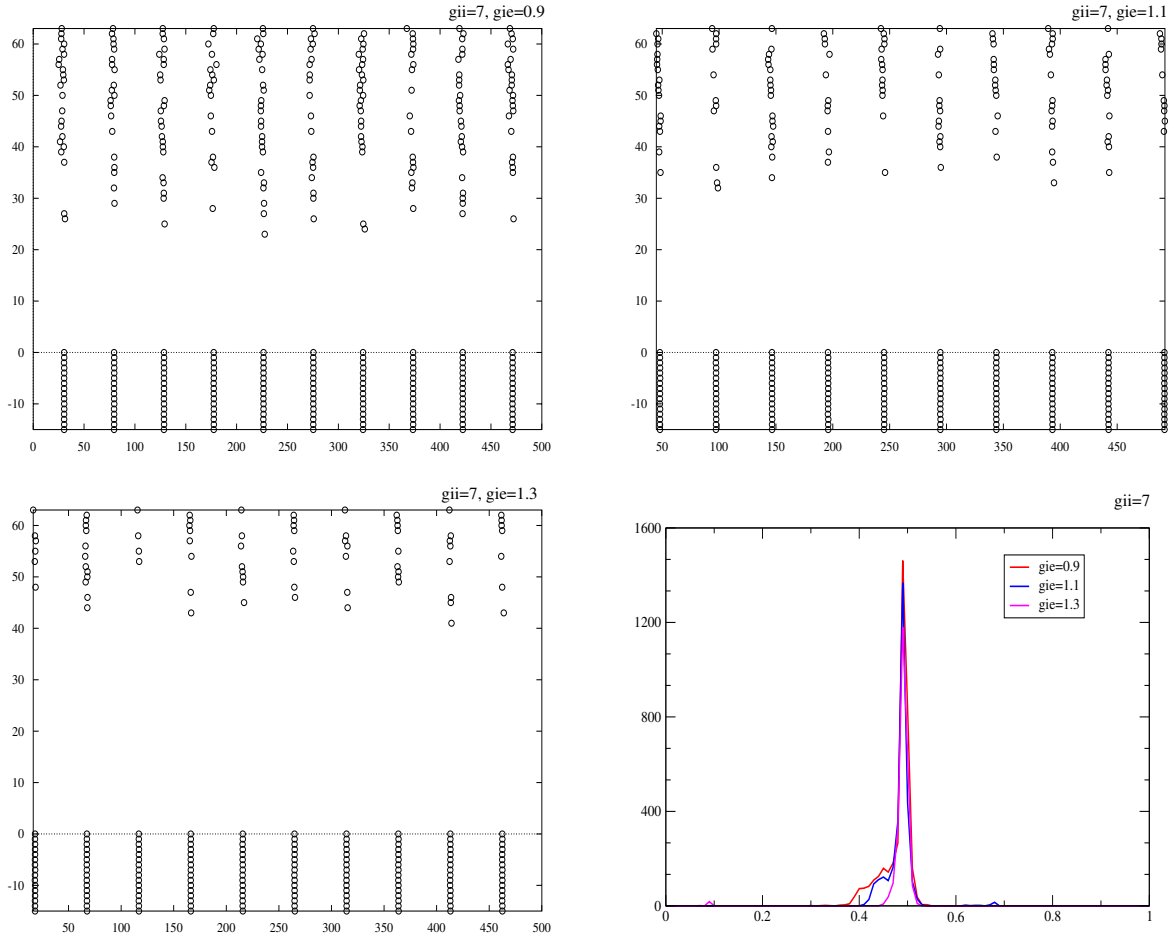


Figure 3.3. Rasters and histograms for rest-state activity, at fixed g_{ii} , and varying g_{ie} . Note that, for reference, the red curve (and the corresponding raster panel) is the same as in Figure 3.2 above.

to the cycle period over which they fire. Figure 3.4 shows the behavior of the synaptic conductance from an i-cell taken from the full simulation and an e-cell's own afterhyperpolarization¹ (AHP), the two variables that determine when (or if) that e-cell can fire next. Notice that the inhibition from i-cells arrives at an e-cell at the period of the rhythm (since the i-cells fire synchronously). Following an action potential in an e-cell, an outward hyperpolarization current turns on. This tends to further inhibit the cell. Since the time constant of AHP conductance is large compared to the period of the rhythm (around 50 ms), there is significant adaptation in that current from cycle to cycle. The figure strongly suggests modeling these quantities as exponentially decaying variables. Thus we take the inhibition from i-cells as a quantity (proportional to) $g_{ie} s$, and the AHP current

as $g_{ahp} z$, where $\dot{s} = -s/\tau_i$ and $\dot{z} = -z/\tau_a$ are assumed to decay with appropriately chosen decay constants. (We will not be too concerned for the particular numerical values we shall pick for these numbers below, only their approximate relative strengths matter.) The e-cell is assumed to fire when the total inhibition has decayed to a value I , which is related to the current drive to the cell; the larger the I , the sooner the e-cell can fire on a given cycle.

Figure 3.5 shows one such e-cell phase-locked to an i-period. The synaptic variable s is assumed to decay with a time constant $\tau_i=20$ ms, and the AHP variable, z , with $\tau_a=50$ ms. $g_{ie}=3$, and $g_{ahp} = 0.5$. We take P , the period of the i-rhythm to lie between 40 ms (25 Hz), and 50 ms (20 Hz) for the different values of g_{ii} . Thus, the change in the period of the oscillation corresponds to a change in g_{ii} ; for a given value of P , setting the sum $(g_{ie} s + g_{ahp} z)$ equal to I for a particular e-cell determines the time, \bar{t} , when it fires in that cycle. Since we assume fast inhibitory synapses, s is reset to 1 at the beginning of every cycle. The value of z , however, depends strongly on its value during the previous cycle. Let the value of z be \bar{z} at the beginning of some cycle. When the e-cell fires at a time \bar{t} in the cycle, z is reset at to $z(\bar{t}) + 1$ (note that the we can assume 1 without loss of generality, since in the following analysis any other value can be absorbed by rescaling g_{ahp}). As the system approaches its steady state, the value of \bar{z} can be determined as the fixed point of the map that generates \bar{z} on successive cycles. Thus we find that

$$\bar{z} = \frac{1}{\exp(P - \bar{t})/\tau_a - \exp(-\bar{t}/\tau_a)} \quad (3.1)$$

For simplicity, we consider here only those e-cells that have a periodicity of P , and each cell is assumed to fire at most once in the cycle. These two conditions will determine the minimum and maximum values of the allowable drives to these cells. The phase $\phi = \bar{t}/P$ of an e-spike is a function of the drive I . If an e-cell is to spike at least once every period, the drive to it must be above a critical value I_l (Figure 3.5, left panel). That is, at I_l , $\bar{t} = P$. Thus I_l is determined as

$$I_l = g_{ie} \exp(-P/\tau_i) + g_{ahp}/(\exp(P/\tau_a) - 1) \quad (3.2)$$

In order to prevent firing more than once every cycle, the drive must be kept below a value, I_h (Figure 3.5, right panel) for all cells. In order, to obtain the critical value I_h , we note that the

¹The variable z in the figure is identical to the gating variable of the AHP current, w (see Appendix).

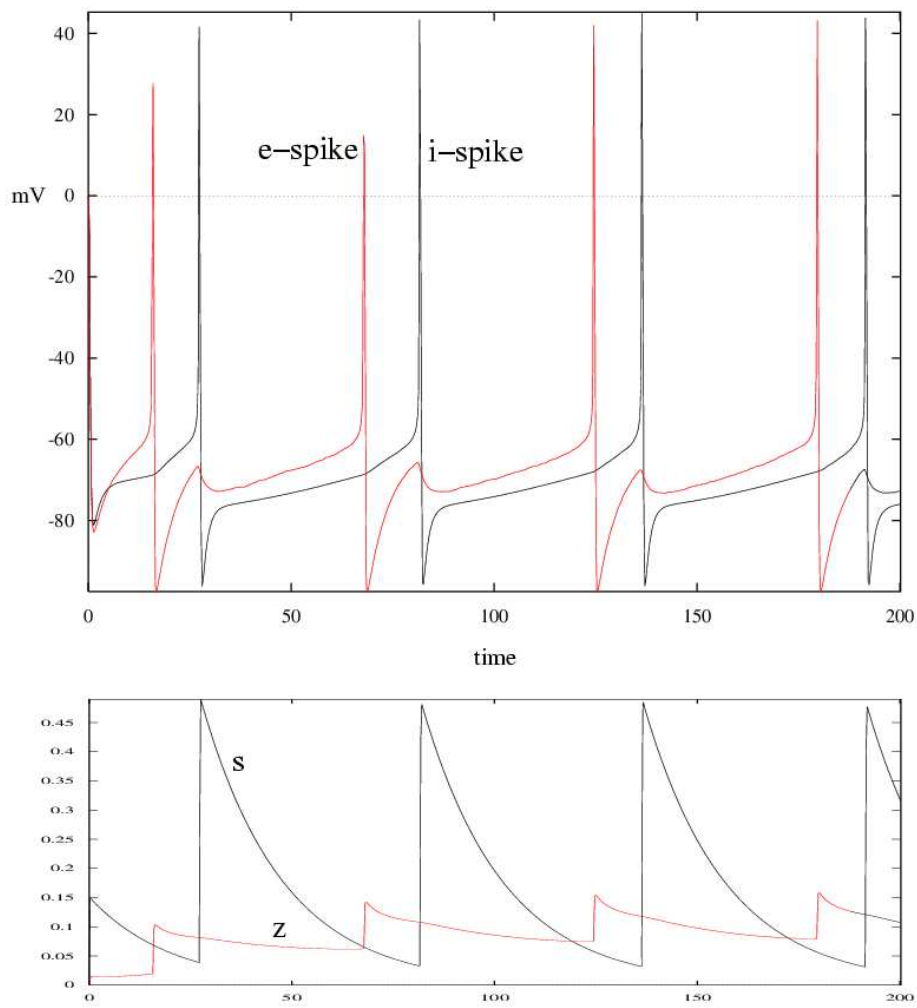


Figure 3.4. Voltage traces of an i- and e-cell taken from the full simulation (top panel). The corresponding synaptic variable for i-cell, s , and AHP gating variable, z , for that e-cell are shown below (bottom panel). The inhibitory synapse peaks when the i-cell fires, and the AHP current turns on when the e-cell fires. Note that the decay time of the AHP current is larger than the time constant for decay of synaptic current. Notice also that z adapts on successive cycles..

e-cell spikes at \bar{t} , but is just prevented from firing again by a spike of inhibition arriving at P. This leads to pair of equations that contain \bar{t} implicitly:

$$I_h = g_{ie} \exp(-\bar{t}/\tau_i) + g_{ahp}/(\exp(P/\tau_a) - 1) \quad (3.3)$$

$$I_h = g_{ie} \exp(-P/\tau_i) + g_{ahp} \exp(\bar{t}/\tau_a)/(\exp(P/\tau_a) - 1) \quad (3.4)$$

For cells with intermediate values of drive, $I_l < I < I_h$, the time \bar{t} of the e-spike can be determined as the root of

$$I = g_{ie} \exp(-\bar{t}/\tau_i) + g_{ahp}/(\exp(P/\tau_a) - 1) \quad (3.5)$$

We numerically compute the values of phases ϕ (relative to the normalized period) of spiking for e-cells driven with different I . Figure 3.6 plots the phase of the e-spike relative to the i-cycle for various values of P (i.e. g_{ii}), for two values of g_{ie} . The phase is seen to retract into the cycle for higher value of I . For larger values of g_{ie} the number of cells firing in the cycle is also decreased. As the period is increased (i.e. increasing g_{ii}), more cells are seen to emerge from suppression. This figure thus reproduces qualitatively the results in the discussion above (section 3.3).

If we assume drive I is distributed linearly in the e-cells, we can estimate the *number* of e-cells spiking per cycle at a given P to be proportional to $I_h(P = 50) - I_l$. (At P=50 ms, $I_h=0.83$ and $I_l=0.54$. The drives are between these values for all P and g_{ie} .) (The number of spikes per cycle thus computed ignores that for lower drives there will be cells firing at larger periodicities. The complexity in computing the map grows combinatorially beyond period two.) Hence by fixing an upper bound on the drives the cells $I_h(P = 50)$ and assuming a linear distribution of drives, we may plot the number of cells that fire for the values of g_{ii} and g_{ie} considered. Figure 3.7 shows clearly that, more cells fire with increasing g_{ii} , and decreasing g_{ie} .

The maximum spread of the phases at which the cells fire can be used to measure *coherence* of the e-cells. Figure 3.7 (bottom panel) indicates the variation in “coherence” $1/(1 - \phi_{min})$ with inhibition, where ϕ_{min} is the lowest value of phase among the firing e-cells at a given g_{ii} and g_{ie} . As expected, we find that coherence increases with increasing g_{ie} , that is, the cells fire closer together;

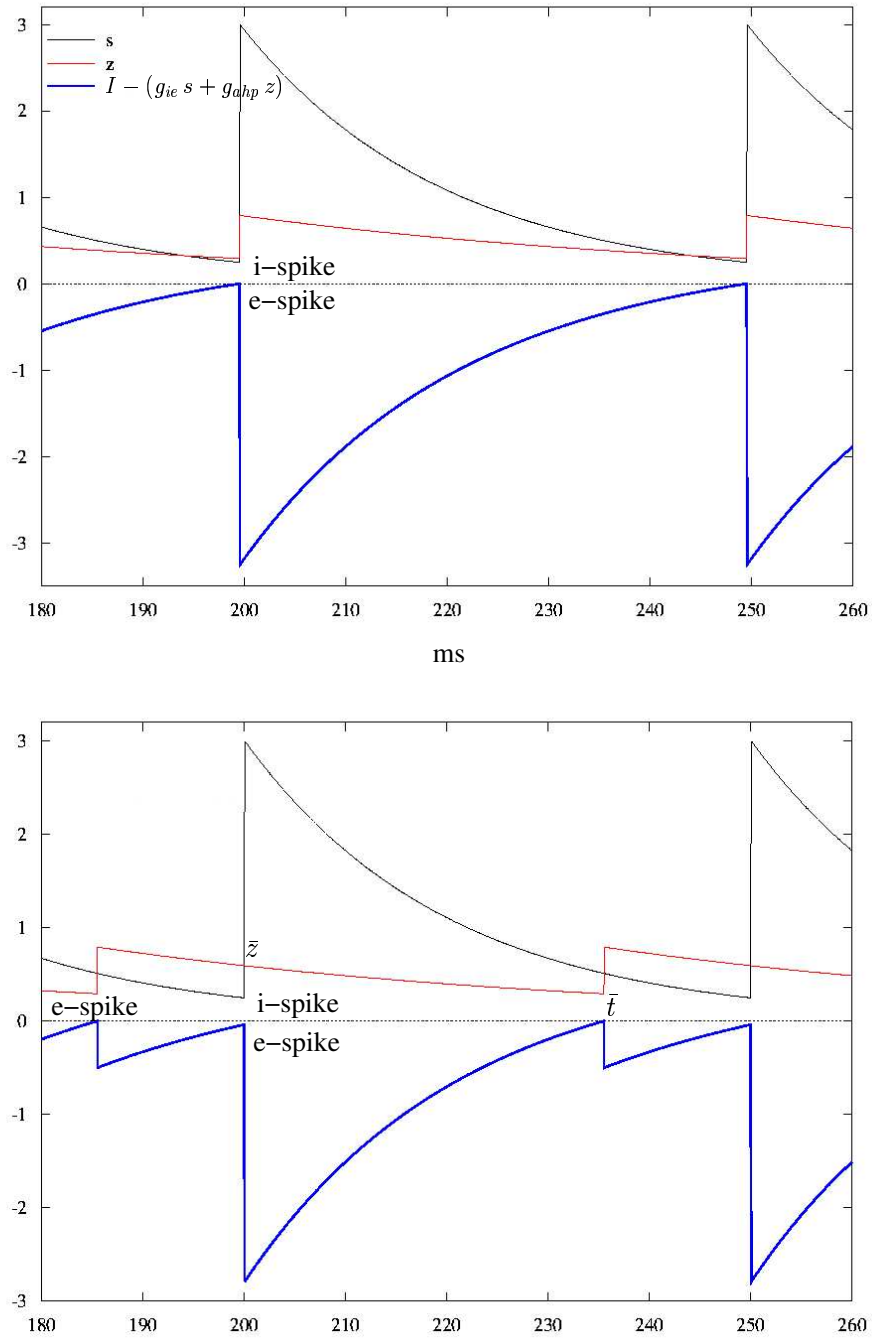


Figure 3.5. The variables in the analytic model. One i-period for two values of the “drive” I to an e-cell, I_l , (top panel) and I_h (bottom panel) is shown. The e-cell fires when the total inhibition ($g_{ie} s_i + g_{ahp} z$) wears off to the value I , i.e. blue curve touches zero. The i-cells are firing with a period of 50 ms in this example. If the I is too small the cell may be never fire in any one period, as the top panel suggests. If, on the other hand, I is large enough, the cell may recover sufficiently to fire more than one spike within that cycle (bottom).

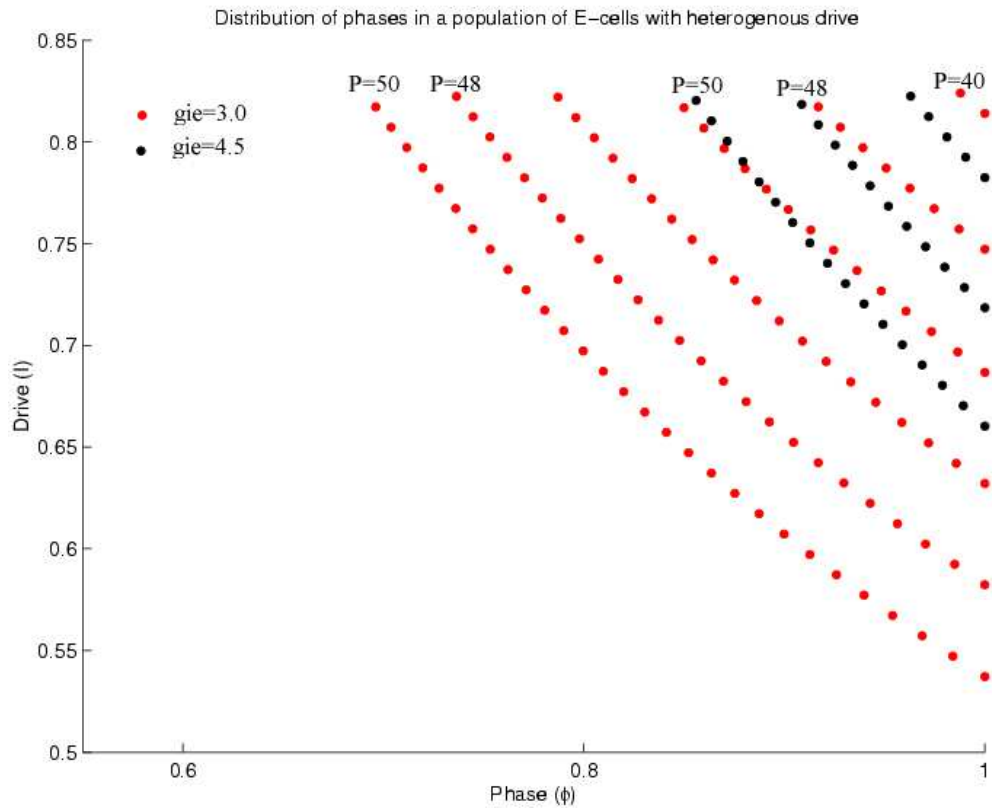


Figure 3.6. Phases of e-spikes relative to the i-period at different g_{ie} and g_{ii} numerically computed from Equations 3.2 through 3.5. Cells towards the top have the higher drives. The red dots indicate the lower value of g_{ie} than the black dots. The curves $P=50, 48, \dots, 40$ for $g_{ie}=3$ indicate the effect of a lowering the period, corresponding to smaller g_{ii} s. A similar set of curves are also plotted for $g_{ie}=4.5$ (with the black dot with the least phase being computed at $P=50$).

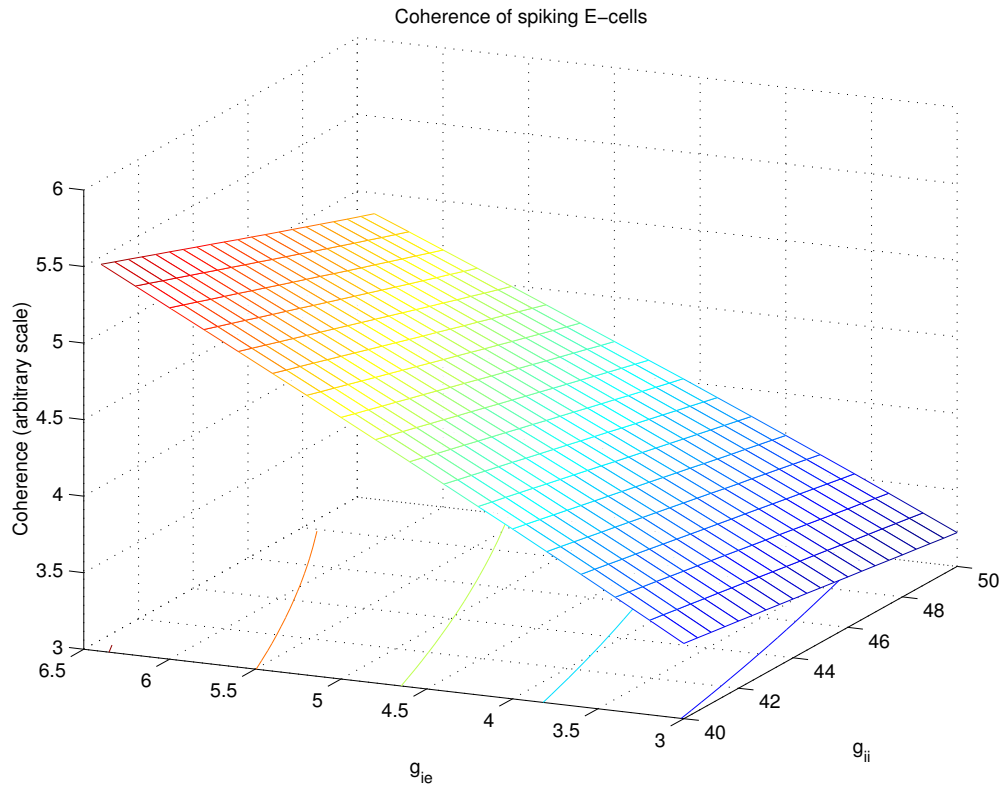
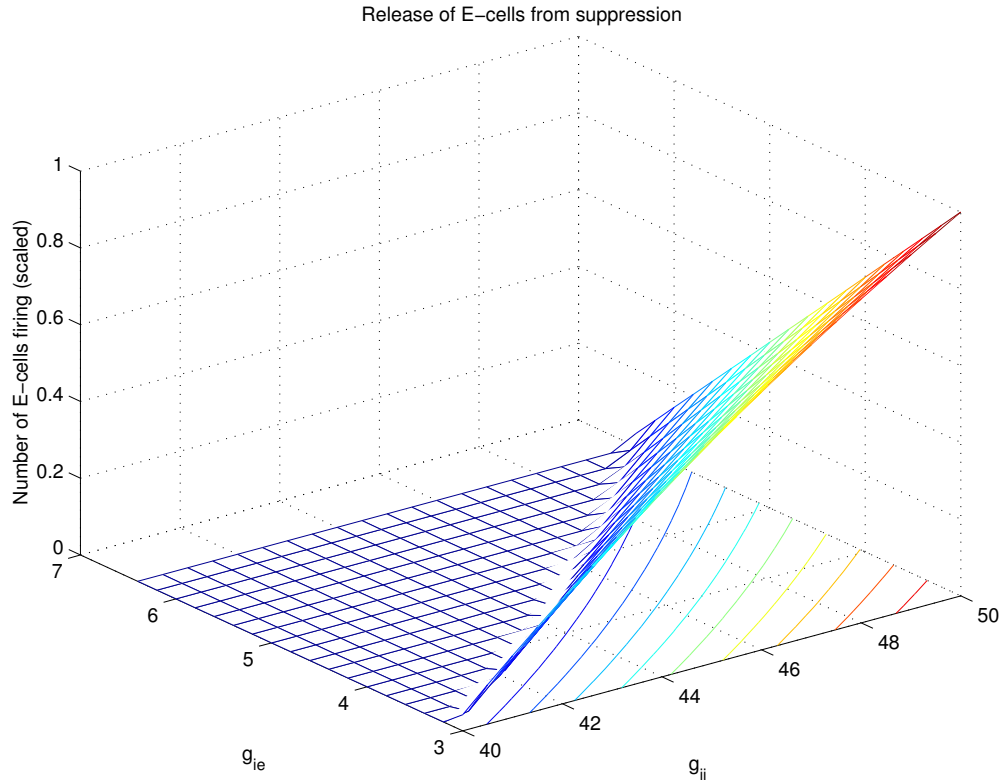


Figure 3.7. Total number of cells spiking at different g_{ii} and g_{ie} (top panel) as computed from the analytical model. (The scale is normalized by the maximal number of cells that fire at $P=50$ ms.) The bottom panel shows coherence (as defined in the text) of the spiking e-cells in a cycle, for various values of the inhibition.

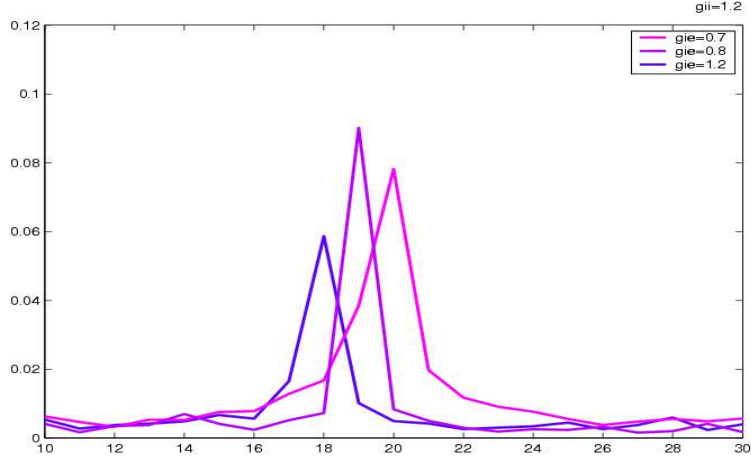


Figure 3.8. Non-monotonicity of the peak in the power spectrum of the total synaptic conductance with increasing g_{ie} . Parameters are as for the active state network.

it decreases with increasing g_{ii} .

We remark that with increasing g_{ie} , the number of e-cells that fire decreases, however, at the same time coherence increases, so that they fire closer together. This suggests the interesting possibility that in simulations it may be possible to obtain an *increase* in the power spectral peak on increasing g_{ie} . Indeed, as Figure 3.8 shows, a power spectrum of the total excitatory synaptic *conductance* shows an increase in the peak as g_{ie} is increased from 0.7 to 0.8. Note also the tighter coherence at 0.8. (Parameters used in this simulation correspond to those for the active state network, see below.)

3.4 Active Processing: the Effects of a Significant g_{ei}

When g_{ei} is sufficiently strong in the network, the number of e-cells firing has a significant effect on the period of the e/i network oscillation. In that case, as the average rate of e-cell firing increases with increasing g_{ii} , the increased excitation to the e-cells tends to increase the network frequency and counters the frequency-decreasing effect of increasing g_{ii} . Similarly, if g_{ei} is set high enough, as g_{ie} is increased the decreasing number of E-cells participating can lower the frequency of the network and allow more cells to fire, again countering the primary effect.

Figure 3.9 shows the spectral plots computed by varying g_{ii} alone, and then g_{ie} . The corre-

sponding histograms and rasters are shown in figures 3.10 and 3.11. The effect of increasing g_{ii} is seen to be typical: frequency shifts lower, and the spectrum is taller and broader; coherence can also be seen to decrease from the histograms and rasters in Figure 3.10. At a given value of g_{ii} , varying g_{ie} however, shows behavior that is in contrast to that of the resting state network (see above, section 3.3). As g_{ie} is increased frequency is seen to increase; this is reasonable, as argued above. Coherence does increase as expected, as seen from the histograms in Figure 3.11. (As a curiosity, we also remark that frequency does not change very much between values $g_{ie}=0.8$ and 1.0. This is because a significant proportion of the cells are firing on alternate cycles, presumably the net $e \rightarrow i$ influence is then not nearly strong enough.)

3.5 Discussion

Clearly, there is a tremendous gap between the quantities that experiments can measure and theories comprehensive enough to explain the observed quantities in terms to the intrinsic biophysical properties of (groups of) the participating cells. We try here to speculate on MEG data that indicates a beta rhythm sensitivity to benzodiazepines in the sensorimotor cortex. We model a population of 16 inhibitory, and 64 excitatory single-compartment neurons that generate an oscillation around 20 Hz. Interneurons are known to play a key role in generating gamma rhythms (30-90 Hz), specifically the type of rhythm dubbed ING. Here we claim that this beta rhythm is produced by a mechanism similar to hippocampal gamma, except at lower frequencies. Thus, interneurons generate a synchronous rhythm via recurrent inhibition; the pyramidal cells participate only weakly, they are more likely to be gated by the inhibition.

We have considered two cases, one when $e \rightarrow i$ synaptic influence is weak (the case most relevant to the experiments described here), and one in which their role might be more prominent. We claim that increase in the beta-frequency rhythm found in relaxed subjects given benzodiazepines comes from an increase in the inhibitory conductance *to the i-cells*. If the inhibitory conductance *to the e-cells* also increases with benzodiazepines, it does so at a lower rate, and is not the major cause of the increased beta power. Then our model predicts behavior that is consistent with the experimental results: increasing beta power with application of the drug, and the accompanying lowering of the frequency.

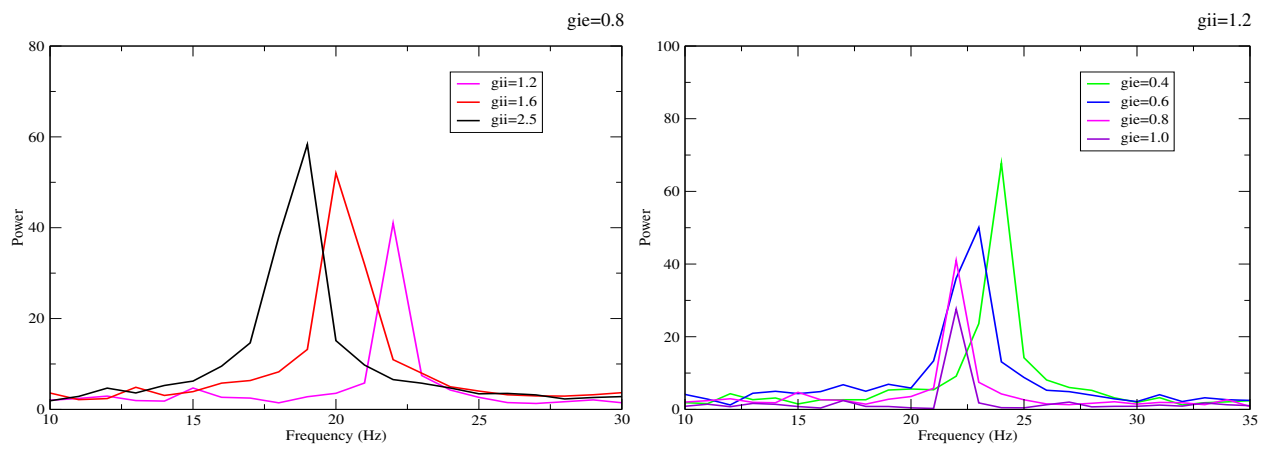


Figure 3.9. Spectra computed for the active state network, that is, when the role of g_{ei} is significant. (Contrast with Figure 3.1).

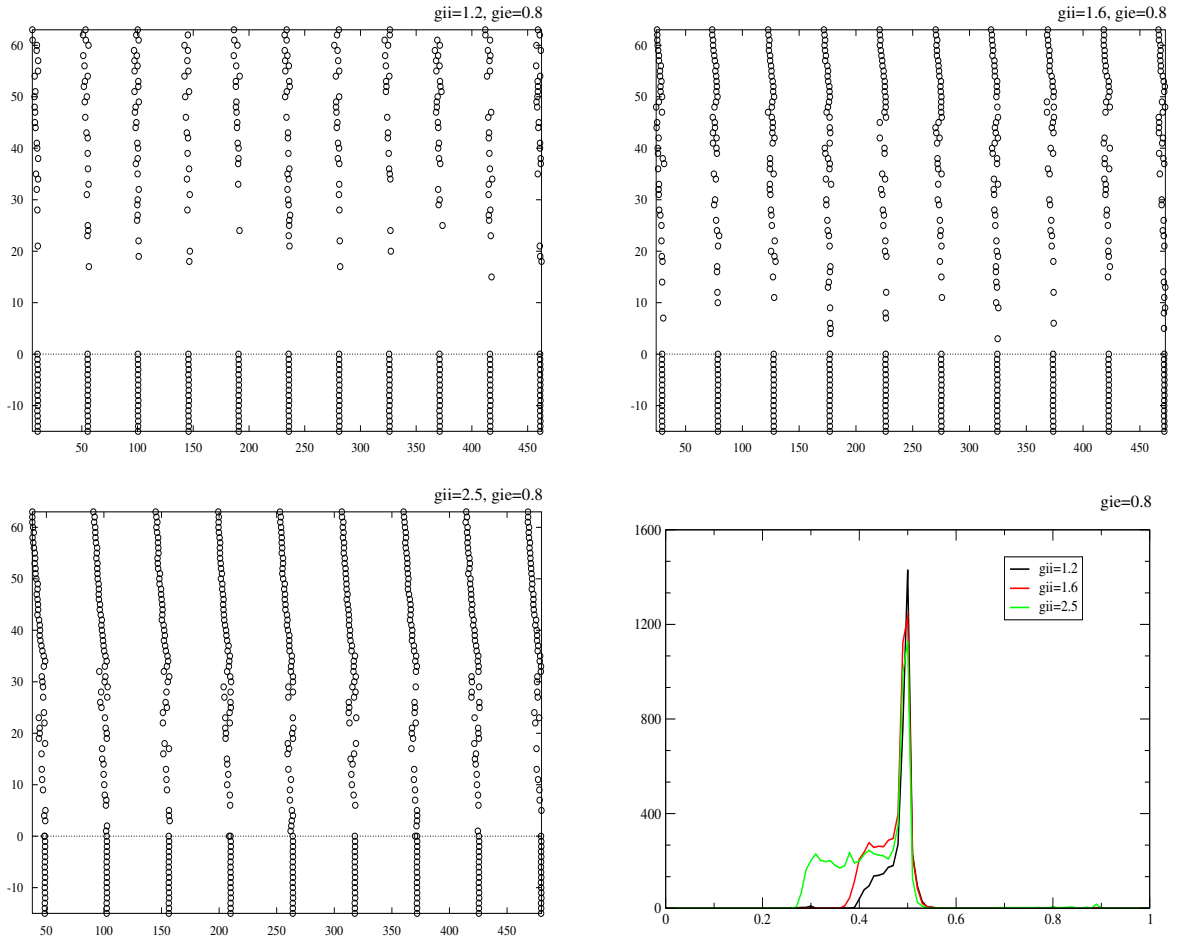


Figure 3.10. Rasters and histograms for fixed g_{ie} , and varying g_{ii} corresponding to the power spectra in Figure 3.9.

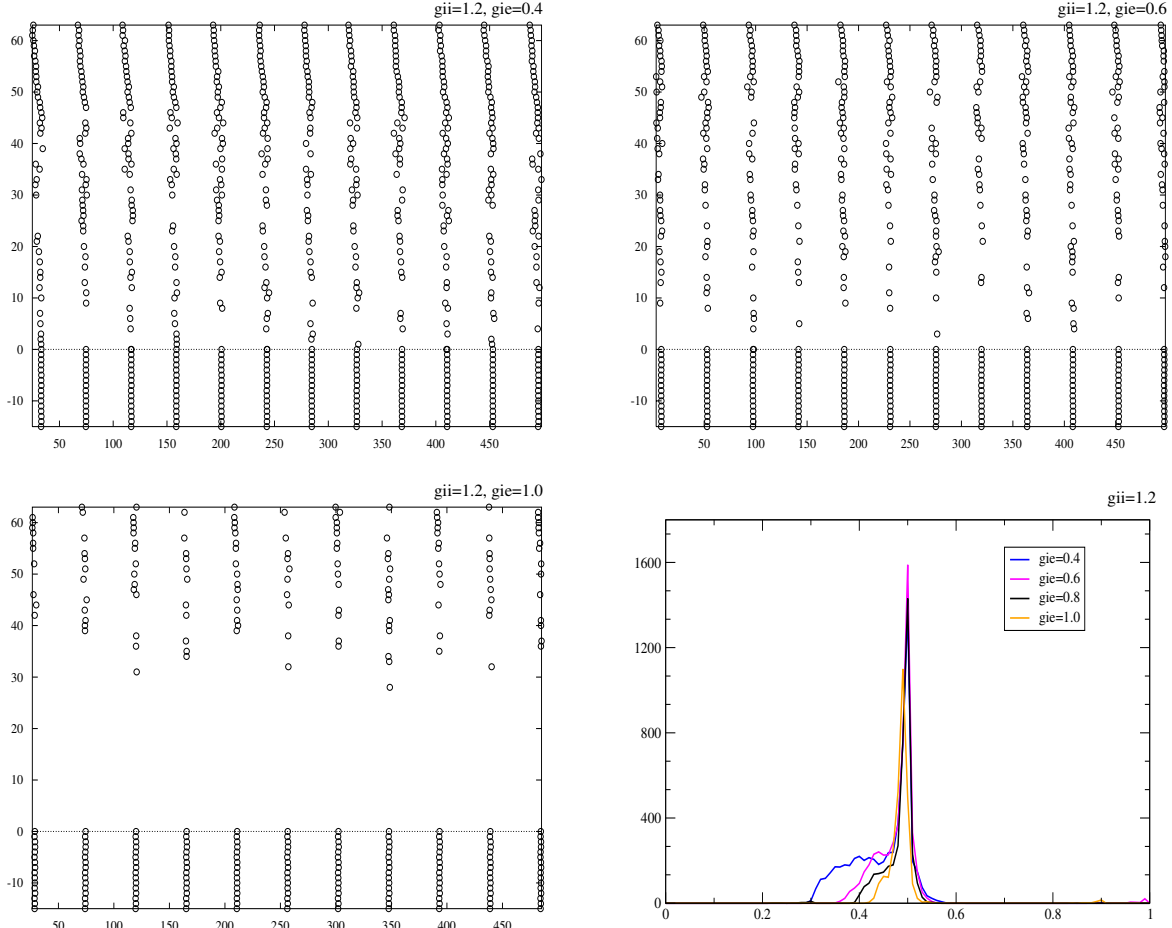


Figure 3.11. Rasters and histograms for fixed g_{ii} , and varying g_{ie} corresponding to the power spectra in Figure 3.9.

3.6 Appendix

The equations for each cell are obtained from a model of Traub and Miles for spiking [41]. The network consists of 64 e-cells and 16 i-cells connected all-to-all, but without any significant e-e coupling which is thought to be sparse in the cortex ($g_{ee}=0$).

The i-cells were modeled with equations

$$C \frac{dV_i}{dt} = -g_L(V_i - V_L) - g_k n^4 (V_i - V_K) - g_{Na} m^3 h (V_i - V_{Na}) - I_{syn,i} + I_0$$

and the e-cells by equations of the form:

$$C \frac{dV_e}{dt} = -g_L(V_e - V_L) - g_K n^4 (V_e - V_K) - g_{Na} m^3 h (V_e - V_{Na}) - g_{AHP} w (V_e - V_K) - I_{syn,e} + I_0$$

Both types of cells have a leak, a transient sodium, and a delayed rectifier potassium current. The e-cells have an additional AHP current in the form of a slow outward potassium current. Parameters and functional forms of the equations are taken from R. Traub & R. Miles [4], [41]. The gating variables, m, h, n satisfy equations of the form:

$$\frac{dx}{dt} = a_x(V)(1 - x) - b_x(V)x$$

for $x = m, h, n$ where

$$a_m(V) = 0.32(54 + V)/(1 - \exp[-(V + 54)/4])$$

$$b_m(V) = 0.28(V + 27)/(\exp[(V + 27)/5] - 1)$$

$$a_h(V) = 0.128 \exp(-(50 + V)/18)$$

$$b_h(V) = 4/(1 + \exp[-(V + 27)/5])$$

$$a_n(V) = 0.032(V + 52)/(1 - \exp[-(V + 52)/5])$$

$$b_n(V) = 0.5 \exp[-(57 + V)/40].$$

The gating variable, w satisfies

$$\frac{dw}{dt} = (w_\infty(v) - w)/\tau_w(V)$$

where

$$w_\infty(V) = 1/(1 + \exp[-(V + 35)/10])$$

$$\tau_w(V) = 400/(3.3 \exp[(V + 35)/20] + \exp[-(V + 35)/20]).$$

The maximal conductances were $g_{Na} = 100$ mS/cm², $g_K = 80$ mS/cm², $g_L = 0.1$ mS/cm², and $g_{AHP} = 0.3$ mS/cm². Reversal potentials are $V_L = -67$ mV, $V_K = -100$ mV, and $V_{Na} = 50$ mV. Parameters for both the e-cells and i-cells were the same; the only differences are in the synaptic

currents and the driving currents, I_0 . The synaptic currents were of the form:

$$I_{syn,\alpha} = g_{i\alpha}s_{i,tot}(V_\alpha - V_{in}) + g_e s_{e,tot}(V_\alpha - V_{ex})$$

for $\alpha = e, i$. Reversal potentials were $V_{ex} = 0$ mV and $V_{in} = -80$ mV. The synaptic gates are described by:

$$s_{\alpha,tot} = \frac{1}{N_\alpha} \sum_{\alpha\text{-cells}} s_\alpha$$

$$\frac{ds_\alpha}{dt} = a_\alpha(1 + \tanh(V_\alpha/4))(1 - s_\alpha) - s_\alpha/\tau_\alpha$$

where $a_e = 20/\text{ms}$, $a_i = 1/\text{ms}$, $\tau_e = 2.4$ ms, and $\tau_i = 20$ ms. The conductances, g_{ie}, g_{ii} varied and are given in the text; $g_{ee} = 0$ and $g_{ei} = 0.07$ mS/cm². White noise was added to the voltages and equations were integrated using Euler's method with a time step of 0.025 ms. Smaller values yielded no qualitatively different results. Simulations were done using XPPAUT (Ermentrout [34]).

Heterogeneity is introduced into the network by providing variations in the input currents (I_0) in the range 1.3 to 2.5 $\mu\text{A}/\text{cm}^2$ to the e-cells for the rest-state network and 1.6 to 2.6 $\mu\text{A}/\text{cm}^2$ for the active-state. The input currents to the the i-cells in the rest-state case is 7 $\mu\text{A}/\text{cm}^2$, and in the active-state 2 $\mu\text{A}/\text{cm}^2$. Choosing lower values of I_i and g_{ii} for the active-state is equivalent to a significant g_{ei} in the network.

The field measured by MEG is thought to be a consequence of the EPSCs produced by the e-cell spiking (Hamalainen [42]). The power spectrums in the simulation are computed by summing the EPSCs over all I-cells, i.e. a time series obtained by sampling the quantity

$$EPSC_{tot} = \sum_{i\text{-cells}} s_{e,tot}(V_{ex} - V_i).$$

in the integration (XPPAUT) is used to compute its FFT and estimate the power spectrum [43]. The power spectrum has units of (amplitude)²/Hz, i.e. ($\mu\text{A}/\text{cm}^2$)²/Hz.

We remark that the power spectral curve computed in any particular run varies from one simulation to the next. This is due to noise in the membrane voltage, and depends also on the initial conditions. To get a reasonable representative of the activity we compute an average over

several spectral curves.

Chapter 4

Analysis of the Disruption of Synchrony in Networks with Altered Excitatory Kinetics

4.1 Introduction

A critical question regarding gamma-frequency oscillations (30-90 Hz) in the hippocampus has been how synchrony arises between spatially distal sites, given the slow expected conduction times in the cortex. Traub *et al* [37] have suggested that interneuron doublets are critical to synchrony in the presence of delayed synaptic inputs. Ermentrout and Kopell [7] studied the physics of the system in a two-site model with a pair of excitatory and inhibitory neuron on each site, mutually coupled with negligible delay, and with significant delays between interactions across the two sites. Their analysis clarified the role of the interneuron doublets in encoding a feedback signal that allowed for the cells to synchronize stably. Synchrony thus arises as an emergent property of the network, without the necessity of a central pacemaker. Fuchs *et al* [1] have recently used molecular techniques and (large) network simulations to examine the role of the time constant of the synaptic drive to the interneurons in (disrupting) synchrony. The authors delineate three regimes with varying τ_e , the synaptic time constant of the excitatory postsynaptic potentials (EPSPs). With τ_e too big, or too small, synchrony in the network is degraded. Here we use maps similar to those used in the analysis in [7] to understand these results.

The present work relates to the earlier two studies in the following way: [7] laid the foundation for studying synchrony in presence of delay in a simplified 4-cell model. We use that framework to study (the stability of) synchrony in the presence of delay, but also for various values of τ_e . We are thus able to explain the experimental results in [1]. We also study features of the model itself, in particular the various activity patterns for different sets of parameters. The role of maps becomes clear as we describe the analysis. In particular, we compute a simple slope condition related to the maps (that was also obtained in [7]), to support results from direct simulation of the network dynamics.

4.1.1 The Findings of Fuchs *et al* [1]

Fuchs *et al* generated mice with slowed interneuron EPSPs by gene targeting. In both, the wild-type and mutant mice, tetanic stimuli evoked gamma oscillations (local field potential recordings *in vitro*, see Figure 4.1). Oscillation *synchrony* across spatially separated sites, however, was disrupted in the mutant. In addition, interneurons from wild-type mice fired in single spikes or spike doublets (recorded during the tetanus-evoked oscillation), whereas interneurons from the mutants fired doublets and triplets (Figure 4.1). (It was further confirmed that single-shock stimuli of interneurons (could) elicit single action potentials in the wild-type mice, whereas in the mutant, doublets could be evoked.)

The authors also carried out large network simulations [44] with values of τ_e altered to be a) larger than normal, and b) smaller than normal. Thus they divide the behavior of the network into three regimes, Figure 4.2¹. They conclude that in regime I, synchrony is weak because of fewer doublet firings if the EPSC is smaller and faster. In regime II, synchrony is sharp, and the interneuron autocorrelation shows the presence of doublet firings. In regime III the EPSC is more persistent and stronger, interneurons in the mutant fire triplets as well as doublets.

The analysis in Ermentrout and Kopell [7] essentially covers regime II, the “normal” conditions. In the appendix (published as supplementary data on the PNAS website, www.pnas.org), representative traces (i.e. averages of the e,i-cells at each edge of the “slice”) in the detailed simulations indicate a “doublet-triplet mismatch” occurs in regime III. They speculate on why this doublet-triplet mismatch disrupts the feedback necessary for synchrony in the context of the Ermentrout-Kopell model. The authors also point out that triplet firings by themselves need not necessarily disrupt synchrony, a point that we return to in our simulations. Here we revisit the model to study the effect of altering τ_e in greater detail. Our simulations reveal parameter regions in the τ_e -delay plane where the dynamics displays this predicted behavior. But first, we describe the Ermentrout-Kopell reduced model.

¹Remark on the notation used in the figure: τ_e is identical to τ_{AMPA} (or τ); excitatory synapses here are of the AMPA type.

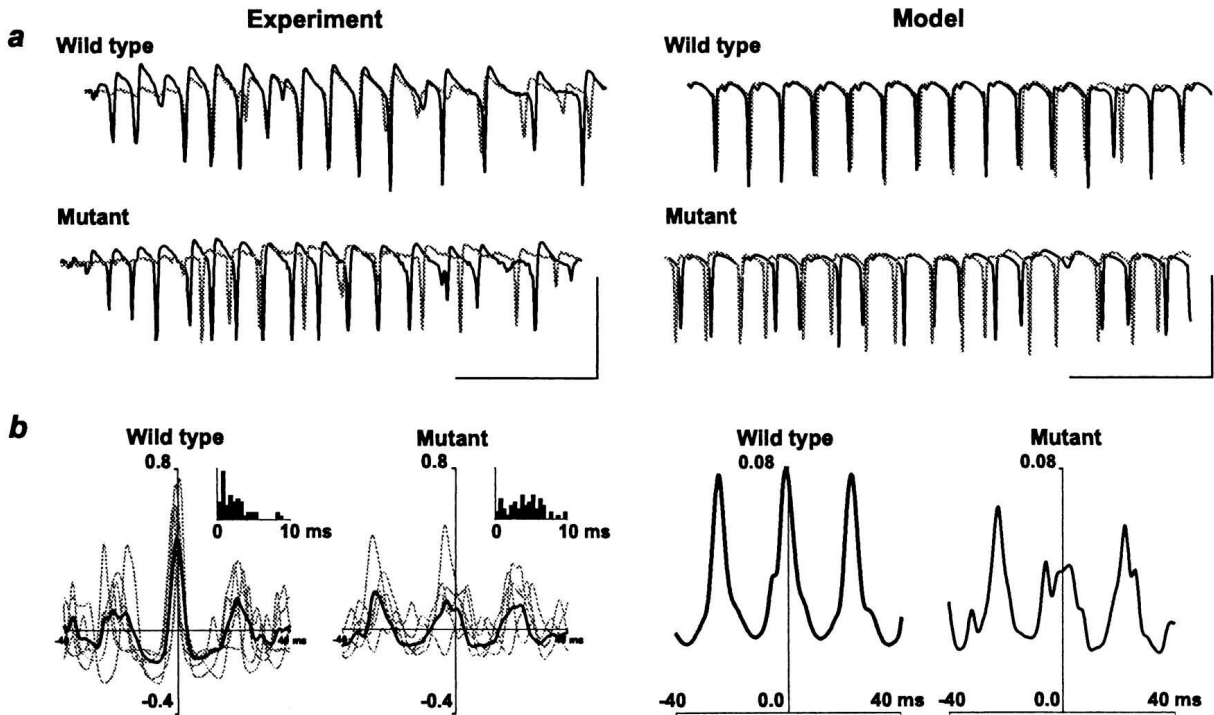


Figure 4.1. Figure 4 in [1]. Population gamma oscillations have disrupted synchrony in the mutant mice. (a) Example traces. Paired stratum pyramidale field potential recordings illustrated from the beginning of the posttetanic oscillatory response induced by paired tetanic stimulation. Recording site separation approximately 1 mm along the CA1 axis. Recordings are overlaid to illustrate temporal relationship between population spikes at the two sites. Oscillations from the mutant mice show a more erratic temporal relationship between spike generation at each site. (Scale bars: 3 mV, 100 ms.) Model data show superimposed average voltage signals, from two ends of the model array, for the two simulations (wild type and mutant). Each average was of 224 somatic pyramidal cell potentials, and the signals are inverted so as to resemble the experimental field potentials. Note the tight synchrony in the wild type, contrasted with the jittering back and forth in the mutant. (Scale bars: 50 mV, 100 ms.) (b) Pooled data showing pattern of phase relationship change in the mutant mice. Cross-correlations are taken from data as in a. Control data show mean cross-correlation plot for data from each of six wild-type mice (gray curves) and the global mean from these plots (black line). Inset shows distribution of modular phase relationships for 62 paired posttetanic gamma oscillations from 11 slices from six wild-type animals. Cross-correlation data from slices from mutant mice are represented in the same manner ($n = 5$ mice). Note erratic nature of central peak amplitudes. Inset shows distribution of modular phase relationships from 74 posttetanic oscillations from 15 slices from five mice. Model data show cross-correlations of 200 ms of data from the average signals shown in a.

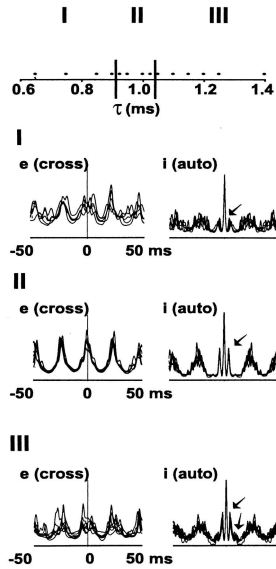


Figure 4.2. Figure 1 in [1]. Two-site synchronization occurs only over a narrow range of values for the decay time constant of interneuron AMPA-receptor-mediated EPSCs (simulations). Data are taken from 14 simulations, each with identical parameters, except for τ_{AMPA} (designated τ on the abscissa). The behavior of the system can be divided into three regimes: I, with $\tau \leq 0.9$ ms, having poor two-site synchrony; II, with $0.925\text{ms} \leq \tau \leq 1.025\text{ms}$, having good synchrony; III, with $\tau \geq 1.05$ ms, again with poor synchrony. In each regime, we plot superimposed cross-correlations of local average pyramidal cell voltages (e), from opposite ends of the array, using each simulation in that regime; and also superimposed autocorrelations of local average interneuron voltages (i), again using each simulation in the regime. In regimes I and III, the pyramidal cross-correlations lack a clear peak at 0 ms, and interneuron autocorrelation has either small, single side peaks (I), or double side peaks (III) (arrows). In regime II, in contrast, there is a sharp peak near 0 ms in the pyramidal cross-correlation, and single, sharp side peaks in the interneuron autocorrelation, the latter corresponding to synchronized interneuron doublet firing.

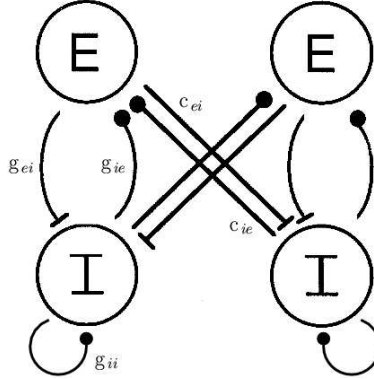


Figure 4.3. The reduced network: a pair of local circuits, each with an e-, and i-cell. Conduction delays are significant only across columns.

4.1.2 The Simplified Biophysical Model

In order to elucidate the dynamic behavior of a larger network it is easier to consider a reduced model with the excitatory and inhibitory populations each represented by a single neuron. Two copies of such a pair representing the two edges of a slice are coupled together by a conduction delay. Remarkably, as shown in [7], such a minimal model captures the essential dynamics very effectively.

Figure 4.3 shows a schematic of a two-column model consisting of pair of local circuits consisting of pyramidal cells and interneurons at two sites some distance apart. Pyramidal \rightarrow interneurons connections are modeled as AMPA receptor-mediated excitatory synapses, while interneurons innervate pyramidal cells via GABA(A)ergic inhibitory synapses. The biophysical equations modeling each cell are obtained from the reduction of a model of Traub and Miles for spiking [41]. e-e connections are thought to be sparse in the CA1 region of the hippocampus, and such connections are not included in the model (i.e. $g_{ee}=0$). Conduction delays are negligible within a column, but significant across all interactions between columns. We also leave out i-i connections across columns. Only those i-cells that are connected together without appreciable delays are assumed to be part of a local circuit. Interneurons are modeled with self-coupling to account for inhibition from within the local population.

4.1.3 ING and PING rhythms

Traub and colleagues [41] have classified gamma rhythms as produced by essentially two different network topologies. Clearly, interneurons must play a significant role in these rhythms (mutual excitation in a population of only excitatory cells would be uncontrollable). Thus Interneuron Gamma, or ING, is a mode of activity in which strong recurrent connections between interneurons produce network rhythms at gamma frequencies. Pyramidal cells either do not participate in the rhythm, or if they do, they do not contribute to shaping the frequency significantly, i.e. they are gated by the i-rhythm. (We considered this type of rhythm in the last chapter.) Network frequency in Pyramidal-Interneuron Gamma (PING), on the other hand, involves both pyramidal cells, and interneurons in synergy. Typically, pyramidal cells are inhibited by interneurons (slowed down), and interneurons are excited (sped up) by pyramidal cells. Recurrent connections between the two populations interact to produce gamma rhythms. The model considered here is an example of a PING network.

The i-cells can be modeled as modeled either as excitable (does not fire without input) or tonically firing, and receiving self-inhibition (which can come from other cells of this population). The i-neuron is a Type 1 neuron. Type 1 neurons can have an arbitrarily long latency to firing after stimulation. For an excitable cell, this means that, as the cell receives increasing amounts of depolarized injected current, it becomes oscillatory through a saddle-node bifurcation. That is, the onset of repetitive firing can occur at arbitrarily low frequencies. For a tonically firing cell, it ceases oscillations with sufficient hyperpolarizing current, again through oscillations of arbitrarily low frequency.

When the system is sufficiently close to synchrony, each e-cell fires one pulse per cycle (with further pulses halted by the inhibition), and each i-cell fires one, two, or three pulses (in response to excitation from the extrinsic and intrinsic e-cells).

Each reciprocally coupled e-i pair is an oscillator. In the simulations, sustained tonic currents drive the (isolated) e-, i-cells to spike periodically. The experimental justification of this follows from the stimulus protocol [41]. Brief tetanic stimuli - 20 pulses at 100 Hz - are delivered simultaneously to the stratum radiatum proximal to the cell body layer at two recording sites at either end of the CA1 region (separation 0.7-1.1 mm) every 4 minutes throughout each experiment. Repetitive electrical stimulation of sufficient intensity (8-30 V, 50- μ s duration) induce large (upto 20mV)

depolarizations in both pyramidal and interneurons that typically last for hundreds of ms. A latent period - about 125 ms - following the stimulus, gamma oscillations begin. (Note that gamma is a *network* rhythm; in an experiment action potential trains in isolated pyramidal cells or interneurons are markedly different from the network oscillations.)

4.2 Regions of Stable Synchrony in the $\tau_e - \delta$ plane

We use the four-cell network described above to check if synchrony is stable while varying the delay parameter, δ , for different values of τ_e . (Since we are only interested in the asymptotic *stability* of synchrony,) each run is started with initial conditions sufficiently close to synchrony. The equations are integrated for a total time of one second, allowing transients to decay sufficiently. We then compare the firing times of the two e-cells in a cycle; we take them to be synchronized only if they fire to within half a millisecond of each other. The results of the simulation are plotted in Figure 4.4. (We remark that the plot here thus does not give any indication of the domain of attraction of a stable solution.) Several regions of synchrony can be detected. The patterns of i-cell firings are however different in these different regions, as the following table shows:

A, B, C	synchrony, with i-cell triplets
D, E	synchrony, with doublets
F	synchrony, with singlets

We will now show that it is possible to understand this behavior in the full network (i.e. the four-cell network) by studying a *reduced map*, as in [7], *that encodes the response of a single i-cell to two temporally dispersed excitatory inputs*.

4.3 Reduction to a Map in the Ermentrout-Kopell Model

By reducing the network to a two-site, four-cell network, naturally one loses details of the various biophysical processes that exist in the “real” network *in vivo*, or even *in vitro*. The advantage of studying a minimal model lies in the hope that it may be possible to specify the interactions between cells in a relatively complete fashion, at least to a first order. (Of course, perhaps not surprisingly, even in this simplified model the patterns of activity can become very complex.) Under

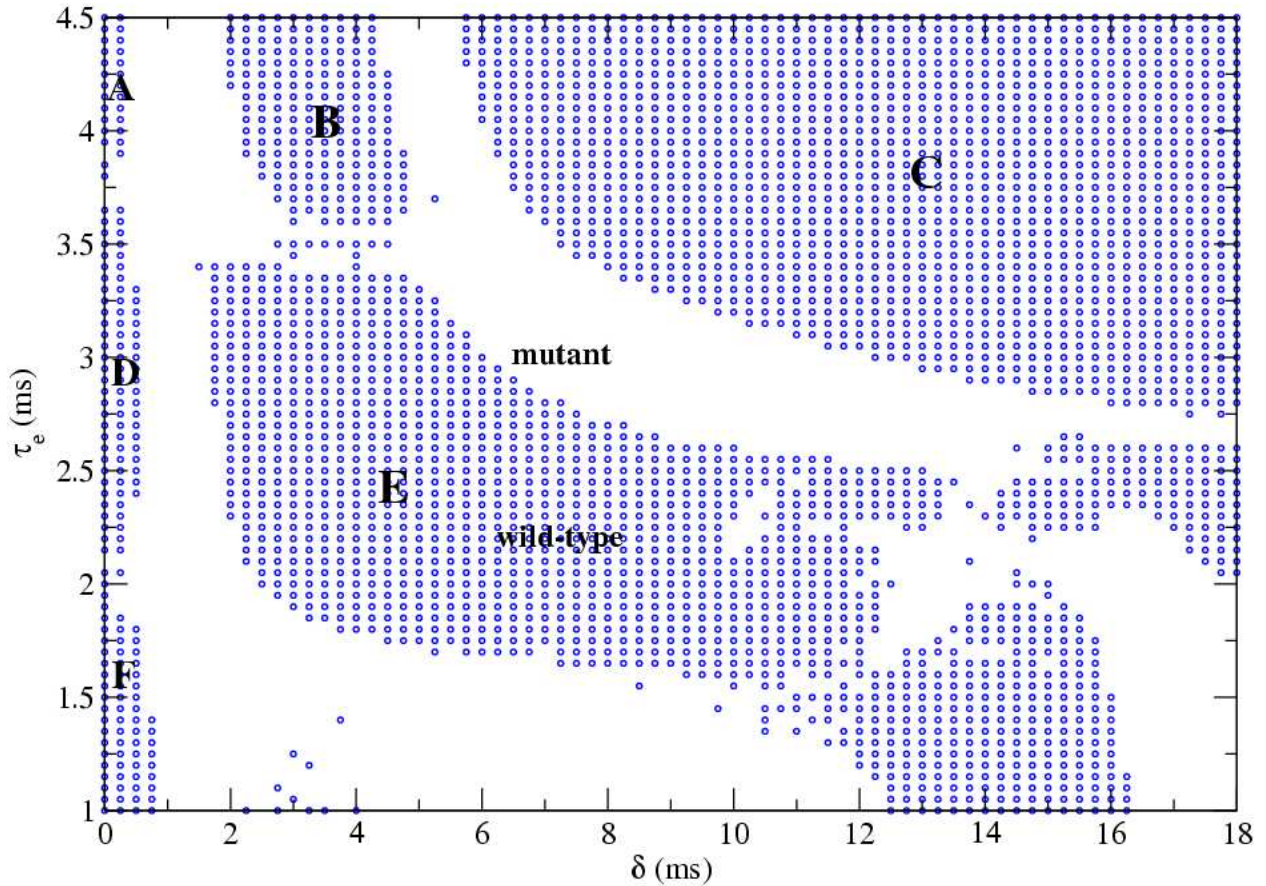


Figure 4.4. The phase plot of synchronous behavior in the τ_e -delay plane as computed in the two-site, four-cell network. Synchrony is marked in blue. Voltage traces show that in regions A, B and C (both) interneurons fire triplets, in regions D, E, doublets, and singlets in F. Also indicated are the regions that correspond to parameters for the interneuron firing patterns seen in wild mice (synchrony through interneuron doublets), and mutants (loss of synchrony) [1].

the assumption that spikes are thin (with respect to the period) the times of spikes can be specified. If, in addition, we make certain assumptions on the nature of the coupling (e.g. the topology of connections and the direction of influence, the biophysical behavior (type) of synapses), it becomes possible to specify firing times on *successive cycles* through the order in which cells influence each other during the cycle. That is, one can derive a *map* that produces the time difference between the two e-cell spikes (say) from one cycle to the next. Synchrony then corresponds to a fixed point of this map at a time difference of zero. We assume that the system is close to synchrony; we can then use the maps to see if the dynamics brings the system closer to synchrony or further away.

Here we briefly recall the details of the construction of the maps, which closely follows [7]. (In

the canonical case,) each e-cell fires once per cycle. Each i-cell receives an (excitatory) input from the e-cell in the same column, and another from the e-cell of the other column *after a delay*. It may fire one, two, or three spikes depending on the decay constant of the EPSC, and the particular value of the delay. (Note that in [7], the i-cell fires doublets, with the first spike being in response to the excitation from the same column and the second due to the delayed excitation from across the columns. Here, we generalize to the cases where either doublets or triplets can, in addition, arise due to local excitation alone. This is due to the longer time constant for synaptic decay that we consider.) Thus (close to synchrony) the oscillation follows the following mechanism:

1. Each e-cell in either column (say column 1) fires and induces the local i-cell to spike. Let t_1 be the time that e1 spikes and t_2 be the time that e2 spikes.
2. Each i-cell cell, say i1, experiences excitation due to the extra-columnar e-cell, i.e. e2, after a delay, δ . In some circumstances, this may cause another spike in the i1 (if the delay is timed such that the i1 has recovered from its refractoriness and is able to fire again) or it may only modulate the period of the next i-spike. Spike(s) from i1 suppress e1 immediately, but influence e2 only after a delay.
3. e1 receives inhibition from i1 and, after a delay, from i2. It is released from suppression when the total inhibition has decayed sufficiently. e2 fires again by the same mechanism, *mutatis mutandis*. Let \bar{t}_1 be the time that e1 spikes again (i.e. on the next cycle), and \bar{t}_2 be the time that e2 spikes again.

We can use two preliminary maps to consider separately the effects of the response of the i-cell and that of the e-cell to their inputs. T_I encodes the response of the intrinsic i-cell to excitation from the intrinsic and extrinsic e-cell. (It also gets self-inhibition, which we consider to be a part of the definition of the intrinsic dynamics of the i-cell.) Let ψ be the time between the receipt by an i-cell of the excitatory pulses from the intrinsic and extrinsic e-cells. We let $T_I(\psi)$ be the time after the second excitatory input at which the (intrinsic) i-cell fires next, Figure 4.5. $T_I(\psi)$ depends on the parameters of the i-cell and the strength of the synapses onto the cell. $T_I(\psi)$ can be computed by considering an e-i column coupled to an extrinsic e-cell *without delay*; a stimulus (whose time we can control) is applied to (cause) the extrinsic e-cell to fire at various times with

respect to the intrinsic e-cell to mimic conduction delays. Notice that near synchrony, due to the delay the spike from the extrinsic e-cell is always received later than the spike from the local e-cell; thus ψ is always positive. (In some phase-locked states, this need not be the case.) We shall make the approximation that the effect of the last two spikes received by an e-cell is much more important than that of any previous ones in determining its next firing time. This approximation is valid because the inhibitory synapses are close to saturation after one spike so that a later spike of inhibition wipes out the information from an earlier spike (both coming from the same cell).

The other map, T_E , encodes the response of an e-cell to (the last) two inhibitory pulses. T_E can be derived as follows. Let t_{ie} denote the time after the e-cell fires that the i-cell of the same circuit fires last, assuming no other input. And let ϕ be the time between the arrival of the last two spikes at an e-cell. In absence of the extrinsic input an e-cell is released from suppression when the inhibition decays to some value $g^* = g_{ie} \exp(-(t_p - t_{ie})/\tau)$, where t_p is the period of the uncoupled circuit, and τ is the inhibitory decay time. If then, there is also inhibition from the extrinsic i-cell (near synchrony) it is received later by the e-cell, in which time the inhibition from the intrinsic cell has decayed to a value $g_{ie} \exp(-\phi/\tau)$. The sum of the two inhibitory conductances then decays to the value g^* in the time

$$T_E(\phi) = \tau \ln\{e^{-\phi/\tau} + c_{ie}/g_{ie}\} + t_p - t_{ei} \quad (4.1)$$

after the last input to the e-cell.

The time that e1 fires on the next cycle can be derived as follows. Recall that t_1 and t_2 denote the times that the intrinsic and extrinsic e-cells fire on some cycle. Let $\Delta = t_2 - t_1$. Inhibitory pulses from I_{int} and I_{ext} are received at E_{int} at the following times, with the following paths:

1. $E_{int} \rightarrow I_{int} \rightarrow E_{int}$. Arrives at $t_1 + t_{ei}$.
2. $E_{ext} \rightarrow I_{ext} \rightarrow E_{int}$. Arrives at $t_2 + t_{ei} + \delta$.
3. $E_{ext} \rightarrow I_{int} \rightarrow E_{int}$. Arrives at $t_2 + \delta + T_I(\Delta + \delta)$.
4. $E_{int} \rightarrow I_{ext} \rightarrow E_{int}$. This pulse is sent from I_{ext} at $t_1 + \delta + T_I(\Delta + \delta)$ and arrives at E_{int} at $t_1 + 2\delta + T_I(-\Delta + \delta)$.

We make the approximation that the effects of the latter two spikes is more important than that of the first two. This assumption is valid because the inhibitory synapses are close to saturation

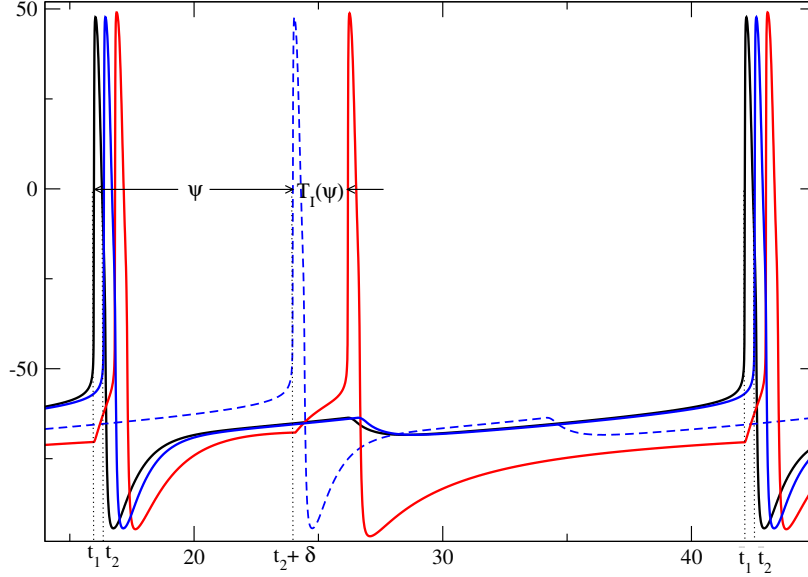


Figure 4.5. An i-cell (red) fires in response to excitation from the intrinsic (black) and extrinsic (blue) e-cells. Note that although the two e-cells are firing very close to each other, the EPSP from the distal site is experienced by the i-cell only after the delay δ (dashed blue). The map $T_I(\psi)$ thus encodes the response of the i-cell to two e-inputs, temporally dispersed by an amount ψ . T_I is then defined as the (next) firing time of the i-cell since the *last* received e-pulse. Note that since the inhibitory synapses are close to saturation (section 4.3) upon firing once from immediate local excitation, we make the assumption that the time of the last i-spike in the cycle is most relevant to the dynamics of the network: that is, T_I is measured upto whichever is the last i-spike in that cycle.

after one spike: thus the third spike of inhibition wipes out the information from the first, and the fourth does the same for the second. Pulses 3 and 4 are clearly the last to arrive at E_{int} .

Thus the times \bar{t}_1, \bar{t}_2 at which E_{int} and E_{ext} fire again can be specified as

$$\bar{t}_1 = t_1 + 2\delta + T_I(-\Delta + \delta) + T_E(-\Delta + \delta + T_I(-\Delta + \delta) - T_I(\Delta + \delta)), \quad (4.2)$$

with \bar{t}_2 obeying a similar formula with indices 1 and 2 reversed, and the replacement $\Delta \rightarrow -\Delta$. We thus obtain a map for the difference between the timings of the two e-cells on consecutive cycles, $\Delta \mapsto \bar{\Delta} = (\bar{t}_2 - \bar{t}_1) \equiv G_\delta(\Delta)$

$$G_\delta(\Delta) = \Delta + F_\delta(\Delta) - F_\delta(-\Delta) \quad (4.3)$$

where

$$F_\delta(\Delta) = T_I(\Delta + \delta) + T_E(\Delta + \delta + T_I(\Delta + \delta) - T_I(-\Delta + \delta)). \quad (4.4)$$

4.3.1 Analysis of Synchrony

The synchronous solution is given by $G_\delta(0) = 0$, and is stable if $|G'_\delta(0)| < 1$. This in turn means that

$$-1 < F'_\delta(0) < 0, \quad (4.5)$$

where $F'_\delta(0) = T'_I(\delta) + T'_E(\delta)[1 + 2T'_I(\delta)]$.

Recall that $T_E(\phi)$ is essentially independent of ϕ for large ϕ , Equation 4.1. We also note that taking the limit $c_{ie} \rightarrow 0$ implies that the map

$$T_E(\phi) = -\phi + t_p - t_{ei} \quad (4.6)$$

is linear in ϕ . In our simulations we shall neglect long-range i→e connections (and take $c_{ie} \approx 0$). When $c_{ie} \rightarrow 0$, $T_E(\phi)$ is independent of any influence from the extrinsic i-cell; however, it formally serves as a bookkeeping device to locate the position of the next e-spike.

Taking $T'_E = -1$ from Equation 4.6, the stability boundary occurs for $T'_I(\delta) = -1$, when $F'_\delta(0) = -1$. *We thus obtain the slope of the T_I map as an index of (a)synchrony.* Note that a map that is stable to perturbation expresses the fact that, mechanistically speaking, there is a feedback process in the network that drives cells towards the stable solution on successive cycles. That is, if either e-cell is driven away from (stable) synchrony, the network exerts a corrective effect to drive the cells together on the next cycle.

An alternate derivation of the above result is given in [7]. The derivation given there does not rely on taking the limit of a vanishingly small c_{ie} . Instead, it supposes that i→e connections across columns do not exist at all. The analysis follows along lines such as above, but with the essential difference that each e-cell receives two pulses of inhibition and not four, both from the intrinsic i-cell (spikes 1 and 3 above) alone. In that case, T_E is interpreted as encoding how the e-cell responds to two inputs from its *own* circuit. The condition on the slope of the T_I map for stability of synchrony that is arrived at then, is identical to the one here (see also, [7] for additional details of the algebra).

Equation 4.5 (and the corresponding condition on T'_I) says that if we compute T'_I for a given τ_e , we should be able to predict the (loss of) synchrony in the full network by determining if

slope of T_I is (greater) less than 1 in magnitude. Recall (section 4.3) that the map $T_I(\psi)$ can be computed for several values of ψ , by applying two excitatory stimuli ψ ms apart to an i-cell and measuring the time taken for the i-cell to fire since the last input. We will examine some such maps below; for example, Figure 4.12 (right panel) shows the map computed for $\tau_e = 4$. At (network) synchrony then, an i-cell receives two e-inputs a time $\psi = \delta$ apart, since the local excitation arrives immediately while the extrinsic excitation takes a time precisely δ to arrive. Thus: to look for stable synchrony for a given value of delay *in the full network* (at a given τ_e), one picks out the slope of the map, $T_I'(\psi = \delta)$ (computed for that value of τ_e); if *this* slope is less than 1 in magnitude, synchrony ought to be stable, else not.

We will next examine the behavior of the network for various values of τ_e and δ . We shall compute $T_I'(\psi)$ (and its derivative) at different τ_e and correlate the regions of synchrony in the network to regions in the map where the slope is less than unity. The process of computing the map (described above) indicates whether an i-cell will respond with singlets, or doublets, or triplets to two excitatory inputs, and this will also enable us to predict firing patterns in the full network.

In order to fix these ideas, we will begin by describing the dynamics in network in the case considered in [7], which we find in our phase plot 4.4 at parameter values $\tau_e = 2, \delta = 7$ (say). Then, we shall consider three different sections of the plane at $\tau_e = 1.5, 3$ and 4 which are representative of the regions of synchrony in $\tau_e - \delta$, as broadly classified above. For each of these cases, we examine the voltage traces from simulations of the full network to identify the different activity patterns; we also compute the map T_I to verify if it predicts the onset of synchrony.

4.4 Dynamics of Synchrony in the $\tau_e - \delta$ plane

At parameter values, $\tau_e = 2$ and $\delta = 7$, synchrony can be seen to be stable, as in Figure 4.4 (full simulation). A simulation, Figure 4.6, shows that in absence of input from the extrinsic cell (by setting $c_{ei} = 0$) an i-cell fires only one spike per cycle. Figure 4.7 (left panel) shows the response of the i-cell to two excitatory inputs a time ψ apart. Another excitatory input arriving at short time later evokes a second spike in the cell. (It is the time of this second spike that is plotted in the figure.) Thus if two e-cells in the full network are synchronized, and the delay in the network is a value $\delta = \bar{\delta}$, the response of the i-cell in the network can be read as $T_I(\bar{\delta})$. The right panel plots

the slope of the T_I curve. By the analysis in the previous section, if synchrony is to be stable in the full network, the figure indicates that ψ (or equivalently, the delay, in the full network) must be greater than 2.36 (as can be read off readily in Figure 4.7 on the right). Indeed, the boundary of the stable region E in Figure 4.4 lies close to this value ($\delta \approx 2.25$). We remark that this parameter set corresponds to experimental observations in *wild-type* mice: recall that synchrony is mediated by interneuron “doublets”. The analysis with the map shows that synchrony is not possible for very short delays.

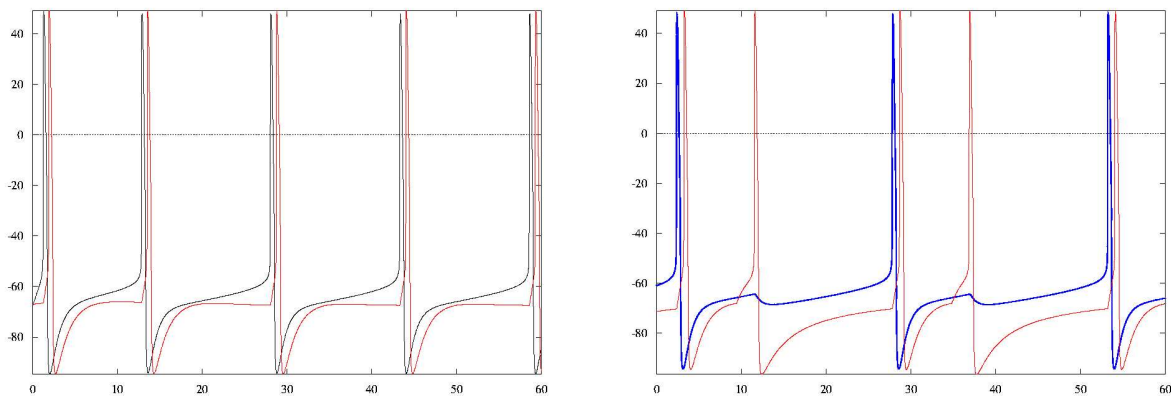


Figure 4.6. $\tau_e = 2$, $\delta = 7$. *Left*. An EPSP in an i-cell from the intrinsic e-cells alone evokes single spikes, e-cell in black, i-cell in red. *Right*. In the full network e-cells (blue and black overlaid) are synchronized through interneuron doublets (red).

We now turn to the various other regions in the Figure 4.4.

4.4.1 $\tau_e = 3$

We begin by describing the dynamics at a section $\tau_e=3$ of the phase-plot in Figure 4.4. Five qualitatively different regions can be seen in the figure: at very small values of the delay one observes that synchrony is stable, for somewhat larger delays unstable, then stable, and unstable again and stable for large delays. Figure 4.8 shows spiking activity in the cells in each of these different regions. Note that in the plots (a), (b), (c) and (e) the i-cells fire doublets; in plot (d) half the i-cells fire doublets, the other half triplets, and in (e) both i-cells fire triplets. Evidently, with larger delays in the network it becomes easier to evoke triplets in the i-cells due to the clear separation of excitation from the local and distal e-cells. The role of local and extrinsic circuits in

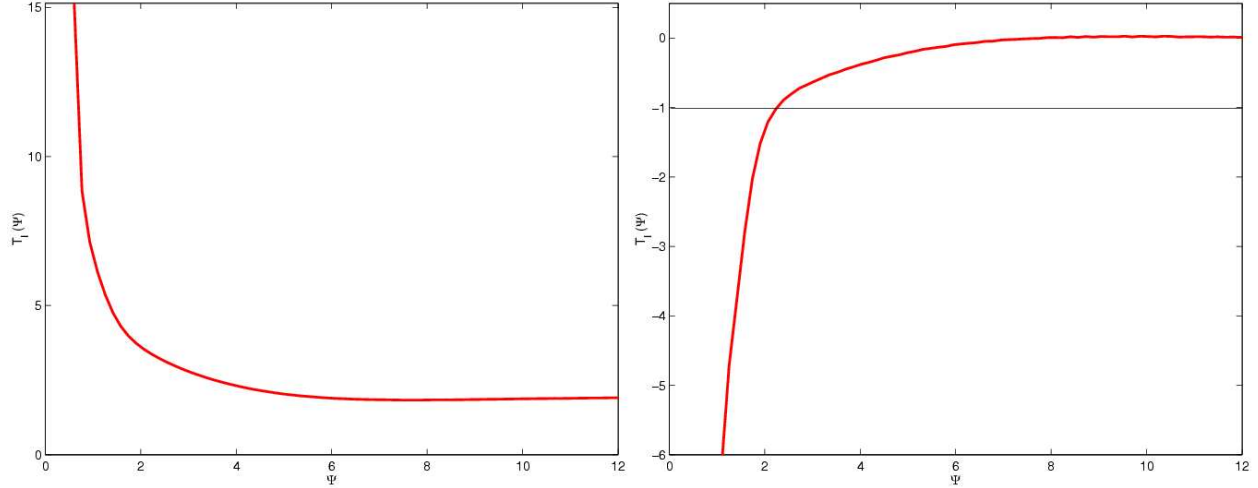


Figure 4.7. The T_I map (left), and its slope (right) at $\tau_e=2$. Note that the slope $-1 < T_I' < 0$ for $\psi > 2.36$.

evoking either doublets or triplets in an intrinsic i-cell is made clear by looking at the T_I map for $\tau_e=3.0$, Figure 4.9.

4.4.1.1 The T_I map.

Figure 4.9 shows the map T_I for increasing values of ψ . Only the last elicited spike is plotted in the graph. There are, qualitatively, three pieces to this curve, marked blue, black and red. We find that $\tau_e = 4$ is large enough to evoke spike doublets due to intrinsic excitation alone. For $\psi < 6.9$ (blue curve), the second excitatory arrives soon enough that it can modify the timing of this “intrinsic” interneuron doublet. For $\psi > 6.9$ (black; broken), the later e-input arrives *after* the second i-spike, and hence the time of the doublet is determined by the intrinsic pulse alone. Here the slope of the “doublet” T_I is therefore -1. It is not difficult to estimate the critical value of ψ for which a *third* spike may be evoked due to the second excitatory input. (This is the value of ψ corresponding to the vertical asymptote of the “triplet” curve (red).) Due to the saddle-node nature of these (Type 1) neurons, this third spike can appear after an arbitrarily long latency. The e-cells, however, recover from suppression in finite time (and the cycle is terminated). Thus, in the simulations of the full network i-cells effectively fire doublets in this regime. ($\psi < 9.4$ was estimated from a direct computation of the map). For $\psi > 9.4$ (red curve), as the map shows, the i-cell fires

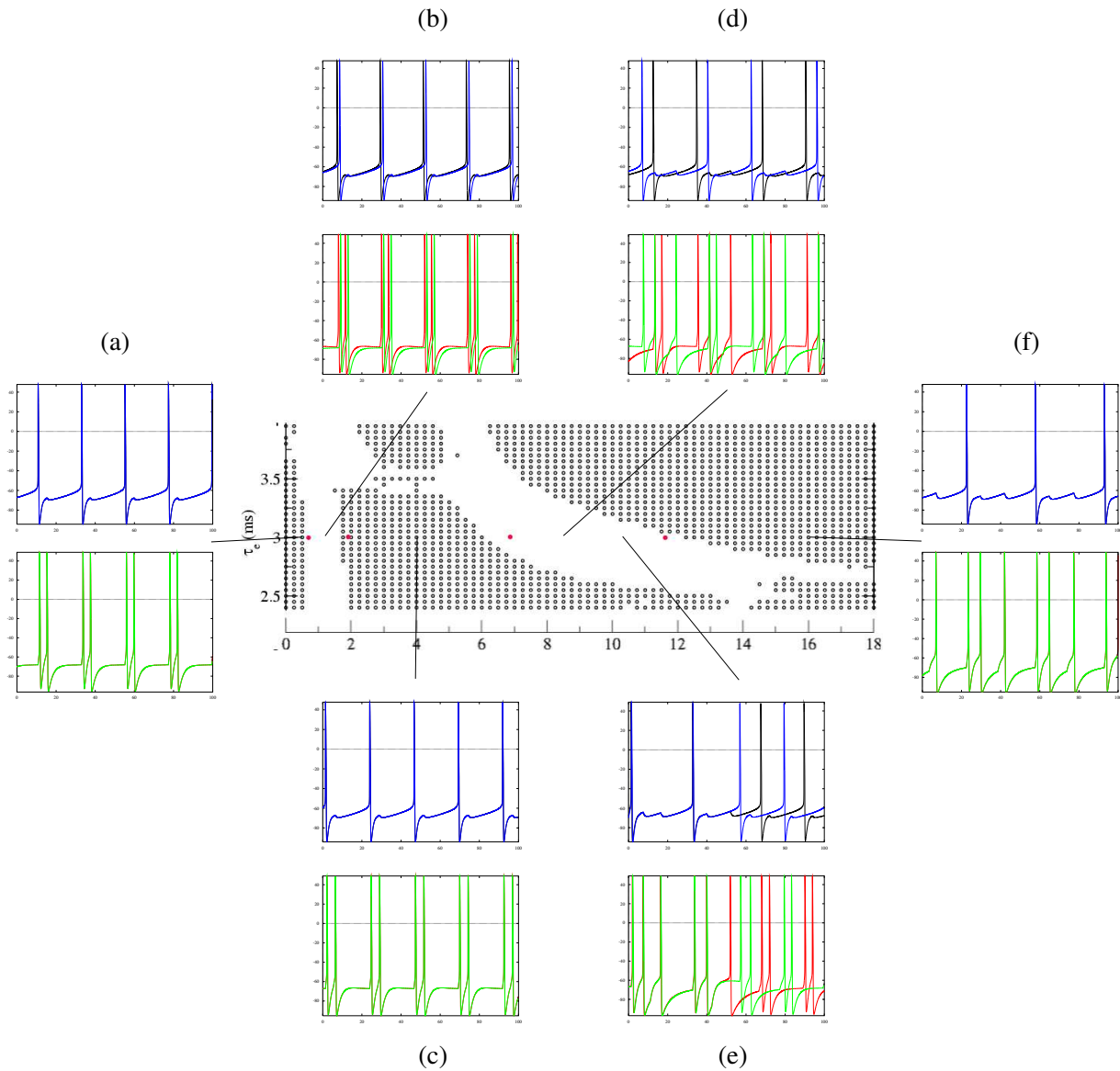


Figure 4.8. The phase plot of synchronous behavior in the τ_e - δ plane around $\tau_e=3$. Traces of activity in the e-cells (black, blue) and the i-cells (red, green) are shown at points representative of the different regions with increasing δ . The plots are computed at values of delay $\delta = 0.5, 1, 4, 8, 9.7, 16$; $\tau_e = 3.0$. Note, in particular, the dots in red that mark where the slope of T_I evaluated for $\tau_e=3$, crosses -1.

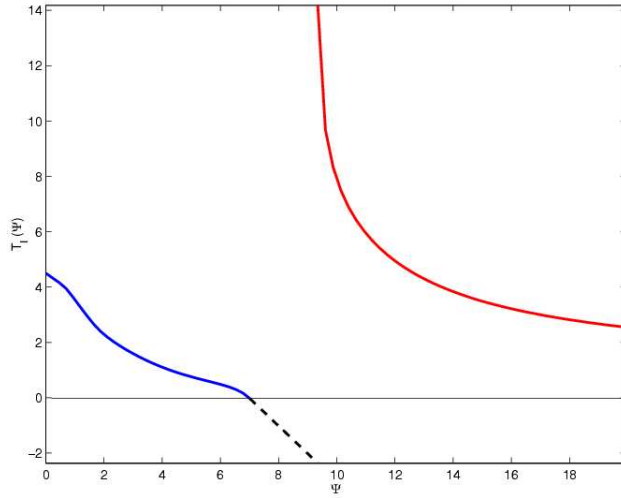


Figure 4.9. The T_I map at $\tau_e=3$. The red curve indicates a firing of triplets. For lower values of δ , however, the excitation does not arrive late enough to induce a third spike (blue). For $\delta > 6.9$ (broken curve), distal excitation can no longer influence the second spike.

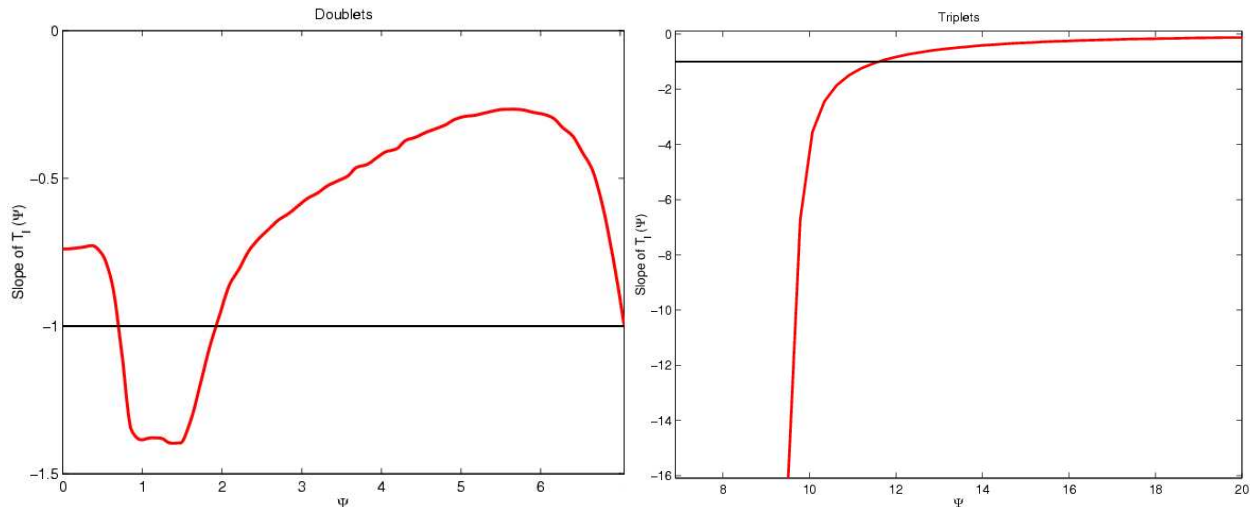


Figure 4.10. The slope of the T_I map in the “doublet” regime (left), and in the “triplet” regime (right) at $\tau_e=3$. The slope crosses the line $T_I'=-1$ at the points $\psi = 0.7, 1.9$ and 6.9 successively (left panel); and 11.61 (right). Notice that the rightmost point on the abscissa on the left is the same as the leftmost abscissa point on the right i.e. the two panels may be “concatenated” with respect to the horizontal axis..

a third spike soon enough to inhibit the (intrinsic) e-cell within that same cycle.

4.4.1.2 $\delta=0.5$.

The slope of the T_I map is greater than -1 , and we expect that synchrony is a stable solution. Figure 4.8 (a) shows the spike activity computed in the simulation. The upper panel indicates the spikes of the e1 (in black), and e2 (in blue), and the lower panel shows activity of the i-cells, i1 (in red), and i2 (in green). An overlap of the black and blue, and red and green, curves indicates a sub-millisecond phase difference between the cells. We remark on the difference between the mechanism of doublet firing here and in [7] (which arises from the larger value of τ_e). In [7] (as in the case $\tau_e = 2$ above) the second spike of the doublet arises from a delayed excitation arriving from the inter-columnar e-cell (a case that we consider below). With a more persistent excitation (larger τ_e) each interneuron can fire doublets in rapid succession under the influence of the local e-cell alone; the distal excitation, if received soon enough, modulates the T_I map, resulting in a non-constant slope. Synchrony is possible if this slope is shallow enough.

4.4.1.3 $\delta=1$.

Figure 4.8 (b) shows that synchrony is unstable. This is also corroborated by looking at the slope of the T_I map at $\psi=1$ in Figure 4.10, the slope in this region takes a steep dive below -1 . Nevertheless, with initial conditions that are close to the synchronous state, a small perturbation drives the system into a nearby phase-locked position. Since the system is symmetric with respect to the two columns, the solution with the identities of the two columns reversed (i.e. spike times with i,e-cells 1 and 2 reversed) is also equivalent to the latter. Thus, (starting from initial conditions near synchrony), a symmetry-breaking bifurcation leads to either of the two phase-locked positions. Numerically, this phase-locked solution seems to be stable. We now reason the existence of this solution. Suppose that on some cycle e1 fires ahead of e2, the figure shows that i1 spikes ahead of i2 (both spikes in the doublet, compared pairwise). Then, if t_{i1} and t_{i2} denote the spike times of the second spikes of the respective i-cells: e1 receives a delayed inhibition from i2, and a local inhibition from i1. Clearly, the latter arrives later. So the time e1 spikes again is given by $t_{i2} + \delta + T_E(t_{i2} + \delta - t_{i1})$. e2, on the other hand, receives its inhibition from t_{i1} delayed, and local inhibition from i2. So that the time that e2 spikes again is given by $\max(t_{i1} + \delta, t_{i2}) + T_E(|(t_{i1} + \delta) - t_{i2}|)$. Note that the effect of the delay is to bring t_{i1} and t_{i2} “effectively” *closer* (i.e. decreasing ϕ) with regard to e2, and *farther* (i.e. larger ϕ) with respect to e1. Since the T_E map decays with ϕ , e1 continues to fire sooner than e2 on the next cycle. (Indeed, algebra of the usual kind reveals the fixed point $\bar{\Delta} \approx \delta$. This is not, however, entirely accurate since in this case (i.e. locking with a phase difference comparable to the delay) it becomes important to distinguish the local and distal spikes in the computation of the T_I map. That is, $T_I(\psi; e_i \text{ then } e_j) \neq T_I(\psi; e_j \text{ then } e_i)$. Of course, this issue does not arise in the calculation considering synchrony since $\psi = \pm\Delta + \delta$ is always positive: the perturbation in either e-cell can be made smaller than any value of delay without loss of generality. So the spike from the distal e-cell is *always* experienced later than that from the local column.)

4.4.1.4 $\delta=4$.

Figure 4.8 (c) shows synchrony is stable. The slope of the T_I map is greater than -1 . This region is qualitatively similar to the case $\delta = .5$ considered above. Excitation from the extrinsic e-cell arrives with a delay so as to modify the time of the interneuron spike doublet, but not sufficiently late in the cycle to evoke a third spike (Figure 4.9). This region of stability spans delays over nearly

5 ms.

4.4.1.5 δ around 8.

As the delay increases beyond $\delta=6.9$, the extrinsic excitation is received late enough that the timing of the second spike in the local cell is entirely unaffected (black curve in Figure 4.10). The slope in T_I for doublet firing is therefore $= -1$.

Near a value of δ greater than 6.9, then, the i-cell can fire *triplets* . The relevant slope to consider is that for the “triplet” T_I map, Figure 4.10, right panel. As noted earlier, this third spike can be evoked after an arbitrarily long time so that slope of the map is large here. And the network loses its synchrony.

A common pattern of firing in this region, Figure 4.8 (d) at $\delta = 8$, results from a *doublet-triplet mismatch* [1]. Say e1 fires ahead of e2 in some cycle, then the prolonged EPSP will cause the i1 to fire triplets (local plus distal excitation). Since the spike from e1 is received by i2 after a delay, e1 and e2 are temporally less separate for i2 than for i1. Thus, i2 may only fire doublets. The extra inhibition from the triplet spikes pushes the i1 farther out so that the order of spiking of the two e-cells is reversed on the next cycle.

As delays become greater than 9.4, triplets can be evoked with latencies comparable to the period of the oscillations. The T_I slope however, is large and negative, and synchrony continues to be unstable. A commonly recurring solution in this region (as seen in simulation) shows that anti-synchrony seems to be the preferred mode of locking here. Figure 4.8 (e) shows e-cells started near synchrony quickly step out of phase. (Notice that this implies that the frequency of the rhythm doubles, i.e. a field potential recording of the network population will indicate a power spectral peak at twice the frequency of the individual cells.) Although this is one (of the more likely) possible solutions, other solutions may well exist in this regime: the (arbitrarily) delayed i-spike can influence firing in complex ways. Ermentrout and Kopell indicate the existence of chaotic solutions in a similar regime (see also below).

4.4.1.6 $\delta=16$.

The T_I slope is nearly zero; synchrony is stable. Triplet spikes form at both sites, Figure 4.8 (f). Note that the frequency of the rhythm is somewhat slower due to the larger delays in the

circuit. However, with such a low slope while synchrony is stable, locking is very weak. Hence heterogeneity in the cells is not likely to be tolerated, even less so for larger delays. Figure 4.11 shows the results of adding the same amount of heterogeneity in the drives to the two e-cells for two nearby values of δ . For larger δ (and smaller slope) synchrony is broken, while at slightly lower δ the cells continue to lock nearby.

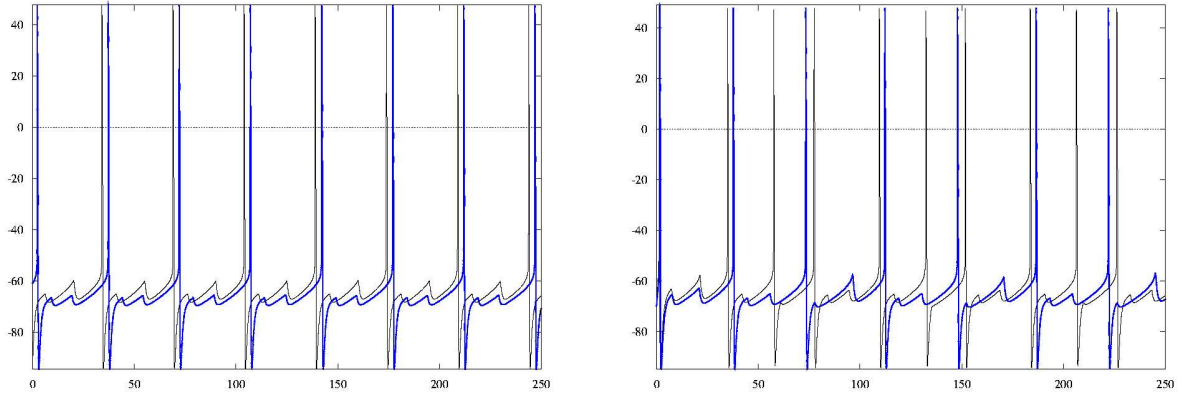


Figure 4.11. $\tau_e = 3$, $\delta = 15$ (left), and 17. There is a 14 % heterogeneity in the drives to the two e-cells. For larger delays, synchrony is weaker.

4.4.2 $\tau_e=4$

We next consider the effect of an even larger τ_e on the dynamics of synchrony. In this regime, τ_e is sufficiently large to evoke intrinsic triplets in each i-cell. (Distal excitation, however, modulates the timing of the i-spikes.) Figure 4.14 shows a computation of the T_I map, and Figure 4.12 shows the corresponding regions in $\tau_e - \delta$. Synchrony is lost in the regions of delay where the slope is more negative than unity. For large values of the delay, the last i-spike is evoked with nearly a fixed latency, so the slope of T_I is nearly zero, and synchrony is feeble.

4.4.3 $\tau_e=1.5$

At the rather low value $\tau_e=1.5$, Figure 4.4 shows that synchrony is largely unstable. This is in keeping with experiment and large-scale simulations; doublets have been noted to be *necessary* for synchrony.

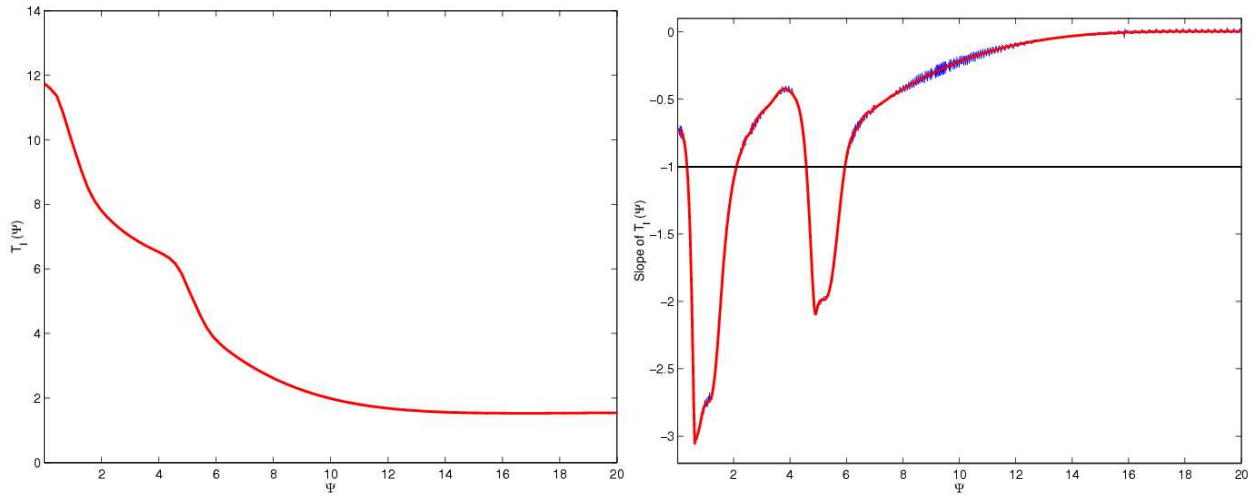


Figure 4.12. The T_I map (left), and its slope (right) at $\tau_e=4$. The slope curve in red is a piecewise polynomial fit to the numerical data (blue; overlaid). The slope crosses the line $T_I'=-1$ at the points $\psi = 0.35, 2.1, 4.58, 5.95$ successively.

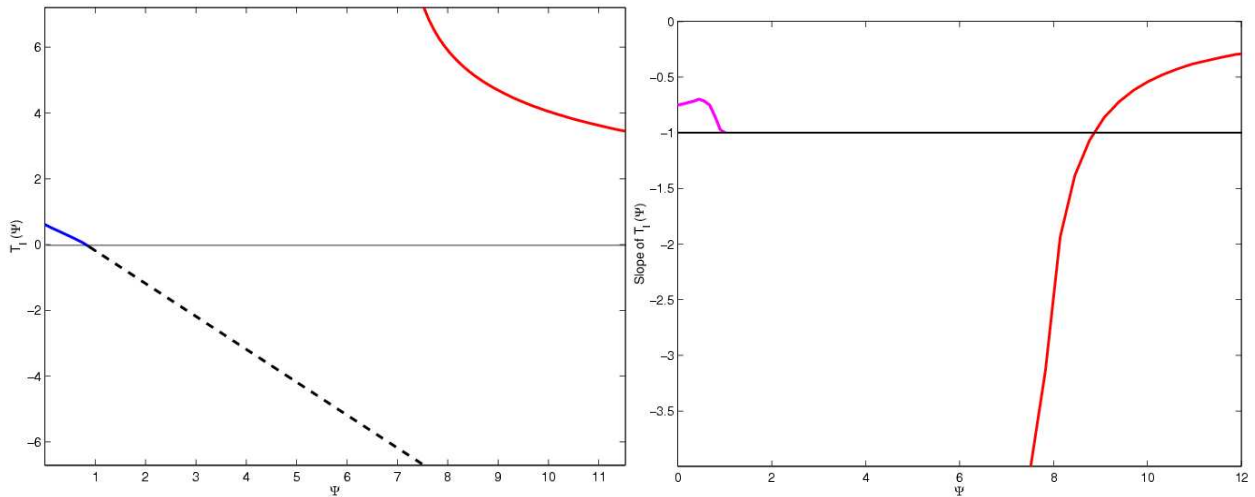


Figure 4.13. The slope of the T_I map in the “singlet” regime (blue), and in the “doublet” regime (red) at $\tau_e=1.5$. The slope crosses the line $T_I'=-1$ at the points $\psi = 0.9$ and again at 8.9. Note that at 7.2 the doublet is evoked soon enough to affect phase in the same cycle.

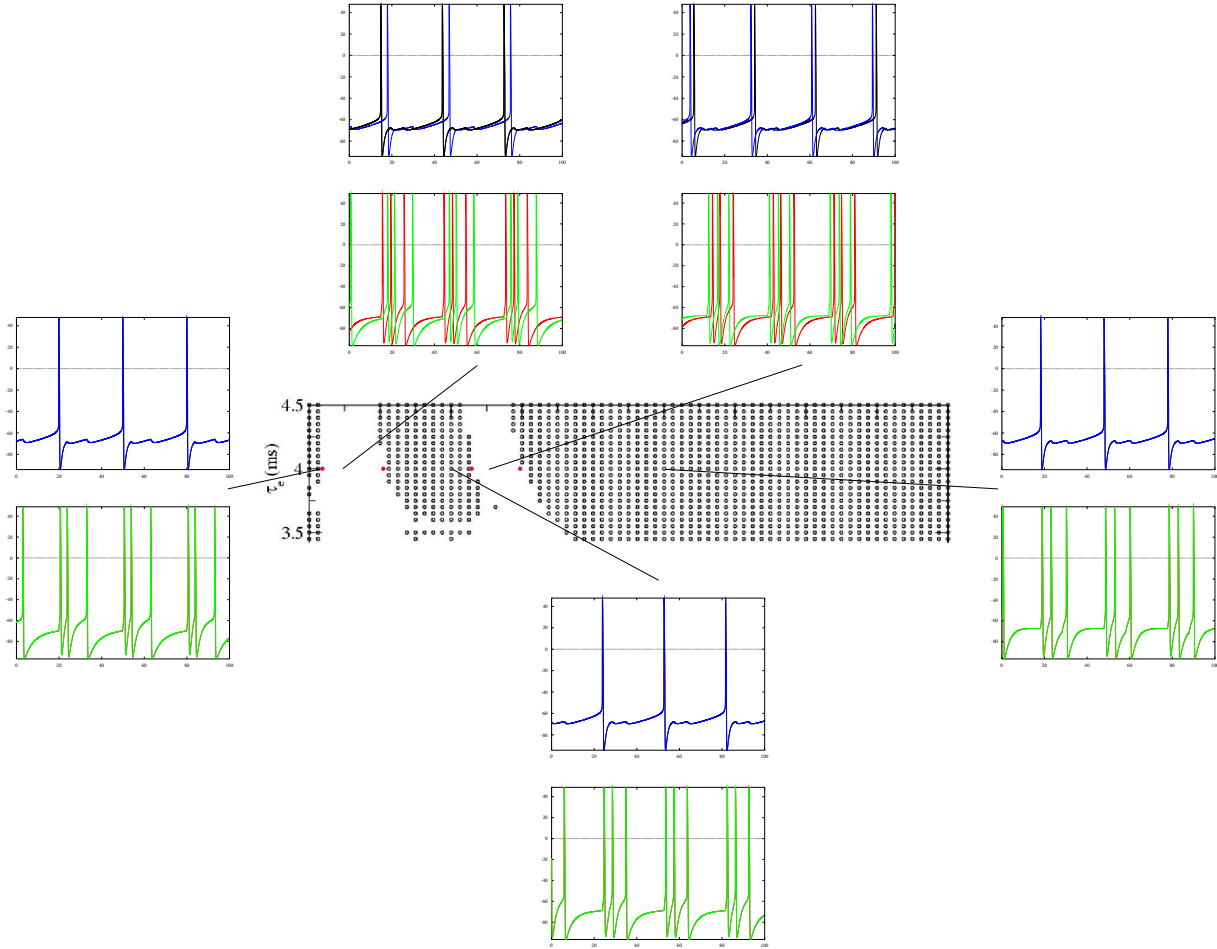


Figure 4.14. The phase plot of synchronous behavior in the τ_e - δ plane around $\tau_e = 4$. Traces of activity in the e-cells (black, blue) and the i-cells (red, green) are shown at points representative of the different regions with increasing δ . The plots are computed at values of delay $\delta = 0.25, 1, 4, 5, 10$; $\tau_e = 4.0$. Note, the dots in red that mark where the slope of T_I evaluated for $\tau_e=3$, crosses -1.

Stable solutions are seen to form for very small values of δ , Figure 4.15. For very small values of delay, each i-cell can fire only single spikes. This condition disappears around $\psi=0.9$, Figure 4.13, where it now becomes possible that each i-cell can fire doublets. Due to the large response times of the i-cells involved, complicated firing patterns, can develop. For example, at $\tau_e=5$, a chaotic seeming solution can be seen in simulations, figures 4.17 and 4.18. At about $\psi=8.9$, the T_I maps predicts that stably synchronous solutions can form. Indeed, the simulations indicate nearby regions in τ_e - δ plane where synchrony is present. However, we note that in this case, i-cells (can) fire

doublets with latencies comparable to the delay times involved. Thus it is not clear that the map idea is particularly useful in such a regime. Complicated firing sequences can develop, and are difficult to study unless on a case by case basis. (e.g. at $\delta=14$, the e-cells are synchronized with i-cell *singlets*, but at a rather high frequency of 66 Hz.) On the other hand, the map suggests that the *anti-synchronous* solution might also be possible to obtain. We see such a solution at $\delta=7$ for example, figure 4.19. We remark that the map itself, Figure 4.13, breaks down at $\psi = 11$ or so. This is because the inhibition is weak enough that the e-spike of the next cycle truncates any further measurement.

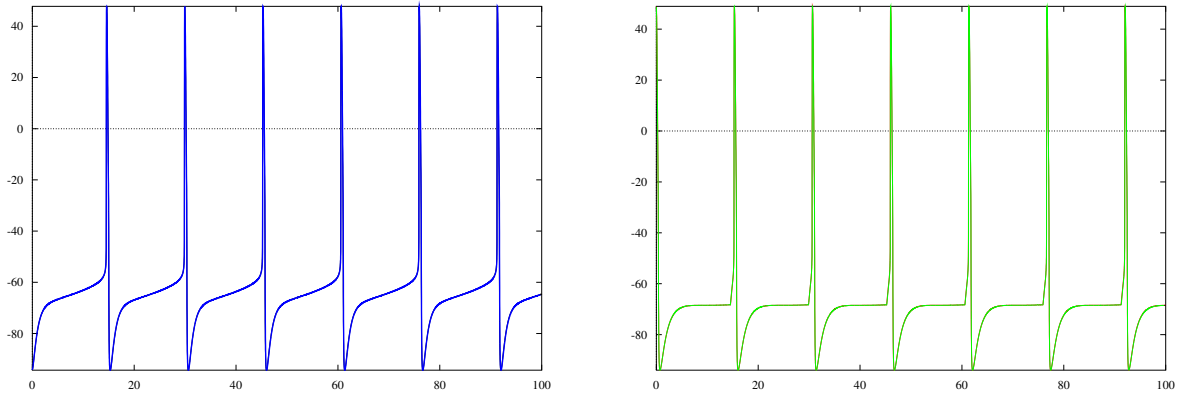


Figure 4.15. $\tau_e=1.5$, $\delta=0.5$, stable synchrony.

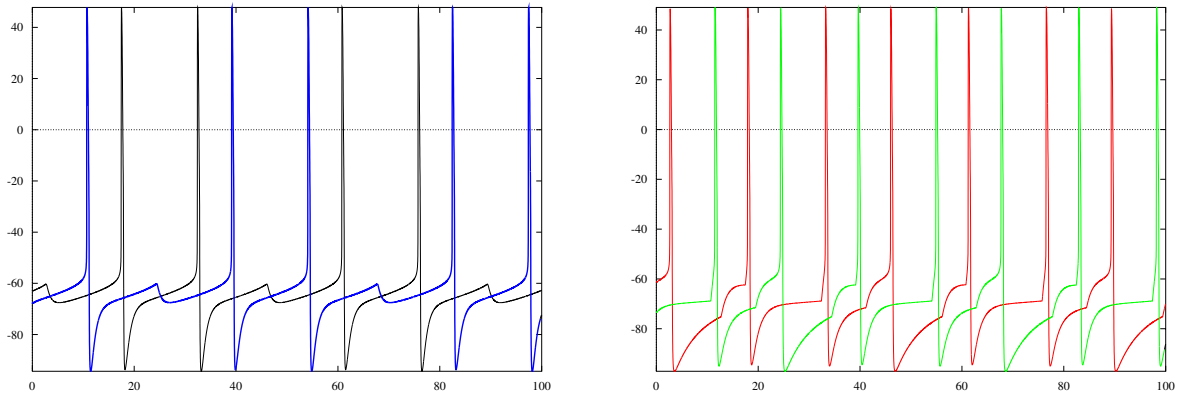


Figure 4.16. $\tau_e=1.5$, $\delta=2$, the “alternating” pattern, but with only singlets.

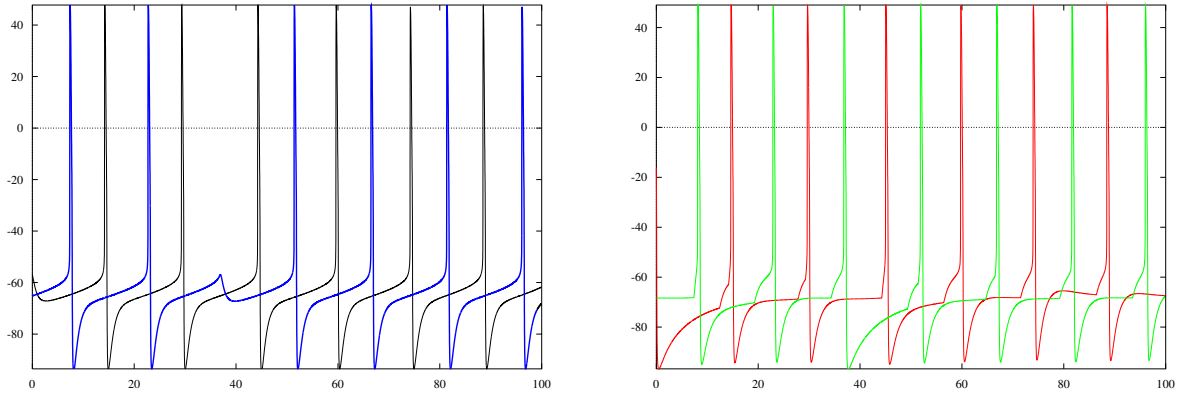


Figure 4.17. $\tau_e=1.5$, $\delta=5$, a fragment of an intricate pattern.

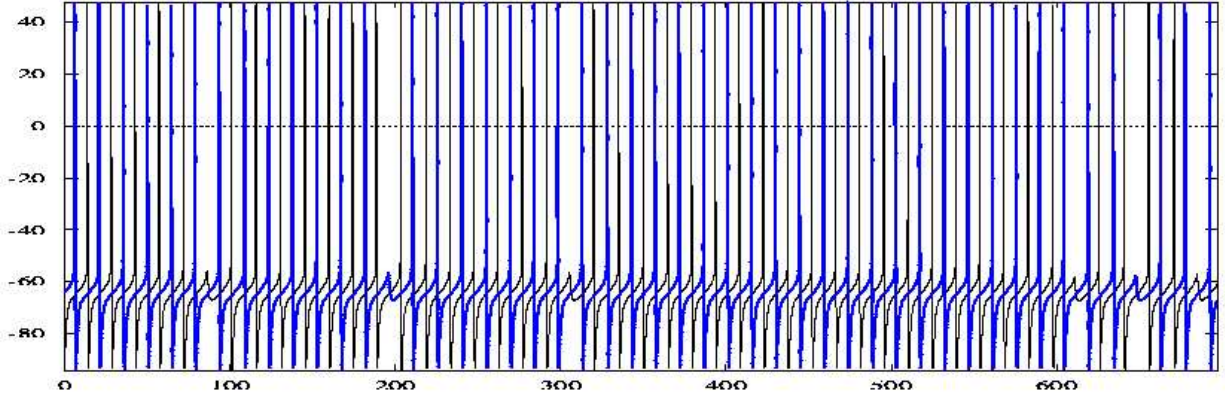


Figure 4.18. chaos?.

4.4.4 The Experimental Results of Fuchs *et al*

Given the phase-plot of Figure 4.4, we can now pick out the regions that corresponds to the results in [1]. In their study, single shocks elicit double action potentials in the mutant interneurons (i.e. with slowed EPSP's), but only single spikes in the wild-type mouse. Synchrony across the slice in wild mice is mediated by doublet firing in a large fraction of the population. Such a condition corresponds to parameters at, say, $\tau_e=2$ and $\delta = 7$ as noted above. To understand why synchrony is degraded for larger values of τ_e we consider a section of plot at, say, an average delay of $\delta=7$ ms. For $\tau_e=1.5$, the doublets are disrupted on either or both columns. At larger τ_e , e.g. $\tau_e=3$, the doublets are disrupted too, but through an extra spike that is picked up by one of the i-cells in each

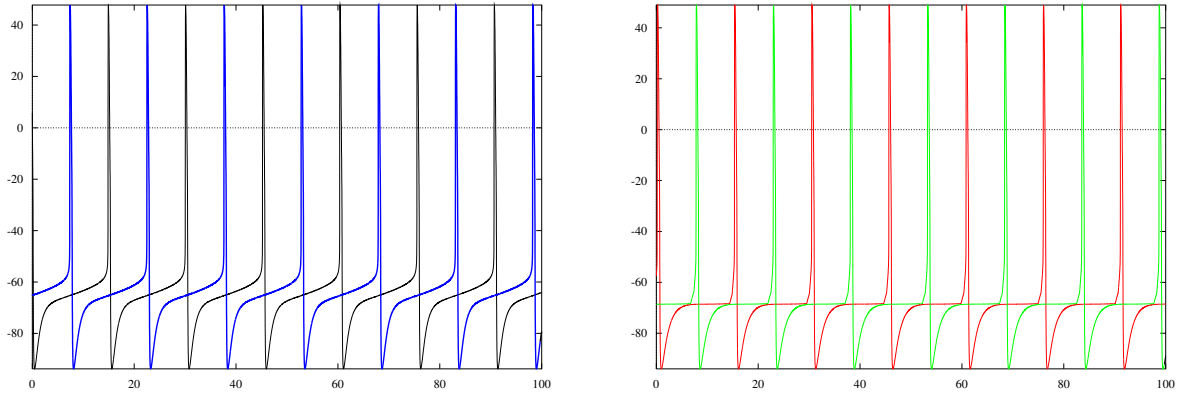


Figure 4.19. $\tau_e=1.5$, $\delta=7$, anti-synchrony.

cycle (i.e. the doublet-triplet mismatch). This is precisely the mechanism for the loss of synchrony with larger τ_e that was proposed in [1].

Carrying this argument further, our analysis also predicts that for even higher values of τ_e , it may be possible to improve synchrony again, this time with a feedback involving triplets. It may, of course, turn out to be difficult to test for this in experiment because the parameter ranges may be physiologically unrealistic. A wide variety of other interneurons are known to fire doublets relatively easily. The mechanism of synchrony through triplets is general enough that it may be tested for in other similar situations.

4.5 Discussion

In detailed computer simulations of the network, such as that in [1], [44], it is possible to capture many more features of the network than we do here. Such simulations also reproduce the morphology of neurons to some extent by constructing them out of “compartments” connected together. Although the complexity of individual neurons and synaptic connectivity is mimicked more closely, nevertheless it cannot be reproduced completely. Such a simulation can include several other features of the network including dendritic integration of EPSPs and gap junction coupling, and the effects of varying network size and connectivity. In such a large-scale simulation, it is difficult to separate cause and effect. In the reduced model we consider here, the role of the synaptic

kinetics in the dynamics of the rhythm becomes much clearer, and available to analysis.

We use a *map* in the Ermentrout-Kopell [7] framework to further clarify the role of the nonlinear response of an interneuron in providing the feedback loop mediating synchrony between signals that would otherwise naturally be out of phase with each other. [7] showed that interneuron doublets that arise from delayed extrinsic excitatory impulse can facilitate synchrony for certain amounts of network delays. This (i.e. doublet synchrony) is indeed the case that seems to be most relevant to experiments. Here we consider the effects of increasing and decreasing the EPSP time constant on network behavior. With a more persistent excitation i-cells can fire triplets. Experiments of [1] on mutant mice with larger decay EPSC kinetics show impaired synchrony. They observe triplet firings in population recordings; single cell recordings, however, show the absence of (intrinsic) triplets. We show a regime in τ_e and δ where synchrony is lost that is consistent with their results. We also note that synchrony arises primarily out of the interaction between the responses of the two i-cells (the e-cells are simply slaved to the inhibition). Thus we show it is also possible to stabilize synchrony with (intrinsic) triplets forming on both columns. It is even possible to synchronize with singlets; however, such a synchrony is not robust. In all of this, the map of the reduced problem, T_I , is central to the understanding.

4.6 Appendix

The equations for each cell are obtained from a model of Traub and Miles for spiking [41]. The equations are

$$\frac{CdV}{dt} = -g_L(V - V_L) - g_K n^4(V - V_K) - g_{Na} m^3 h(V - V_{Na}) + I_0 + I_{syn}$$

with ion channels for leak, sodium, and delayed rectifier potassium.

Here $m = m_\infty(V) = a_m(V)/[a_m(V) + b_m(V)]$ where $a_m(V) = 0.32(54 + V)/(1 - \exp[-(V + 54)/4])$ and $b_m(V) = 0.28(V + 27)/(\exp[(V + 27)/5] - 1)$.

The K-gate $n(t)$ satisfies $dn/dt = a_n(V)(1 - n) - b_n(V)n$, with $a_n(V) = 0.032(V + 52)/[1 - \exp(-(V + 52)/5)]$, $b_n(V) = 0.5 \exp[-(57 + V)/40]$.

A reduction to a two-dimensional equation is obtained (28) by setting $h = \max(1 - 1.25n, 0)$.

Parameter values are $C = 1$, $g_L = 0.1$, $V_L = -0.67$, $g_{Na} = 100$, $V_{Na} = 50$, $g_K = 80$, $V_K = -100$, $I_0 = 0.5$ for the I cells and $I_0 = 13$ for the E cells.

C is measured in $\mu F/cm^2$, conductances in mS/cm^2 , currents in $\mu A/cm^2$, voltages in mV , and time in ms .

Each synaptic current has the form $g_{syn}s(t-\delta)(V-V_{syn})$. Here $g_{syn} = g_{ii}, g_{ie}, g_{ei}, c_{ie}$ or c_{ei} . The subscripts denote the source and target of the synapse, the g 's denote conductance within a circuit, and the c 's denote conductance between the circuits, $g_{ii} = 0.15$, $g_{ei} = 0.34$, $g_{ie} = 1.8$, $c_{ei} = 0.12$ and $c_{ie} = 0$. $\delta = 0$ for synapses within a local circuit. s satisfies $ds/dt = A S(\hat{V})(1-s) - B s$, where $S(\hat{V}) = 1 + \tanh(\hat{V}/4)$ and \hat{V} is the presynaptic voltage. For excitatory synapses, $A = 20 \text{ ms}^{-1}$, $V_{syn} = 0$; for inhibitory synapses, $A = 1 \text{ ms}^{-1}$, $B = 0.05 \text{ ms}^{-1}$, $V_{syn} = -80 \text{ mV}$. Simulations were done using XPPAUT (Ermentrout [34]). The usual method of integration is a Gear-type integrator adapted for use with delay equations.

Chapter 5

Discussion

Recurrent activity is prominent in several aspects of brain function. Neurons, in particular, can exhibit oscillatory modes under appropriate conditions (i.e. for particular values of “driving” currents). We have studied here aspects of the patterns of temporal activity that can emerge in networks of neurons (oscillators) coupled together, using *maps* to facilitate a mathematical analysis. The use of maps is inspired by the idea that “firing” times of the oscillators can be “mapped out” from cycle to cycle as the activity recurs. The steady (asymptotic) state is of primary interest, as is the question of its stability to (small) disturbances.

In the first chapter, we study oscillators (largely inspired by neuronal behavior) pulse-coupled with phase response curves. PRCs serve to establish the neuron’s response to perturbations (typically synaptic input – excitatory or inhibitory) received at different phases in its cycle. As is to be expected, excitatory inputs typically advance the phase, while inhibitory input delays it; the PRC may also have both positive and negative halves (as a function of phase). The PRC itself can be measured directly in experiment, precluding the need to *model* the dynamics of the neuron. A PRC can also be computed numerically for a given *model* neuron (with different PRCs resulting for different types of “stimuli”), and for some simple cases, even analytically. We first study two (identical) neurons coupled through their PRCs. We derive a map that describes the firing time of one of the oscillators (using the other’s firing time for reference). Analysis of the stability of fixed points establishes conditions on synchrony (with both oscillators firing simultaneously on all cycles) and other phase-locked states. We show how these conditions can be related to the shape of the *PRC*. Thus, properties of *individual neurons* – the effect of stimulus on the period – the *PRC* – determine whether the synchronous solution exists in the *network*, and is stable to small perturbations. (That is, if one presumes that the PRC can be obtained in some (*a priori*) way, then its nature can be used to predict experimentally verifiable results on the temporal activity in the network.) We then extend the analysis to other geometries of connectivity. We obtain necessary and sufficient conditions for synchrony to be a stable solution in globally coupled networks.

Interestingly, in networks with an asymmetry in the (slope of the) PRC about 0 (the phase at which an oscillator is taken to fire), the size of the network becomes relevant. For no change in the PRC or the oscillators, networks larger than a critical size fail to synchronize stably, while any smaller network does (stably) synchronize. We demonstrate waves on a ring (with conditions on their stability), and in two dimensional arrays (stability is suggested from numerical simulation). We also study chains of oscillators. It is difficult, in general, to derive a map or study the stability of synchrony for such geometries as the chain and the ring: this arises from the fact that the firing sequence need not be maintained from one cycle to the next. (Then the problem quickly becomes combinatorial, and many cases would need to be considered separately even for small network sizes.) We do, however, speculate that for “sufficiently connected” topologies (with an irreducible connectivity matrix), the PRC can indicate stability of the synchronous solution. A theory for general all-to-all coupled networks remains open.

The techniques used here can probably be extended also to networks of oscillators with slightly different intrinsic frequencies. Another feature of the theory is that it largely ignores the strength of the perturbation due to multiple simultaneous inputs. That is, a neuron is assumed to respond to stimuli with only a change in phase, and not in amplitude. (The attraction to the limit cycle is assumed to be rapid (instantaneous); multiple inputs are “composed” together.) While heterogeneity in oscillator frequency can be expected to yield to the formalism to a certain extent, heterogeneity in coupling is significantly more difficult.

Another instance of rhythmicity in the brain is the oscillatory output evident in recordings of electrical (EEG) and magnetic (MEG) fields around the brain. We examine certain features of activity in the gamma band (in mice), and beta in humans.

Experiments of Jensen *et al* [6] observed a marked increase in the power in the human beta band with the administration of benzodiazepines: the source of this activity was located to the sensorimotor cortex. It seems surprising that an “inhibitory” drug (diapam) should result in the *increase* in power that is thought to be indicative of activity in excitatory cells. It was also noted that the frequency of the post-drug rhythm is slightly lower. We model this phenomenon in a small network of 64 excitatory cells, and 16 inhibitory cells to mimic the cortical population. Particularly significant for the model is an AHP current in the e-cells. In the model, the (oscillatory) inhibitory cells synchronize as a population, and gate the activity of the e-cells. The effect of an increase in

the levels of the GABAergic drug induces an increase in the inhibitory conductance; the i-rhythm slows down, allowing a larger number of the e-cells to emerge from suppression - thus registering an increase in the beta power recorded. We predict that the primary effect of the drug is an increase in i-i conductance; its effect on the i-e conductance is much less significant. We then model the role of the synaptic and AHP variables using simple exponentials. Since the time constant of AHP is comparable to the period of the oscillation, this current shows a significant adaptation over cycles. We can derive a map for its value at steady state that satisfies appropriate consistency conditions. This, along with the value of drive to an e-cell, determines the phase in the cycle when (if) the cell is able to fire. (Heterogeneity in the drive to the e-cells, and the consequential dispersion in phase of firing is responsible for the width of the spectral peak in the simulations.) These results complement those of the full simulation. We are thus able to indicate the possible physiological action of benzodiazepines in the sensorimotor cortex.

The key feature of the model, of course, is that the i-rhythm itself is not the one detected in the MEG, it is the e-rhythm entrained to it that is recorded. (Which is consistent with the literature.) Thus, an increase in “inhibition” decreases the gating capacity of the i-cells, with an increase in the e-activity.

In their experiments with gamma in mice, Fuchs *et al* [1] sought to determine the role of the excitatory time constants in determining the coherence of the rhythm. They generate transgenic mice with slowed EPSPs and found that the oscillations were degraded. Ermentrout and Kopell [7] had studied a version of this problem in a modeling study where they consider a simplified network consisting of a pair of e- and i-cells coupled with significant conduction delays. The rhythm itself is thought to arise from the e-cells oscillating with the i-cells in concert. Synchrony across spatially distant sites was shown in [7] to be mediated via a doublet firing mechanism (proposed earlier by Traub *et al* [37]). In the model, excitatory input received by an i-cell generates a response that varies with the phase in the oscillation at which it was received. A second input – or, equivalently – simultaneous e-cell firings at spatially distal columns that is temporally dispersed as inputs to an i-cell by the conduction delay – could evoke a second spike in the i-cell, a doublet. The response of the i-cell can be mapped out as a function of the (temporal) separation of two e-inputs to an i-cell. This curve can then be used to write down a map for the difference in firing times of the two e-cells on successive cycles. Synchrony corresponds to a fixed point of this map. Stability of

the synchronous solution is then seen to be related to the slope of the T_I . And as shown in [7], the doublet firing generates a feedback mechanism that is necessary for synchrony to be robust to perturbation.

Here we have used the same model to explain the results of [1] as to why a longer EPSP time constant can disturb this phenomena. We find that a doublet-triplet mismatch occurs at the two sites if the EPSP is prolonged enough that it can cause a *triplet* firing to occur in an i-cell (as was verified in their experiment). We generate a plot of regions of synchrony for varying values of τ_e , and conduction delays δ . We use T_I maps (in the spirit of [7]) computed for different τ_e to predict the boundaries of regions of stability. We find that the results of the full simulations bear out the predictions based on the map.

A noteworthy point to mention with respect to the two modeling studies above is that in the case of the beta model, it is that i-cells that are primarily responsible for the network rhythm (in the sense that the e-cells are slaved to them). Whereas, in the case of the gamma model the excitatory cells are at least as important to shaping the rhythm as the i-cells: in fact, the i-cells need not even be modeled as oscillatory, as long as they are excitable. The beta model follows essentially an ING mechanism, while the gamma is modeled as a PING rhythm.

We have studied several aspects of rhythmicity in the brain in this work. We have been able to formulate several of the questions in a mathematical framework of iterated maps (as discrete dynamical systems). Questions of synchrony as a solution translate to questions concerning (the appropriate) fixed points in these maps. We can then also often address the issue of the stability of these fixed points: that is, of the robustness of the activity pattern.

Appendix

Glossary of Select Terms

AHP current (One of several) currents that prolongs the *afterhyperpolarization* phase following an action potential. The AHP current considered here is a slow voltage-gated K^+ current. Following a depolarization an outward potassium current rapidly leaves the membrane; at first this conductance is large and results in the membrane repolarizing to values more negative than the resting potential. As the inside becomes more negative the potassium diffusion slows down, allowing the membrane to return towards rest.

AMPA α -amino-3-hydroxy-5-methyl-4-isoxazolepropionic acid. A prominent excitatory neurotransmitter in the brain.

EPSP Excitatory postsynaptic potential. An EPSP is so called because a (presynaptic) excitatory neuron influences a (postsynaptic) neuron through a current term with a reversal potential that is typically positive with respect to the resting potential. In a network, excitatory neurons tend to drive postsynaptic neurons towards firing sooner than in the uncoupled case.

GABA γ -aminobutyric acid. A prominent inhibitory neurotransmitter in the brain.

ING Interneuron network gamma oscillations. Gamma oscillation that is supposed to arise from coherence in a network composed primarily of oscillating interneurons; pharmacologically isolated networks of interneurons have been shown to generate gamma oscillations. Pyramidal cells play a passive role in such a network.

Interneurons A variety of neurons that are predominantly responsible for inhibitory connections in the hippocampus and the cortex. Interneurons are GABA releasing local circuit (inhibitory) neurons.

IPSP Inhibitory postsynaptic potential. The reversal potential of an inhibitory synapse is typically more negative than the resting potential. Thus, inhibitory synapses tend to delay (suppress) firing in the postsynaptic cell.

MEG Magnetoencephalography. A non-invasive method of recording brain activity. MEGs record magnetic fields evoked at the surface of the brain due to ionic current flow from nerve activity. MEGs are recorded using the SQUID (Superconducting Quantum Interference Device), an ultrasensitive detector of magnetic flux. (Compare also EEG, electroencephalography, which is a measure of electric fields recorded as potential differences between electrodes placed on the scalp.)

Pyramidal cells A variety of neurons especially relevant to the hippocampus and the cortex that typically makes excitatory synapses.

PING Pyramidal-interneuron network gamma oscillations. Gamma oscillation that is supposed to arise from coherence in a network of interneurons and pyramidal cells. Pyramidal cells are integral to oscillations in the network. Note that one of the inhibitory population could be modeled as *excitable* (with the pyramidal cells oscillatory), and not necessarily oscillatory.

Synapse The cells of neurons are *connected* in networks through synapses. A synapse is a physical gap between two neurons; upon arrival of an action potential at the *presynaptic* terminal of the synapse, *neurotransmitters* are released into the synaptic cleft. These typically influence *receptors* on the *postsynaptic* neuron to produce changes in its membrane potential.

Tetanic Stimulus A stimulus protocol that involves delivering a train of sharp, rapid, short voltage pulses to the neuron to induce an oscillation. (See text for more details.)

Bibliography

1. E. C. Fuchs, H. Doheny, H. Faulkner, A. Caputi, R. D. Traub, A. Bibbig, N. Kopell, M. A. Whittington, and H. Monyer. Genetically altered AMPA-type glutamate receptor kinetics in interneurons disrupt long-range synchrony of gamma oscillation. *Proc Natl Acad Sci U S A*, 98(6):3571–3576, Mar 2001.
2. Arthur T. Winfree. *The geometry of biological time*, volume 8 of *Biomathematics*. Springer-Verlag, Berlin, 1980.
3. J. Buck. Synchronous rhythmic flashing of fireflies II. *Q Rev Biol*, 63(3):265–289, Sep 1988.
4. R. Traub and R. Miles. *Neuronal Networks of the Hippocampus*. Cambridge University Press, 1991.
5. M. A. Whittington, I. M. Stanford, S. B. Colling, J. G. Jefferys, and R. D. Traub. Spatiotemporal patterns of gamma frequency oscillations tetanically induced in the rat hippocampal slice. *J Physiol*, 502 (Pt 3):591–607, Aug 1997.
6. O. Jensen, M. Pohja, P. Goel, B. Ermentrout, N. Kopell, and R. Hari. On the physiological basis of the 15-30 hz motor-cortex rhythm. In H. Nowak, J. Haueisen, F. Giessler, and R. Huonkner, editors, *Proceedings of the 13th International Conference on Biomagnetism*, pages 313–315. VDE Verlag GMBH, Berlin, 2002.
7. G. B. Ermentrout and N. Kopell. Fine structure of neural spiking and synchronization in the presence of conduction delays. *Proc Natl Acad Sci U S A*, 95(3):1259–1264, Feb 1998.
8. C. M. Gray. Synchronous oscillations in neuronal systems: mechanisms and functions. *J Comput Neurosci*, 1(1-2):11–38, Jun 1994.
9. Y. Kuramoto. *Chemical oscillations, waves, and turbulence*, volume 19 of *Springer Series in Synergetics*. Springer-Verlag, Berlin, 1984.
10. Renato E. Mirollo and Steven H. Strogatz. Synchronization of pulse-coupled biological oscillators. *SIAM J. Appl. Math.*, 50(6):1645–1662, 1990.
11. P.C. Bressloff and S. Coombes. Symmetry and phase-locking in a ring of pulse-coupled oscillators with distributed delays. *Physica D*, 126:99–122, 1999.
12. C. Van Vreeswijk., L. F. Abbott, and G. B. Ermentrout. When inhibition not excitation synchronizes neural firing. *J Comput Neurosci*, 1(4):313–321, Dec 1994.
13. George Bard Ermentrout and Nancy Kopell. Frequency plateaus in a chain of weakly coupled oscillators. I. *SIAM J. Math. Anal.*, 15(2):215–237, 1984.

14. Joseph E. Paulllet and G. Bard Ermentrout. Stable rotating waves in two-dimensional discrete active media. *SIAM J. Appl. Math.*, 54(6):1720–1744, 1994.
15. D. Hansel, G. Mato, and C. Meunier. Synchrony in excitatory neural networks. *Neural Comput*, 7(2):307–337, Mar 1995.
16. R. Dror, C.C. Canavier, R.J. Butera, J.W. Clark, and J.H. Byrne. A mathematical criterion based on prcs for stability in a ring of coupled oscillators. *Biol. Cyber.*, 80:11–23, 1999.
17. C.C. Canavier, D.A. Baxter, J.W. Clark, and J.H. Byrne. Control of multistability in ring circuits of oscillators. *Biol. Cyber.*, 80:87–102, 1999.
18. N. Kopell. Towards a theory of modeling central pattern generators. *Neural Control of Rhythms, Wiley, New York*, 1988.
19. A. D. Reyes and E. E. Fetz. Two modes of interspike interval shortening by brief transient depolarizations in cat neocortical neurons. *J Neurophysiol*, 69(5):1661–1672, May 1993.
20. R. Stoop, L. A. Bunimovich, and W. H. Steeb. Generic origins of irregular spiking in neocortical networks. *Biol Cybern*, 83(6):481–489, Dec 2000.
21. Pranay Goel and Bard Ermentrout. Synchrony, stability, and firing patterns in pulse-coupled oscillators. *Phys. D*, 163(3-4):191–216, 2002.
22. B. Ermentrout. Type 1 membranes, phase resetting curves, and synchrony. *Neural Comput*, 8(5):979–1001, Jul 1996.
23. Frank C. Hoppensteadt and Eugene M. Izhikevich. *Weakly connected neural networks*, volume 126 of *Applied Mathematical Sciences*. Springer-Verlag, New York, 1997.
24. Leon Glass and Michael C. Mackey. *From clocks to chaos*. Princeton University Press, Princeton, NJ, 1988. The rhythms of life.
25. A. T. Winfree. Patterns of phase compromise in biological cycles. *J. Math. Biol.*, 1(1):73–95, 1974/75.
26. J. Guckenheimer. Isochrons and phaseless sets. *J. Math. Biol.*, 1(3):259–273, 1974/75.
27. G. Bard Ermentrout. $n : m$ phase-locking of weakly coupled oscillators. *J. Math. Biol.*, 12(3):327–342, 1981.
28. A. T. Winfree. Biological rhythms and the behavior of populations of coupled oscillators. *Journal of Theoretical Biology*, 16:15–42, 1967.
29. J. T. Ariaratnam and S. H. Strogatz. Phase diagram for the winfree model of coupled nonlinear oscillators. *Phys Rev Lett*, 86(19):4278–4281, May 2001.
30. G. B. Ermentrout and N. Kopell. Multiple pulse interactions and averaging in systems of coupled neural oscillators. *J. Math. Biol.*, 29(3):195–217, 1991.
31. G. Bard Ermentrout. Stable periodic solutions to discrete and continuum arrays of weakly coupled nonlinear oscillators. *SIAM J. Appl. Math.*, 52(6):1665–1687, 1992.
32. Leah Edelstein-Keshet. *Mathematical models in biology*. The Random House/Birkhäuser Mathematics Series. Random House Inc., New York, 1988.

33. N. Kopell and G.B. Ermentrout. Symmetry and phase-locking in chains of weakly coupled oscillators. *Commun. Pure Appl. Math.*, 39:623–660, 1986.
34. Bard Ermentrout. *Simulating, analyzing, and animating dynamical systems*, volume 14 of *Software, Environments, and Tools*. Society for Industrial and Applied Mathematics (SIAM), Philadelphia, PA, 2002. A guide to XPPAUT for researchers and students.
35. J.M. Greenberg. Spiral waves for lambda-omega systems. *SIAM J. Appl. Math.*, 39:301–309, 1982.
36. P.S. Hagan. Spiral waves in reaction-diffusion systems. *SIAM J. Appl. Math.*, 42:762–786, 1982.
37. R. D. Traub, M. A. Whittington, I. M. Stanford, and J. G. R. Jeffreys. A mechanism for generation of long-range synchronous fast oscillations in the cortex. *Nature*, 383:621–624, 1996.
38. J. A. White, C. C. Chow, J. Ritt, C. Soto-Trevino, and N. Kopell. Synchronization and oscillatory dynamics in heterogeneous, mutually inhibited neurons. *J Comput Neurosci*, 5(1):5–16, Mar 1998.
39. X. J. Wang and G. Buzsaki. Gamma oscillation by synaptic inhibition in a hippocampal interneuronal network model. *J Neurosci*, 16(20):6402–6413, Oct 1996.
40. C. C. Chow and N. Kopell. Dynamics of spiking neurons with electrical coupling. *Neural Comput*, 12(7):1643–1678, Jul 2000.
41. R. D. Traub, R. K. Wong, R. Miles, and H. Michelson. A model of a CA3 hippocampal pyramidal neuron incorporating voltage-clamp data on intrinsic conductances. *J Neurophysiol*, 66(2):635–650, Aug 1991.
42. M. S. Hamalainen. Magnetoencephalography: a tool for functional brain imaging. *Brain Topogr*, 5(2):95–102, Winter 1992.
43. William H. Press, Saul A. Teukolsky, William T. Vetterling, and Brian P. Flannery. *Numerical recipes in C*. Cambridge University Press, Cambridge, second edition, 1992. The art of scientific computing.
44. R. D. Traub, M. A. Whittington, E. H. Buhl, J. G. Jefferys, and H. J. Faulkner. On the mechanism of the gamma \rightarrow beta frequency shift in neuronal oscillations induced in rat hippocampal slices by tetanic stimulation. *J Neurosci*, 19(3):1088–1105, Feb 1999.
45. G.B. Ermentrout. Stable periodic solutions to discrete and continuum arrays of weakly coupled nonlinear oscillators. *SIAM J. Appl. Math.*, 52:1665–1687, 1992.
46. N. Kopell and G. B. Ermentrout. Coupled oscillators and the design of central pattern generators. *Math. Biosci.*, 90(1-2):87–109, 1988. Nonlinearity in biology and medicine (Los Alamos, NM, 1987).
47. P. C. Bressloff and S. Coombes. Dynamics of strongly-coupled spiking neurons. *Neural Comput*, 12(1):91–129, Jan 2000.
48. N. Kopell, G. B. Ermentrout, M. A. Whittington, and R. D. Traub. Gamma rhythms and beta rhythms have different synchronization properties. *Proc Natl Acad Sci U S A*, 97(4):1867–1872, Feb 2000.

49. R. D. Traub, A. Bibbig, A. Fisahn, F. E. LeBeau, M. A. Whittington, and E. H. Buhl. A model of gamma-frequency network oscillations induced in the rat CA3 region by carbachol in vitro. *Eur J Neurosci*, 12(11):4093–4106, Nov 2000.
50. M. A. Whittington, R. D. Traub, N. Kopell, B. Ermentrout, and E. H. Buhl. Inhibition-based rhythms: experimental and mathematical observations on network dynamics. *Int J Psychophysiol*, 38(3):315–336, Dec 2000.
51. M. A. Whittington, H. C. Doheny, R. D. Traub, F. E. LeBeau, and E. H. Buhl. Differential expression of synaptic and nonsynaptic mechanisms underlying stimulus-induced gamma oscillations in vitro. *J Neurosci*, 21(5):1727–1738, Mar 2001.
52. R. D. Traub, N. Kopell, A. Bibbig, E. H. Buhl, F. E. LeBeau, and M. A. Whittington. Gap junctions between interneuron dendrites can enhance synchrony of gamma oscillations in distributed networks. *J Neurosci*, 21(23):9478–9486, Dec 2001.
53. Stephen. K. Towers, Fiona. E. N. LeBeau, Tengis. Gloveli, Roger. D. Traub, Miles. A. Whittington, and Eberhard. H. Buhl. Fast network oscillations in the rat dentate gyrus in vitro. *J Neurophysiol*, 87(2):1165–1168, Feb 2002.
54. Andrea Bibbig, Roger. D. Traub, and Miles. A. Whittington. Long-range synchronization of gamma and beta oscillations and the plasticity of excitatory and inhibitory synapses: a network model. *J Neurophysiol*, 88(4):1634–1654, Oct 2002.
55. Mette. S. Olufsen, Miles. A. Whittington, Marcelo. Camperi, and Nancy. Kopell. New roles for the gamma rhythm: population tuning and preprocessing for the Beta rhythm. *J Comput Neurosci*, 14(1):33–54, Jan 2003.
56. Christoph. Borgers and Nancy. Kopell. Synchronization in networks of excitatory and inhibitory neurons with sparse, random connectivity. *Neural Comput*, 15(3):509–538, Mar 2003.
57. J. Buck and E. Buck. Synchronous fireflies. *Sci Am*, 234(5):74–79, May 1976.
58. S. P. Ahlfors, R. J. Ilmoniemi, and M. S. Hamalainen. Estimates of visually evoked cortical currents. *Electroencephalogr Clin Neurophysiol*, 82(3):225–236, Mar 1992.
59. M. S. Hamalainen. Basic principles of magnetoencephalography. *Acta Radiol Suppl*, 377:58–62, 1991.
60. M. Hamalainen. Anatomical correlates for magnetoencephalography: integration with magnetic resonance images. *Clin Phys Physiol Meas*, 12 Suppl A:29–32, 1991.
61. J. Buck and E. Buck. Mechanism of rhythmic synchronous flashing of fireflies. Fireflies of Southeast Asia may use anticipatory time-measuring in synchronizing their flashing. *Science*, 159(821):1319–1327, Mar 1968.
62. A. T. Winfree. Biological rhythms and the behavior of populations of coupled oscillators. *J Theor Biol*, 16(1):15–42, Jul 1967.
63. M. S. Hamalainen and R. J. Ilmoniemi. Interpreting magnetic fields of the brain: minimum norm estimates. *Med Biol Eng Comput*, 32(1):35–42, Jan 1994.

64. R. Hari, J. Karhu, M. Hamalainen, J. Knuutila, O. Salonen, M. Sams, and V. Vilkmán. Functional organization of the human first and second somatosensory cortices: a neuromagnetic study. *Eur J Neurosci*, 5(6):724–734, Jun 1993.
65. R. Hari, A. Ahonen, N. Forss, M. L. Granstrom, M. Hamalainen, M. Kajola, J. Knuutila, O. V. Lounasmaa, J. P. Makela, and R. Paetau. Parietal epileptic mirror focus detected with a whole-head neuromagnetometer. *Neuroreport*, 5(1):45–48, Oct 1993.
66. A. D. Reyes and E. E. Fetz. Effects of transient depolarizing potentials on the firing rate of cat neocortical neurons. *J Neurophysiol*, 69(5):1673–1683, May 1993.
67. J. G. Jefferys, R. D. Traub, and M. A. Whittington. Neuronal networks for induced '40 Hz' rhythms. *Trends Neurosci*, 19(5):202–208, May 1996.
68. R. D. Traub, M. A. Whittington, S. B. Colling, G. Buzsáki, and J. G. Jefferys. Analysis of gamma rhythms in the rat hippocampus in vitro and in vivo. *J Physiol*, 493 (Pt 2):471–484, Jun 1996.
69. C. M. Gray. Synchronous oscillations in neuronal systems: mechanisms and functions. *J Comput Neurosci*, 1(1-2):11–38, Jun 1994.
70. F. K. Skinner, N. Kopell, and E. Marder. Mechanisms for oscillation and frequency control in reciprocally inhibitory model neural networks. *J Comput Neurosci*, 1(1-2):69–87, Jun 1994.
71. R. D. Traub, J. G. Jefferys, and M. A. Whittington. Simulation of gamma rhythms in networks of interneurons and pyramidal cells. *J Comput Neurosci*, 4(2):141–150, Apr 1997.
72. M. A. Whittington, R. D. Traub, H. J. Faulkner, J. G. Jefferys, and K. Chettiar. Morphine disrupts long-range synchrony of gamma oscillations in hippocampal slices. *Proc Natl Acad Sci U S A*, 95(10):5807–5811, May 1998.
73. R. D. Traub, N. Spruston, I. Soltesz, A. Konnerth, M. A. Whittington, and G. R. Jefferys. Gamma-frequency oscillations: a neuronal population phenomenon, regulated by synaptic and intrinsic cellular processes, and inducing synaptic plasticity. *Prog Neurobiol*, 55(6):563–575, Aug 1998.
74. H. J. Faulkner, R. D. Traub, and M. A. Whittington. Disruption of synchronous gamma oscillations in the rat hippocampal slice: a common mechanism of anaesthetic drug action. *Br J Pharmacol*, 125(3):483–492, Oct 1998.
75. C. C. Chow, J. A. White, J. Ritt, and N. Kopell. Frequency control in synchronized networks of inhibitory neurons. *J Comput Neurosci*, 5(4):407–420, Dec 1998.
76. A. V. Olypher. Gamma oscillations by synaptic inhibition in a homogeneous medium model of hippocampal interneurons. *Biosystems*, 48(1-3):165–169, Sep 1998.